CHARACTERIZATION AND LIFETIME PERFORMANCE MODELING OF ACRYLIC FOAM TAPE FOR STRUCTURAL GLAZING APPLICATIONS

Benjamin W. Townsend

Thesis submitted to the faculty of the

Virginia Polytechnic Institute and State University

in partial fulfillment of the requirements for the degree of

MASTER OF SCIENCE

IN

CIVIL ENGINEERING

Dr. David A. Dillard, Co-Chairman

Dr. Raymond H. Plaut, Co-Chairman

Dr. Donatus C. Ohanehi

September 12, 2008

Blacksburg, Virginia

Keywords: VHB Acrylic Tape, Creep Rupture, Time Temperature Superposition Principle, Wind Loading, Linear Damage Accumulation Model

Characterization and Lifetime Performance Modeling of Acrylic Foam Tape for Structural Glazing Applications

Benjamin W. Townsend

(ABSTRACT)

This thesis presents the results of testing and modeling conducted to characterize the performance of 3M™ VHB™ structural glazing tape in both shear and tension. Creep rupture testing results provided the failure time at a given static load and temperature, and ramp-to-fail testing results provided the ultimate load resistance at a given rate of strain and temperature. Parallel testing was conducted on three structural silicone sealants to compare performance. Using the time temperature superposition principle, master curves of VHB tape storage and loss moduli in shear and tension were developed with data from a dynamic mechanical analyzer (DMA). The thermal shift factors obtained from these constitutive tests were successfully applied to the creep rupture and ramp-to-fail data collected at 23°C, 40°C, and 60°C (73°F, 104°F, and 140°F), resulting in master curves of ramp-to-fail strength and creep rupture durability in shear and tension. A simple linear damage accumulation model was then proposed to examine the accumulation of wind damage if VHB tape is used to attach curtain wall glazing panels to building facades. The purpose of the model was to investigate the magnitude of damage resulting from the accumulation of sustained wind speeds that are less than the peak design wind speed. The model used the equation derived from tensile creep rupture testing, extrapolated into the range of stresses that would typically be generated by wind loading. This equation was applied to each individual entry in the data files of several real wind speed histories, and the fractions of life used at each entry were combined into a total percentage of life used. Although the model did not provide evidence that the established design procedure is unsafe, it suggested that the accumulation of damage from wind speeds below the peak wind speed could cause a VHB tape mode of failure that merits examination along with the more traditional peak wind speed design procedure currently recommended by the vendor.

ACKNOWLEDGEMENTS

I would like to thank my committee: Dr. David Dillard, whose guidance and helpful insights have allowed me to engage any unfamiliar concept that came my way during this research effort; Dr. Donatus Ohanehi, who assisted me along every step of the project with thoughtfulness and attention to detail; and Dr. Raymond Plaut, for recommending me for the project and his ongoing support.

I would also like to thank 3M for their financial support, with special thanks to Steve Austin and Fay Salmon for providing specimens as well as their experience and advice throughout the project.

Finally, I would like to thank those who are closest to my heart. Allison Skaer has been a constant source of loving support, and her encouragement has given me the motivation I needed to finish this thesis. My parents William and Barbara Townsend and my sister Alyssa Townsend-Hudders have provided their love and confidence throughout my life, and to them I will always owe a part of my success.

TABLE OF CONTENTS

CHAPTER 1 Introduction 1

CHAPTER 2 Characterization of Acrylic Foam Tape for Building Glazing Applications 3

Abstract 3

Introduction 3

Experimental

DMA 6

Creep Rupture 9

Ramp-to-Fail 17

Results and Discussion

DMA 19

Creep Rupture 30

Ramp-to-Fail 46

Conclusions 57

References 59

CHAPTER 3 Postulating A Simple Damage Model for the Long-Term Durability of Structural Glazing Adhesive Subject to Sustained Wind Loading 60

Abstract 60

Introduction 60

Sources of Wind Data 63

Wind Speed and Adhesive Stress 64

Prediction of Failure Time Based on Adhesive Stress 68

Results and Discussion 73

Conclusions 84

References 87

CHAPTER 4 Conclusions 89

Future Work 92

Appendix A Damage and Healing 93
Appendix B FE Inputs 98
Appendix C Thermal Expansion 101
Appendix D Operating Manual for 72 Station Pneumatic Creep Rupture Test Frame 107
Appendix E Supplementary DMA Data 111
Appendix F Teflon Jig 118
Appendix G Bending Jig 119
Appendix H Tabulated RTF Data 120
Appendix I Moisture Uptake Side Study 124

LIST OF FIGURES

Figure 2.1 Double shear sandwich specimen; arrows indicate the VHB tape specimens. 8
Figure 2.2 Compressive specimens showing test configurations with a) a single layer, and b) four layers of tape. 9
Figure 2.3 The long-axis tension a) specimen and b) grip. 9
Figure 2.4 72-station test frame with front face of temperature control chamber removed. 10
Figure 2.5 Close view of a) silicone sealant and b) VHB tape specimens mounted in the creep rupture test frame. 11
Figure 2.6 Butt tensile joint specimens. 13
Figure 2.7 Single-lap shear joint specimens. 13
Figure 2.8 Butt joint tensile specimens, modified for mounting in test frame. 16
Figure 2.9 Single-lap shear joint specimens, modified for mounting in test frame. 17
Figure 2.10 S-bends in silicone single-lap shear joint improve the alignment and avoid applying bending moments to the rods of the air cylinders. 17
Figure 2.11 Storage modulus was shifted manually to 30°C (86°F) reference temperature and then fit with the WLF equation using least-squares regression. 21
Figure 2.12 G23F storage modulus master curve at 30°C (86°F) reference temperature and using WLF shift factors with C1 = 9.98 and C2 = 132.6. 22
Figure 2.13 G23F loss modulus master curve at 30°C (86°F) reference temperature and using WLF shift factors with C1 = 9.98 and C2 = 132.6. 22
Figure 2.14 Application of temperature during DMA testing. 23
Figure 2.15 Shear geometry G23F storage modulus master curve at 30°C (86°F) reference temperature and using WLF shift factors with C1 = 9.98 and C2 = 132.6. 24
Figure 2.16 Shear geometry G23F loss modulus master curve at 30°C (86°F) reference temperature and using WLF shift factors with C1 = 9.98 and C2 = 132.6. 24
Figure 2.17 Loss modulus as a function of time from the first shear geometry replicate. 25
Figure 2.18 Tan delta (storage modulus over loss modulus) as a function of time from the first shear geometry replicate. 25

Figure 2.19 Compression geometry G23F storage modulus master curve at 30°C (86°F) reference temperature and using WLF shift factors with C1 = 9.98 and C2 = 132.6. 26
Figure 2.20 Long-axis tension geometry G23F storage modulus master curve at 30°C (86°F) reference temperature and using WLF shift factors with C1 = 9.98 and C2 = 132.6. 27
Figure 2.21 Method (1) for determination of Tg at 1 Hz: intersection of tangents to glassy plateau region of storage modulus and transition region of storage modulus. 29
Figure 2.22 Creep rupture data – anodized aluminum adherends bonded with G23F VHB tape and three structural silicone sealants. 31
Figure 2.23 Log-log plot of unshifted tensile VHB tape creep rupture data, along with data which has been shifted to 30°C (86°F) reference temperature; each data point is an average of nine replicates, and error bars represent ± one standard deviation. 32
Figure 2.24 Log-log plot of unshifted shear VHB tape creep rupture data, along with data which has been shifted to 30°C (86°F) reference temperature; each data point is an average of nine replicates, and error bars represent ± one standard deviation. 32
Figure 2.25 Representative failed tensile VHB tape specimens, tested at 23°C (73°F), showing some entrapped air voids. 35
Figure 2.26 VHB tape specimens in a) tension and b) shear at nearly 900% strain. 35
Figure 2.27 Representative failed shear VHB tape specimens, tested at 23°C (73°F), showing wedge-shaped residual adhesive. 36
Figure 2.28 Representative failed shear VHB tape specimens, tested at 23°C (73°F). 36
Figure 2.29 Failed tensile VHB tape specimens, tested at 60°C (140°F) and 0.07 MPa (10 psi). 37
Figure 2.30 Failed shear VHB tape specimens, tested at 60°C (140°F) and 0.15 MPa (22 psi). 38
Figure 2.31 Occurrence of adhesive failure surface in relation to creep stress and temperature. 39
Figure 2.32 Occurrence of adhesive failure surface in relation to log time to fail and temperature. 39
Figure 2.33 Occurrence of adhesive failure surface in relation to log time to fail shifted to 30°C (86°F) reference temperature. 40
Figure 2.34 Creep rupture coefficient of variation by specimen type. 40

Figure 2.35 Failed S1 tensile creep rupture specimens. 41
Figure 2.36 Failed S1 shear creep rupture specimens. 42
Figure 2.37 Failed S2 tensile creep rupture specimens. 43
Figure 2.38 Failed S2 shear creep rupture specimens. 43
Figure 2.39 Failed S3 tensile creep rupture specimens. 44
Figure 2.40 Failed S3 shear creep rupture specimens. 45
Figure 2.41 Peak tensile stress resistance of specimens subject to several ramp-to-fail strain rates....47
Figure 2.42 Peak shear stress resistance of specimens subject to several ramp-to-fail strain rates. 48
Figure 2.43 Hackle pattern on shear VHB tape specimen tested at 60°C (140°F) and 500 mm/min (19.7 in./min)....49
Figure 2.44 S1 tensile specimen with bubble voids highlighted. 50
Figure 2.45 S3 tensile specimen with thin, crack-like voids highlighted....50
Figure 2.46 Untested S3 specimens with thin, crack-like voids highlighted. 51
Figure 2.47 5 mm/min (0.197 in./min) tensile ramp-to-fail plots; one representative replicate shown for each condition set....52
Figure 2.48 50 mm/min (1.97 in./min) tensile ramp-to-fail plots; one representative replicate shown for each condition set....52
Figure 2.49 500 mm/min (19.7 in./min) tensile ramp-to-fail plots; one representative replicate shown for each condition set....53
Figure 2.50 5 mm/min (0.197 in./min) shear ramp-to-fail plots; one representative replicate shown for each condition set....53
Figure 2.51 50 mm/min (1.97 in./min) shear ramp-to-fail plots; one representative replicate shown for each condition set....54
Figure 2.52 500 mm/min (19.7 in./min) shear ramp-to-fail plots; one representative replicate shown for each condition set....54
Figure 2.53 Tensile VHB tape master curve of shifted ramp-to-fail data; 30°C (86°F) reference temperature. 55

Figure 2.54 Shear VHB tape master curve of shifted ramp-to-fail data; 30°C (86°F) reference temperature. 56
Figure 3.1 Wind speed and direction at Fowley Rocks, FL during Hurricane Wilma, showing average values sampled over ten-minute intervals. 64
Figure 3.2 Conceptual model relating wind speeds to design pressure. 66
Figure 3.3 Trapezoidal load distribution. 67
Figure 3.4 Log-log plot of unshifted tensile VHB tape creep rupture data, along with data which has been shifted to 30°C (86°F) reference temperature; each data point is an average of nine replicates, and error bars represent one standard deviation. 69
Figure 3.5 Frequency of readings and percentage of predicted damage from wind speeds at Chicago, IL. 74
Figure 3.6 Frequency of readings and percentage of predicted damage from wind speeds at Fowley Rocks, FL, without hurricane winds. 75
Figure 3.7 Frequency of readings and percentage of predicted damage from wind speeds at Fowley Rocks, FL, including hurricane winds. 76
Figure 3.8 Illustration of comparison between creep rupture line and wind-induced stress distribution. 78
Figure 3.9 Comparison between creep rupture line and wind-induced stress distribution where high wind-induced stresses dominate life used. 78
Figure 3.10 Comparison between creep rupture line and wind-induced stress distribution where all wind-induced stresses contribute equally. 79
Figure 3.11 Comparison between creep rupture line and wind-induced stress distribution where low wind-induced stresses dominate life used. 79
Figure 3.12 Comparison between creep rupture line and wind-induced stress distributions. 80

All images are property of the author.

LIST OF TABLES

Table 2.1 Applied DMA Strain Amplitudes 7
Table 2.2 WLF Constants for Various Reference Temperatures 21
Table 2.3 Tg Values Derived from DMA Testing on Shear Specimens 29
Table 2.4 Summary of the Common Defects and Associated Effect on Time to Failure 46
Table 3.1 Constant Wind Speeds and Resulting Failure Times (based on a best fit of mean failure times for a limited data set) 70
Table 3.2 Predicted Damage With No Safety Factor 73
Table 3.3 Top Wind Speeds and Accompanying Life Used at Chicago, IL 74
Table 3.4 Top Wind Speeds and Accompanying Life Used at Fowley Rocks, FL, Without Hurricane Winds 75
Table 3.5 Top Wind Speeds and Accompanying Life Used at Fowley Rocks, FL, Including Hurricane Winds 75
Table 3.6 Chicago, IL Safety Factors Corresponding to 50 Year Service Life 81
Table 3.7 Fowley Rocks, FL Safety Factors Corresponding to 50 Year Service Life With No Hurricane 82
Table 3.8 Fowley Rocks, FL Safety Factors Corresponding to 50 Year Service Life With Hurricane 82
Table 3.9 Relation Between Probability of Failure and Safety Index 83

CHAPTER 1 INTRODUCTION

This thesis has been written in the form of two independent articles, although some modification and reduction may be required to finalize them for submission to appropriate journals. The first article presents the experimental procedure and data analysis performed during a year-long study to characterize the performance of 3M's VHB structural glazing tape. The second article presents a simple linear damage accumulation model based on the findings of the first article.

The broad goal of this study was to investigate time-dependent failure of VHB tape. This investigation was important because VHB tape is used to attach structural glazing panels and resist the tensile stresses induced by wind loading over many years. A viscoelastic material such as VHB tape can demonstrate substantial resistance to stress applied and removed quickly; however, VHB tape is vulnerable to creep failure from low-magnitude, long-duration stresses. This is especially true for a viscoelastic material like VHB tape that is employed at temperatures in the vicinity of its glass transition, T_g.

Another form of delayed failure is the accumulation of fatigue damage. Wind loading has a strong fatigue component; however, characterization of VHB tape in response to fatigue was not performed in this study at the recommendation of 3M. Instead, this study focused specifically on the sustained, long-duration component of wind loading. Several other fatigue studies have been performed on VHB tape. The description and results of these studies are discussed in the introduction to Chapter 3.

To accomplish the research goals of this study, the first article (Chapter 2 of this document) describes experimental testing performed on G23F VHB structural glazing tape. In addition to VHB tape specimens, three structural silicone sealants were tested to compare these competing structural glazing products. Shear and tensile creep rupture testing was performed on bonded VHB tape and silicone sealant specimens at three temperatures to establish the relation between static load and time to failure. Ramp-to-fail tests were performed on VHB tape and silicone sealant specimens at three temperatures to establish the relation between controlled rates of strain and load resistance. Dynamic mechanical analysis (DMA) was performed on VHB tape specimens over a range of temperature and loading frequencies to establish constitutive

properties that could be shifted, by means of the time temperature superposition principle, to form master curves using shift factors that were modeled using the Williams-Landel-Ferry (WLF) equation. These thermal shift factors were also applied to multi-temperature VHB tape creep rupture and ramp-to-fail data.

The established design method for glazing with VHB tape uses one design value to define the maximum allowable static load and one design value to define the maximum allowable dynamic load. These design values, provided by 3M, incorporate a safety factor of five (3M Technical Guide 2007). The dynamic load generally corresponds to a maximum expected three-second gust wind speed over a desired return period (ASCE 7-05). This design method is straightforward, efficient, and conservative, but does not account for the accumulation of intermediate loads. Examination of intermediate loads can provide additional insight into the design of VHB tape for glazing.

The second article (Chapter 3 of this document) proposes a design framework to account for the accumulation of sustained, wind-induced stresses. This was done through a simple linear damage accumulation model which incorporated the shifted creep rupture master curve, a wind speed history, and the wind design section of the ASCE 7-05 building design code. The model provided an approximation of the fraction of life used, given length of desired service life, geographic location, VHB tape width, window size, and other design parameters. This damage model was proposed as a framework for examining the accumulation of damage from sustained wind loads, and has not been validated with experimental evidence. While this exploratory analysis generated useful conclusions, it should not be interpreted as a design manual.

Supplementary results and insights are included in the appendix. These include a side study which investigated the effect of interrupted loading on residual strength (adhesive tape healing), DMA-generated constitutive properties useful for finite element computer analysis, a discussion of the effects of thermal expansion on VHB tape structural glazing installations, an operating manual for the 72-station pneumatic load frame used to generate the creep rupture data, supplementary DMA data, a description of the Teflon jig used to cast the silicone specimens, a description of the bending jig used to prepare the silicone single lap shear specimens, tabulated ramp to fail data, and a side study on VHB tape moisture uptake.

CHAPTER 2 CHARACTERIZATION OF ACRYLIC FOAM TAPE FOR BUILDING GLAZING APPLICATIONS

ABSTRACT

This article presents the results of testing conducted to characterize the performance of 3M™ VHB™ structural glazing tape in both shear and tension. Creep rupture testing results provided the failure time at a given static load and temperature, and ramp-to-fail testing results provided the ultimate load resistance at a given rate of strain and temperature. Parallel testing was conducted on three structural silicone sealants to compare performance. Using the time temperature superposition principle, master curves of VHB tape storage and loss moduli in shear and tension were developed with data from a dynamic mechanical analyzer (DMA). The thermal shift factors obtained from these constitutive tests were successfully applied to the creep rupture and ramp-to-fail data collected at 23°C, 40°C, and 60°C (73°F, 104°F, and 140°F), resulting in master curves of ramp-to-fail strength and creep rupture durability in shear and tension.

INTRODUCTION

3M's VHB structural glazing tape consists of a closed-cell acrylic foam core with an acrylic adhesive on both sides (3M Technical Guide 2007). The tape investigated in this study, designated G23F, was developed by 3M to attach curtain wall glazing panels to building facades. This function is commonly performed by structural silicone sealants, although a similar VHB structural glazing tape has been successfully used in this capacity in South America since 1990 (3M Technical Guide 2007). To date, VHB tape has been used as a structural glazing adhesive on buildings in countries including the USA, Germany, Brazil, Israel, India, and Thailand (Austin, 2008). The load resistance of VHB tape is highly dependent on the rate or duration of loading, providing higher resistance in response to dynamic loads but being quite limited when subjected to sustained loads. Because of this property, glazing installations utilizing VHB tape are designed so that the dead load of the glazing is primarily supported through other means. VHB tape provides resistance to the action of wind loads pulling or pushing on the glazing,

while also retaining the compliance required to accommodate differential thermal expansion of the glazing components.

VHB tapes have been the subject of several third-party studies. Winwall Technology Pte Ltd performed tests including ASTM E283 air infiltration, ASTM E331 water penetration, and ASTM E330 maximum structural wind load, with a focus on very high loading over short durations of ten seconds and one minute (3M Technical Bulletin 2007). This study found that G23F VHB tape exceeded the requirements of these structural glazing ASTM standards.

Another third-party VHB tape study was performed at Michigan Technological University (Heitman 1990).This study examined five VHB tapes similar to G23F. Along with long-term shear and tensile creep rupture tests, the study investigated UV light resistance, water resistance, and tensile full-reversal cyclic fatigue. The study concluded that the controlling design factor for the tapes tested was sustained creep load endurance limits.

3M (Kremer 2005) had also investigated the long-term static load resistance of several VHB tapes similar to the G23F that is specifically investigated in this study. These creep rupture studies have established a short-term dynamic maximum design strength of 85 kPa (12 psi), and a long-term static maximum design strength of 1.7 kPa (0.25 psi) (3M Technical Guide 2007).

This study was designed to address the effect of a wide variety of loading rates (through ramp-to-fail testing) and durations of static load (through creep rupture testing) such as might be experienced by VHB tape used in the field and subject to wind loading. These durability tests were comparable to those performed by Kremer (2005) and Heitman (1990) on similar VHB tapes, although this study supplemented strength and durability test data with use of the time temperature superposition to combine results collected at several temperatures, effectively extending the time range of the experiments. Results could provide insights into the robustness of VHB tape for glazing applications and lead to an improved understanding for design purposes.

In addition to VHB tapes, three structural silicone sealants were tested to provide a direct comparison of these two methods for attaching glazing panels. The structural silicones tested were a one-component sealant (Dow Corning 995), a two-component sealant (Dow Corning 983), and another one-component sealant (Dow Corning 795). For simplicity, in tables and charts, these materials are labeled S1, S2, and S3, respectively.

Dynamic mechanical analysis (DMA) testing was performed to determine viscoelastic properties specific to VHB G23F tape and to develop shift factors for the generation of time temperature superposition (TTSP) master curves. These curves consist of elevated temperature tests shifted to simulate longer loading times, and low-temperature tests shifted to simulate shorter loading times.

Creep rupture tests were performed to examine the effect of several static loads on the time required to fail VHB tape and silicone sealant specimens. These tests were performed in large batches on a 72-station pneumatic test frame, which only records the time of complete failure. The creep rupture tests investigated the long-term response of the materials (minutes to months). Shift factors determined from DMA constitutive data produced smooth master curves of creep rupture data, which predicted results on a long-term time scale that would have otherwise been beyond the time scope of this research project.

Ramp-to-fail tests were performed with several constant strain rates and temperatures to examine their effects on tensile and shear strength of VHB tape specimens. These tests were performed individually on an Instron test frame, which records the resisting force as a specimen is loaded at a prescribed crosshead rate. These tests investigated the short-term response of the material (seconds to minutes), and strength master curves were again constructed using the shift factors determined from DMA constitutive data.

EXPERIMENTAL

DMA

Dynamic mechanical analysis (DMA) testing was performed on VHB G23F tape (lot # 97278) using a TA Instruments 2980 Dynamic Mechanical Analyzer. The frequency sweep included 75, 31.2, 10, 3.2, and 1 Hz, which are evenly spaced on a logarithmic scale. The applied temperatures ranged from -50°C to 150°C (-59°F to 302°F), using 10°C (18°F) increments. In order to examine the effect of temperature history on the specimen, some test replicates were initiated at the low end of the temperature range and progressed to the higher temperature, and some test replicates were performed in the reverse manner. The applied strain amplitudes for various test geometries and temperature ranges are presented in Table 2.1. The selected amplitudes produced specimen dynamic resistances from 0.01 N to 12 N, which were between the lower limit of recording capability and the upper limit of loading capability of the apparatus. In order to prevent the dynamic resistance from dropping below or exceeding the allowable range, the amplitude often had to be modified as the specimens were heated or cooled. No inconsistencies or unusual jumps in recoded data were observed when the amplitudes were modified during testing.

Table 2.1 Applied DMA Strain Amplitudes

Test Desigination	Relevant Specimen Dimension	Temperature Range °C	Temperature Range °F	Amplitude μm	Amplitude in.	% Strain
Shear #1	2.30 mm (0.090 in.)	-50 to 20	-58 to 68	2	0.00008	0.087
		30 to 120	86 to 248	25	0.00098	1.087
Shear #2	2.30 mm (0.090 in.)	-50 to 20	-58 to 68	2	0.00008	0.087
		30 to 120	86 to 248	25	0.00098	1.087
Compression #1	2.30 mm (0.090 in.)	-50 to 30	-58 to 86	2	0.00008	0.087
		40 to 120	104 to 248	15	0.00059	0.652
Compression #2	9.09 mm (0.358 in.)	-30 to 40	-22 to 104	5	0.00020	0.055
		50 to 150	122 to 302	40	0.00157	0.440
Long Axis Tension #1	14.72 mm (0.580 in.)	-40 to 0	-40 to 32	20	0.00079	0.136
		10 to 150	50 to 302	100	0.00394	0.679
Long Axis Tension #2	12.37 mm (0.487 in.)	-40 to 150	-40 to 302	100	0.00394	0.808

Three specimen geometries were used for the DMA testing: double shear sandwich specimens, out-of-plane compressive specimens with the load applied across the thin dimension (i.e. thickness) of the VHB tape, and in-plane tensile specimens with the load applied along the long axis or machine direction of the VHB tape. Two replicates were completed for each geometry. The strains applied during these tests were 1% or less, and so the distinction between out-of-plane compression and out-of-plane tension was assumed negligible. This assumption was necessary because out-of-plane tension was one of the loading modes of primary interest in this study; however, the closest loading mode available from the DMA apparatus was out-of-plane compression. Long axis, in-plane tension was not an important loading mode anticipated during normal use of VHB as a structural adhesive tape. The primary purpose of including it was to examine the isotropy of constitutive properties, by comparison to the out-of-plane compression geometry.

The double shear sandwich specimens were two 10 mm by 10 mm by 2.3 mm thick (0.39 in. by 0.39 in. by 0.090 in. thick) squares, mounted as shown in Fig. 2.1. In order to bond the shear specimens, the shear clamps were tightened until the specimen exhibited 20% compressive strain. After 15 seconds, the shear clamp was loosened and the specimens were allowed to relax

back to approximately the initial thickness of 2.3 mm. The compression specimens were 12.4 mm diameter by 2.3 mm thick (0.49 in. diameter by 0.090 in. thick) disks, and were bonded to the compression platens by the same method as the shear specimens. The first specimen used one disk as shown in Fig. 2.2a, while the second specimen used four disks bonded together as shown in Fig. 2.2b, which provided a total thickness of 9.2 mm (0.36 in.). The long axis tension specimens consisted of strips of VHB tape measuring 2.3 mm by 6.0 mm by 14.7 mm (0.090 in. by 0.24 in. by 0.58 in.) for the first replicate and 2.3 mm by 6.0 mm by 12.4 mm (0.090 in. by 0.24 mm by 0.49 in.) for the second replicate. Steel foil was used to anchor each end of the long axis tension specimens, as shown in Fig. 2.3a. This was done to fit the specimens to the TA Instruments film tension grip, which would not open wide enough to accommodate a specimen thickness of 2.3 mm (0.090 in.). Concerns have been raised that flexing of these foil strips may have influenced the results, but it is likely that the deformations stabilized after initial loading, and had little further effect.

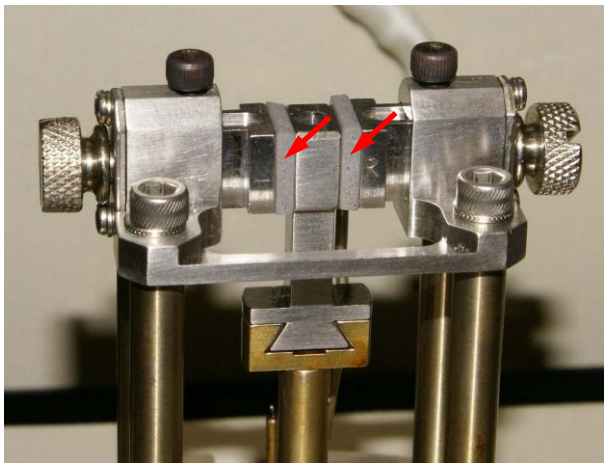

Figure 2.1 Double shear sandwich specimen; arrows indicate the VHB tape specimens.

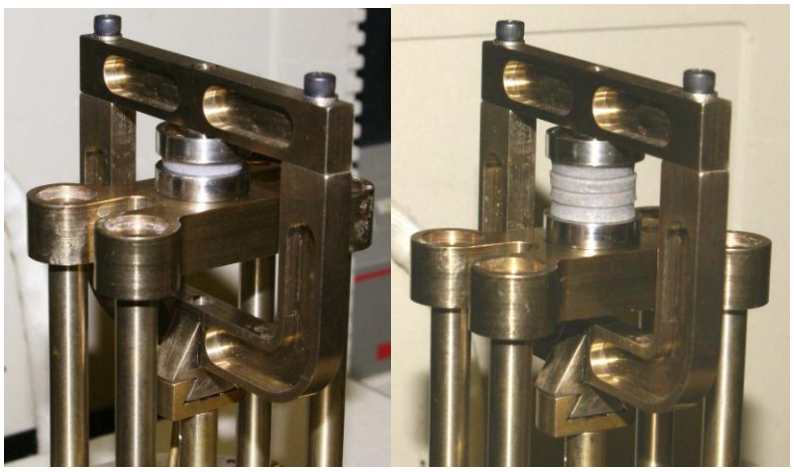

Figure 2.2 Compressive specimens showing test configurations with a) a single layer, and b) four layers of tape.

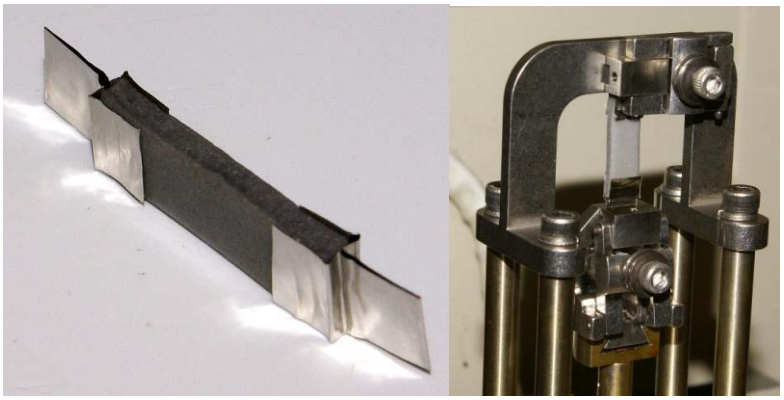

Figure 2.3 The long-axis tension a) specimen and b) grip.

Creep Rupture

The creep rupture data was gathered on a pneumatic test frame equipped with 72 Minimatic double-action air cylinders, as shown in Fig. 2.4. This test frame was originally developed and fabricated by NIST for durability testing of fiber-reinforced composites. The cylinders were capable of applying as much as 534 N (120 lbs) when shop air pressure was supplied, and could consistently and reliably apply loads as low as 68 N (15 lbs). The cylinders were divided into two banks of 36, and each bank had a pressure regulator so they could be independently controlled. If one specimen in the bank of 36 cylinders failed, the retraction of that cylinder piston did not influence the load on the other specimens, within the recording precision of the instrument. The cylinders were mounted on top of a temperature control chamber, and the

cylinder rods passed through loose, low-friction rubber seals into the chamber where they attached to the specimens. The temperature inside the chamber could be maintained from ambient to 85°C (185°F) using heater coils. Operating instructions for the 72-station creep rupture frame are included in Appendix D.

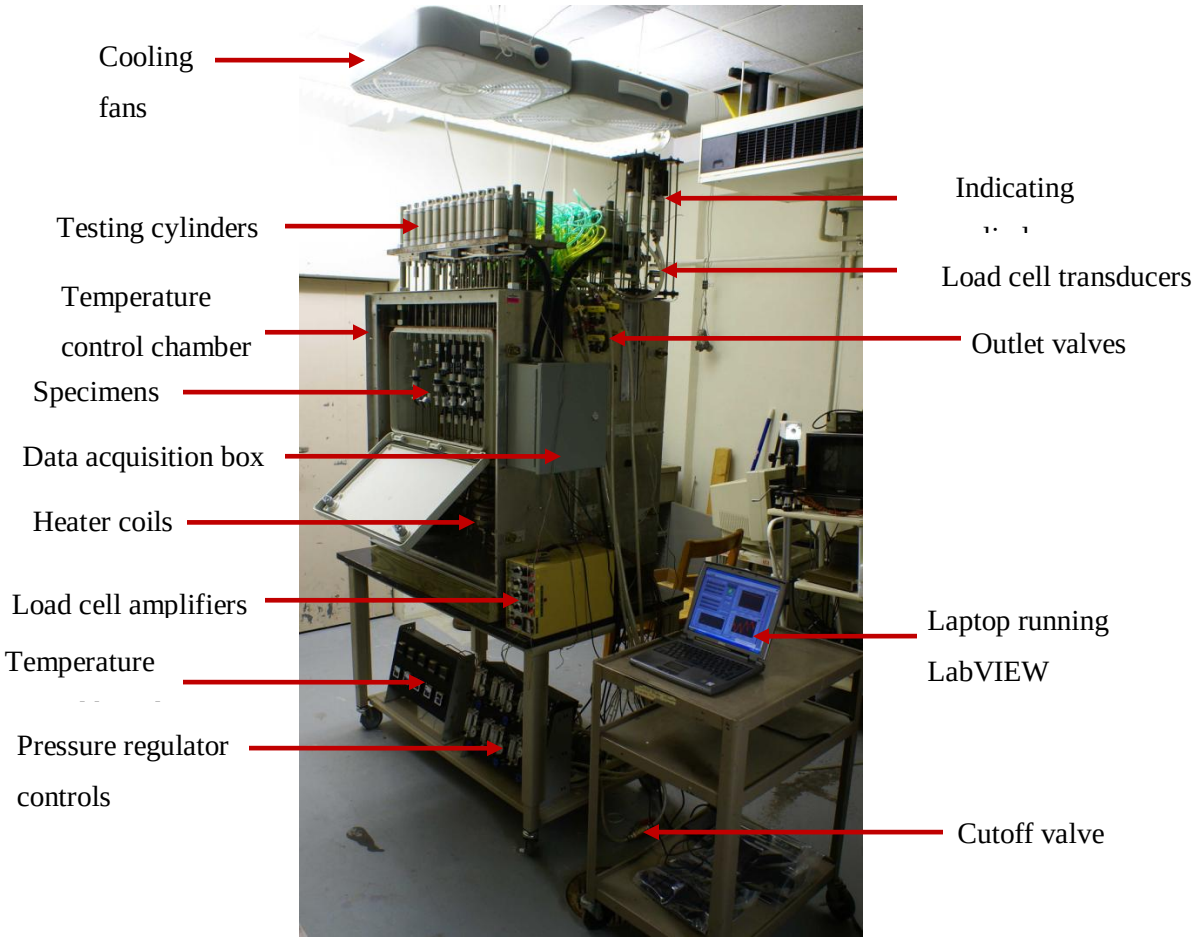

Figure 2.4 72-station test frame with front face of temperature control chamber removed.

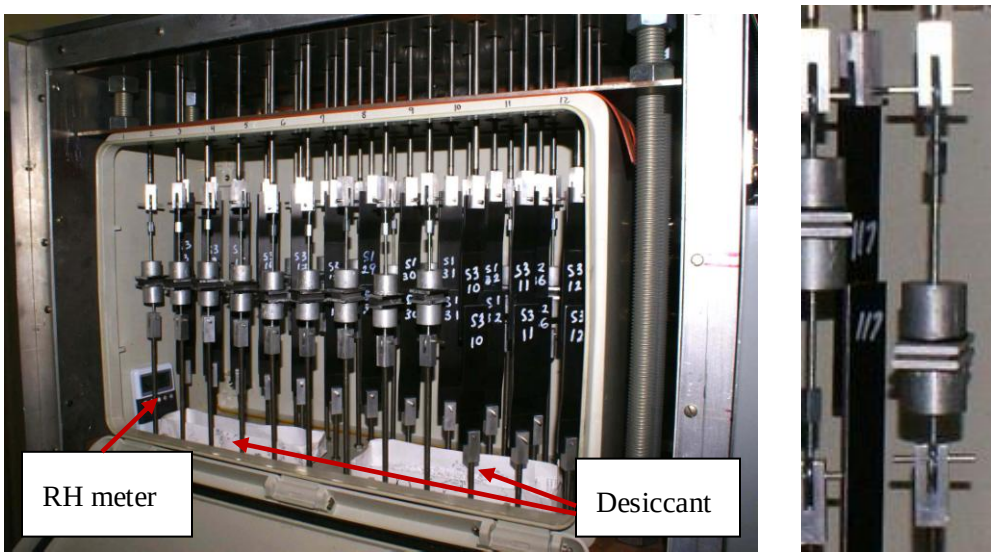

Figure 2.5 Close view of a) silicone sealant and b) VHB tape specimens mounted in the creep rupture test frame.

At elevated temperatures, the relative humidity inside the chamber was low (15%). In order to maintain a similar RH for the ambient 23°C (73°F) tests, Drierite® (a desiccant made from calcium sulfate) was placed in the chamber, which maintained the RH at 15% to 25%. The untested specimens were also stored in sealed chambers with Drierite®.

In order to record the force applied to the specimens, each 36-cylinder bank had an extra cylinder that was mounted outside the test chamber but was connected to a common pressure manifold. These two indicator cylinders were attached to load cell transducers, and these readings represented the load applied to the specimens.

The temperature of the loading cylinders affected their applied load. Heating the external surface of a cylinder by 20°C (36°F) produced an additional load of roughly 4 N (1 lb) when the cylinder was applying 222 N (50 lb) of load. The exact cause of this effect was not determined, although the possibility that temperature was simply influencing the load cell transducer was examined and rejected. When the test frame was run at 60°C (140°F), heat would conduct up the cylinder rods and increase the temperature of the cylinders. This could have created inaccuracies during recording of the applied load, because the two indicator cylinders did not have rods extending into the temperature chamber, and so did not receive conducted heat. This issue was resolved with two fans mounted above the test frame. Air circulation lowered the temperature of the

loading cylinders to match the indicator cylinders. The assumption that the indicator cylinders represented the load applied by the loading cylinders was verified by attaching a load cell to several of the loading cylinders inside the temperature chamber, and comparing those values to the indicator cylinder. Cylinder to cylinder variation in applied load was about 4 N (1 lb), regardless of chamber temperature.

The cylinders were set to pull on the tensile or shear specimens with a constant load until the specimens failed. Failure was recorded when the specimen pulled apart, and the cylinder rod retracted two inches upwards until it encountered the end of the piston travel and engaged a switch. The time of failure for each specimen was logged with a LabVIEW program running on a dedicated laptop computer. The LabVIEW programming and installation of failure switch instrumentation was performed by Pico Systems of Blacksburg, VA. Indicator cylinder loads and temperatures were also collected on a time increment, which could be modified while the tests were running. During a test run, some specimens would fail within a short period, and other specimens would fail within a period several orders of magnitude larger. For example, shear VHB tape specimens usually failed one order of magnitude later than tensile VHB tape specimens did, and those specimen geometries had to be tested simultaneously. To prevent the generation of excessively large data files, the time increment for data recording was set higher as the test progressed. The laptop computer was connected to the internet, and the LabVIEW program provided remote viewing as the test progressed, with a display of specimen status and plots of load and temperature versus time.

The specimens used in both creep rupture and ramp-to-fail tests simulated an aluminum-to-aluminum bond, accomplished by sandwiching the structural silicone sealant or VHB tape between two 3.2 mm (0.13 in.) thick anodized aluminum adherends, as shown in Fig. 2.6 and Fig. 2.7.

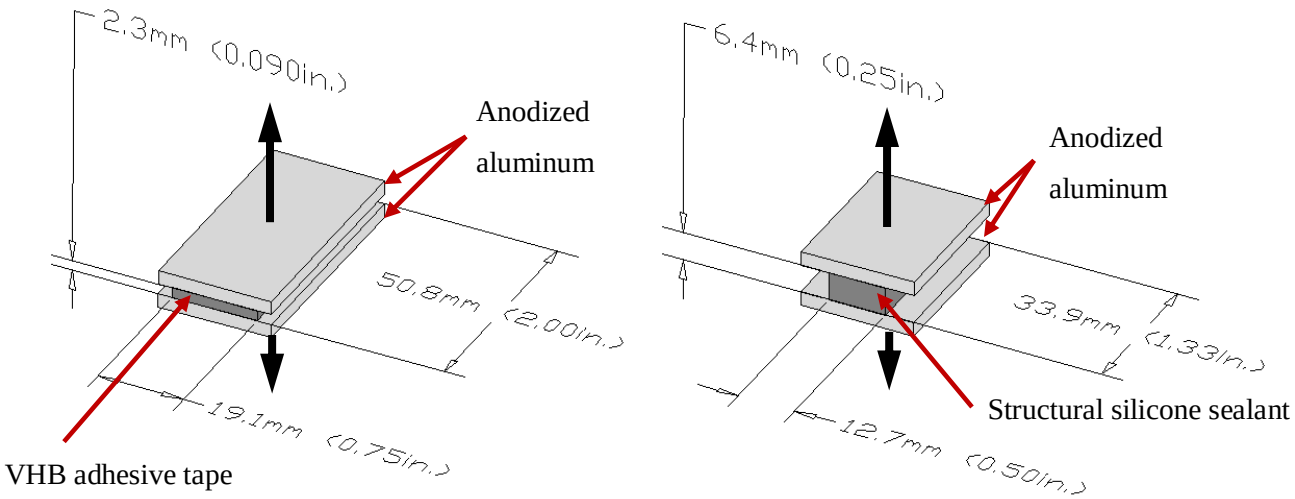

Figure 2.6 Butt tensile joint specimens.

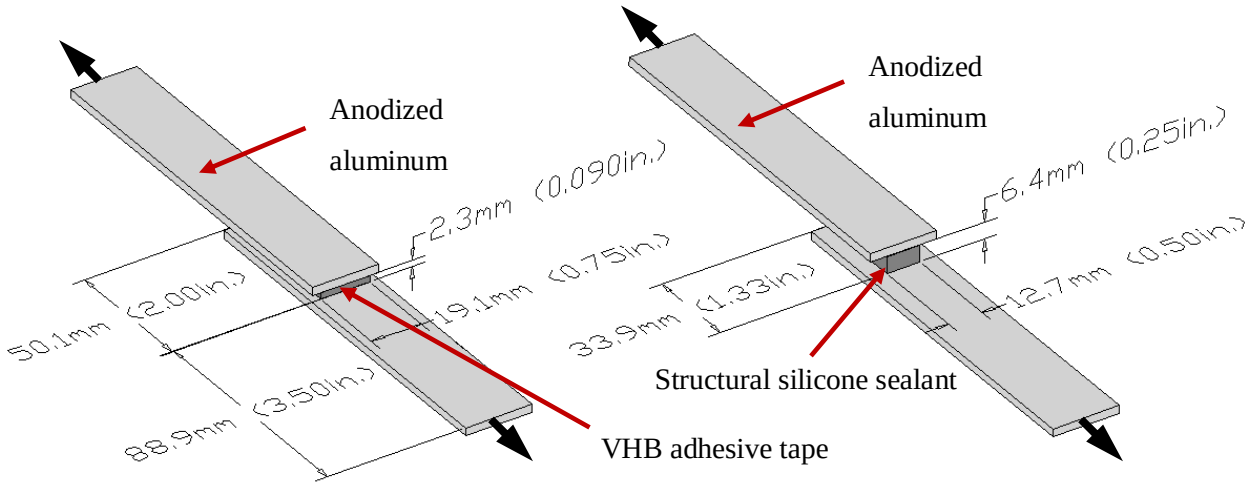

Figure 2.7 Single-lap shear joint specimens.

Specimen bond areas and dimensions were made to emulate real-life applications of these products, as well as sized to fit the limitations of the testing equipment. The 50.1 mm (2.00 in.) length of VHB tape specimens was the maximum length possible in order to fit 72 specimens into the creep frame shown in Fig. 2.4. The 19.1 mm (0.75 in.) width of the VHB tape is a common size used in structural glazing applications. This resulted in a VHB tape bond area of 1290 mm^2 (2.0 in^2). The smaller 33.9 mm by 12.7 mm (1.33 in. by 0.50 in.) dimensions of the structural silicone specimens maintained the same aspect ratio as the VHB tape specimens, although with the reduced bond area of 430 mm^2 (0.667 in^2).The dynamic design strength of the

VHB adhesive tape is 85 kPa (12 psi) (3M Technical Guide 2007), while the generally accepted industry standard dynamic strength of structural silicone sealant is 138 kPa (20 psi). By using appropriately ratioed bond areas for the two materials, the given load levels produced by the pneumatic cylinders loaded each material to a similar multiple of the respective design strength. This resulted in failure times that were closer for the two materials, and ensured that the loads required to fail the two materials were within the capabilities of the test frame. The 6.35 mm (0.25 in.) structural silicone thickness was selected as a common dimension used in construction. The 88.9 mm (3.50 in.) length of the adherends, which extended above and below the shear specimen bond area, was chosen to be similar to the specimen geometry of ASTM D 1002-05, which is the ASTM standard for adhesive metal-to-metal single-lap shear joint tests.

The 72-station pneumatic test frame could apply between 68 N (15 lbs) and 534 N (120 lbs). For the VHB adhesive tape bond area, this converted to a stress range of 10 psi (69.0 kPa) to 80 psi (552 kPa). For the structural silicone bond area, the stress range was 22.5 psi (155 kPa) to 180 psi (1.24 MPa).

The initial bonding of VHB tape specimens and casting and curing of structural silicone specimens was performed by 3M at their St. Paul, Minnesota facility, with the exception of the 2-component DC 983 structural sealant, which was cast by a company specializing in window glazing. The VHB tape used for creep rupture testing came from the same lot (#97278) as the tape used for DMA testing. The S1 silicone specimens (one-component DC 995 sealant, lot #0002703434) were allowed at least ten days of initial curing in a 21°C (70°F) and 50% RH controlled environment, and were tested between one and seven months after creation. The S2 silicone specimens (two-component DC 983 sealant, base lot #2349299, catalyst lot #4395070) were allowed at least three days of initial curing under controlled conditions, and were tested 17 days to six months after creation. The S3 silicone specimens (one-component DC 795 sealant, lot #0004969524) were allowed 18 days of initial curing under controlled conditions, and were tested two to three months after creation. According to the Dow Corning Americas Technical Manual (Dow Corning 2007), the one-component structural sealants (S1 and S3) require 7 to 14 days of cure time, and the two-component structural sealant (S3) requires 24 hours of cure time, all at ambient conditions.

VHB tape specimens were bonded to the two anodized aluminum adherends using the following procedure:

1. Adherends were cleaned with a 1:1 ratio of isopropyl alcohol and water.
2. Adherends were primed with a thin layer of 3M Primer 94 and allowed to dry for one or two minutes.
3. Tape was applied to the first adherend with care to avoid creation of air voids.
4. At least 15 psi of pressure was applied to the tape with a J-roller.
5. The protective liner was removed from the VHB tape and the second adherend was carefully bonded to the tape.
6. Pressure was applied again.
7. Bonded specimens were allowed to dwell for at least 72 hours at 21°C (70°F) and 50% RH in an RH controlled chamber.

Silicone specimens were bonded to the anodized aluminum adherends using the following procedure:

1. Adherends were cleaned with a 1:1 ratio of isopropyl alcohol and water.
2. Adherends were placed in a 22-specimen Teflon jig designed to space them apart consistently and accurately, leaving a 33.9 mm by 12.7 mm by 6.35 mm (1.33 in. by 0.50 in. by 0.25 in.) cavity to be filled with silicone sealant. See Appendix F for a description of the Teflon jig.
3. Silicone was injected into the cavity, starting at one end and moving slowly to the other, with the nozzle held half-way down into the cavity. The silicone was allowed to overfill the edges as the nozzle progressed.
4. Excess silicone was removed with a Teflon tool, leaving the required gap of ¼ in. between the adherend edge and the face of the silicone.

The bonded VHB tape and structural silicone specimens were then shipped to Virginia Tech, where they were placed in a container with desiccant. Immediately before testing, some further

specimen preparation was necessary. As shown in Fig. 2.8, the butt-joint tensile adherends were bonded with epoxy to two aluminum cylinders, drilled, and tapped to accept eye screws for mounting in an Instron load frame or the 72-station creep frame. The modified single-lap shear joints, shown in Fig. 2.9, were drilled at each end so that a pin could secure them into the test frame devices.

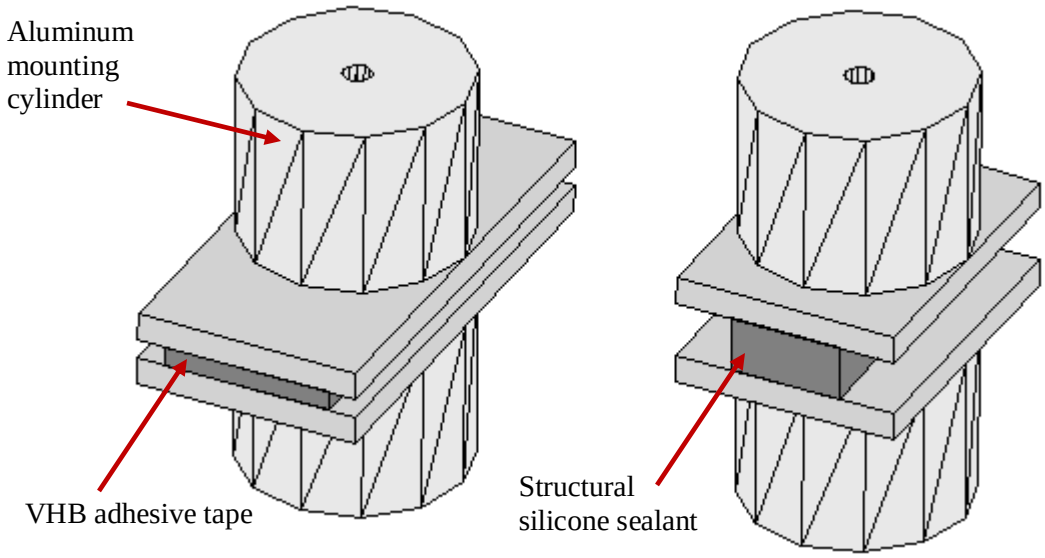

Figure 2.8 Butt joint tensile specimens, modified for mounting in test frame.

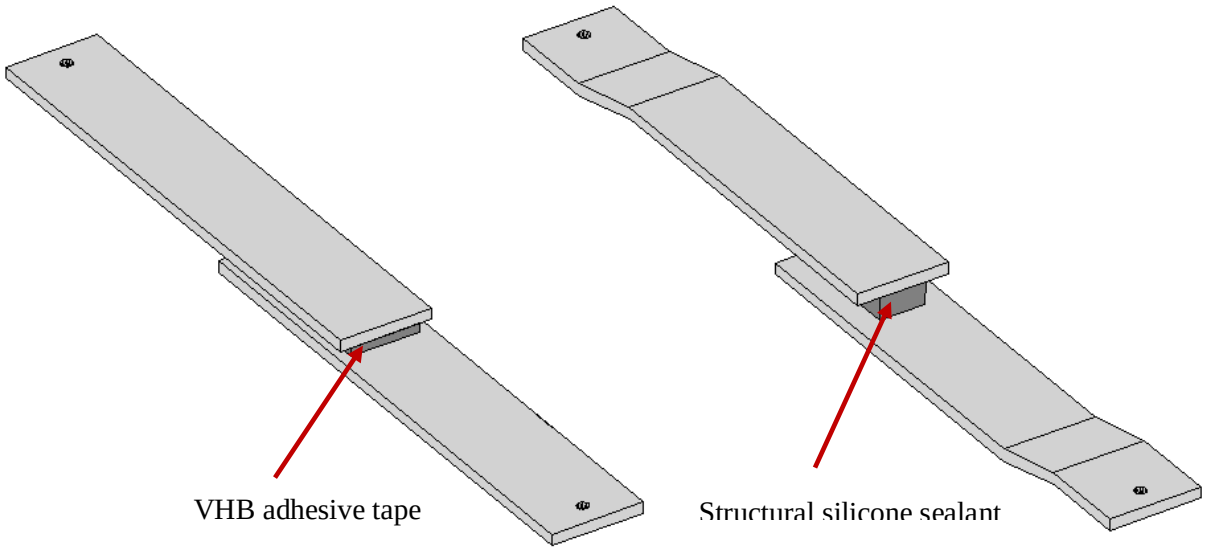

Figure 2.9 Single-lap shear joint specimens, modified for mounting in test frame.

The offset between the adherends of the silicone shear joints were sufficiently thick so that those specimens did not fit easily between the devices of the 72-station creep frame. This generated bending moments in the pneumatic cylinder pistons and rods, resulting in excess friction and rubbing. This problem was reduced by applying an s-bend above and below the specimen bond area, as shown in Fig. 2.10. A simple bending jig was assembled in order to produce consistent s-bends in the adherends by using a vise. More information about the bending jig is included in Appendix G. The VHB tape specimens were thin enough so that s-bends were not necessary.

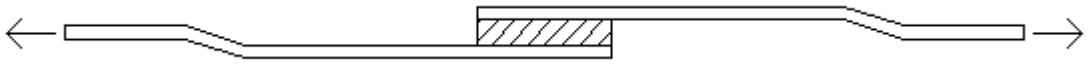

Figure 2.10 S-bends in silicone single-lap shear joint improve the alignment and avoid applying bending moments to the rods of the air cylinders.

Ramp-to-Fail

Constant strain rate ramp-to-fail tests were performed on VHB tape and silicone sealant specimens using an Instron 5800R load frame fitted with a Thermotron temperature control chamber. The Thermotron chamber was a convection oven with openings in the top and bottom for the grip pull rods to pass through. These tests used the same type of shear and tensile specimen geometries and anodized aluminum adherends as the creep rupture tests. Three rates of

strain were used: 5 mm/min (0.197 in./min), 50 mm/min (1.97 in./min), and 500 mm/min (19.7 in./min). The VHB tape specimens were tested at the same three temperatures used for the creep rupture tests: 23°C, 40°C, and 60°C (73°F, 104°F, and 140°F). Temperature was measured with a built-in thermocouple, as well as a thermometer placed inside the chamber. The test temperatures were accurate to approximately ±1°C (1.8°F). The elevated-temperature specimens were allowed to equilibrate for at least 30 minutes prior to testing. The S1, S2, and S3 structural silicones (one-component DC 995 sealant, two-component DC 983 sealant, and one-component DC 795 sealant) were tested at ambient 23°C (73°F) only, resulting in an equal number of silicone sealant and VHB tape specimens. Each set of conditions was replicated with three specimens.

The test chamber was not humidity controlled. At ambient 23°C (73°F) the relative humidity inside the chamber was between 65% and 80%, at 40°C (104°F) the RH was 29%, and at 60°C (140°F) the RH was 9%. However, in the weeks prior to testing, the VHB tape specimens were stored in sealed containers with Drierite®, which maintained RH at 15% to 25%. Specimens were removed from the storage containers for no more than 20 minutes before testing took place. This length of time should not have permitted significant moisture uptake, based on a short side study of moisture mass uptake (see Appendix I).

The VHB tape used for ramp-to-fail testing came from the same lot (#97278) as the tape used for DMA and creep rupture testing. The S1 silicone specimens (one-component DC 995 sealant, lot #0002703434) were fabricated by 3M in a separate batch than the S1 specimens used for creep rupture testing, although the lot number was the same. These S1 specimens were allowed 16 days of initial curing in a 21°C (70°F) and 50% RH controlled environment, and were tested eight months after creation. The S2 silicone specimens were from the same batch as those tested in creep rupture (two-component DC 983 sealant, base lot #2349299, catalyst lot #4395070). They were allowed at least three days of initial curing under controlled conditions and tested nine months after creation. The S3 silicone specimens (one-component DC 795 sealant, lot #4969524) were allowed 18 days of initial curing under controlled conditions, and were tested four months after creation.

RESULTS AND DISCUSSION

DMA

The purpose of the DMA testing on G23F VHB tape was to develop, using the time temperature superposition principle, smooth master curves of storage (E' and G') and loss (E" and G") moduli along with appropriate thermal shift factors, as well as to determine the value of the glass transition temperature (T_g). The value of T_g is useful information in itself, and the constitutive properties should be valuable for stress analysis, including finite element analysis modeling (see Appendix B for finite element input terms). However, the benefit of DMA testing that was most relevant to the rest of this research effort was generation of thermal shift factors used to shift creep rupture data to form creep rupture master curves.

The master curves of shifted constitutive data were generated by adjusting the constants in the Williams-Landel-Ferry (WLF) equation to produce thermal shift factors to match the shift factors generated in forming the master curves. The first step in this process was to display the raw data on a plot of log E' or log G' versus log frequency. The raw data consists of a series of loading frequency sweeps from 1 Hz to 75 Hz, performed at various temperatures. The data was then shifted by eye by adding or subtracting a shift factor ($\log a_T$) from the log frequency values to align each frequency sweep into a single smooth curve. Lower-temperature data was shifted to simulate high-frequency tests, and high-temperature data was shifted to simulate long-term, low-frequency tests. This manual shifting was performed for each separate DMA test run, and the resulting shift factors from separate test geometries were averaged at each temperature interval. The -50°C to -30°C (-58°F to -22°F) manual shift factors did not agree between specimen geometries, so this range was not included in the average manual shift factor values. The average manual shift factor values were then fit using Eq. (2.1), the WLF equation (Ward 1997):

$$\log a_T = -\frac{C_1(T - T_{ref})}{C_2 + T - T_{ref}} \tag{2.1}$$

where T is the temperature that the data is to be shifted from, T_{ref} is the reference temperature, and C_1 and C_2 are constants. The WLF-derived shift factor, log a_T, was then applied to frequency-based data by using Eq. (2.2b):

$$\omega_{ref} = \omega \cdot a_T \tag{2.2a}$$

$$\log \omega_{ref} = \log \omega + \log a_T \tag{2.2b}$$

The shift factors were applied to time-based data by using Eq. (2.3b):

$$t_{ref} = \frac{t}{a_T} \tag{2.3a}$$

$$\log t_{ref} = \log t - \log a_T \tag{2.3b}$$

A discussion of the original development and rationale behind the WLF equation can be found in the text by Ferry (1980).

The reference temperature T_{ref} was set to 30°C (86°F), because that was one of the experimental DMA temperature levels. The process of shifting data manually requires a starting reference temperature at which data was actually collected. VHB tapes used to attach structural glazing would also commonly experience 30°C (86°F), giving the master curves based on that reference temperature a practical value. Using T_{ref} = 30°C (86°F), least squares regression was performed by minimizing the difference in log frequency between the WLF equation and the average of the manually determined shift factors. The resulting constants were C_1 = 9.98 and C_2 = 132.6°C (238.7°F), and these were used in the equation that was employed to generate the master curves displayed in this document. Fig. 2.11 displays both the manual shift factors and the resulting WLF best-fit curve at a reference temperature of 30°C (86°F). WLF constants for other reference temperatures are listed in Table 2.2. Note that as the reference temperature decreases toward the glass transition temperature, the WLF constants move toward traditional values reported for viscoelastic polymers, such as the "universal constants" of C_1 = 17.4 and C_2 = 51.6°C (92.9°F) when $T_{ref} = T_g$ (Aklonis and MacKnight 1983).

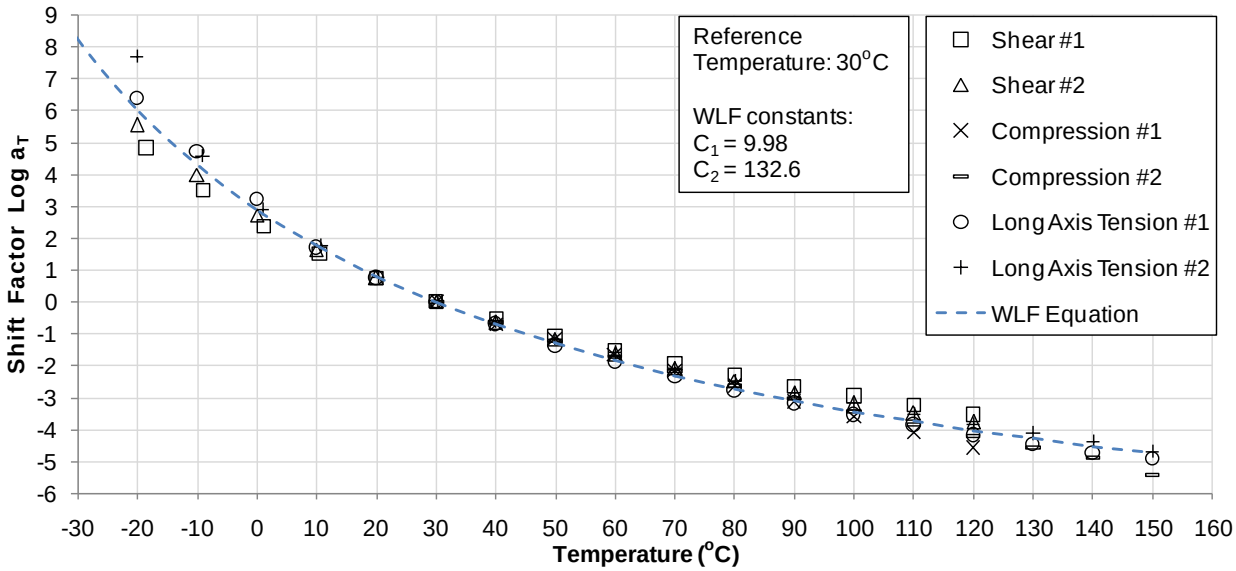

Figure 2.11 Storage modulus was shifted manually to 30°C (86°F) reference temperature and then fit with the WLF equation using least-squares regression.

Table 2.2 WLF Constants for Various Reference Temperatures

Reference	C_1	C_2
30°C (86°F)	9.98	132.6°C (238.7°F)
20°C (68°F)	10.42	118.9°C (214.0°F)
10°C (50°F)	11.18	108.1°C (194.6°F)
0°C (32°F)	12.96	109.1°C (196.4°F)
-10°C (14°F)	15.34	112.7°C (202.9°F)
-20°C (-4°F)	17.09	97.1°C (174.8°F)

The resulting storage and loss moduli master curves, shown in Fig. 2.12 and Fig. 2.13, vary in their internal consistency (specimen to specimen) and external consistency (across the three test configurations) depending on the test geometry employed.

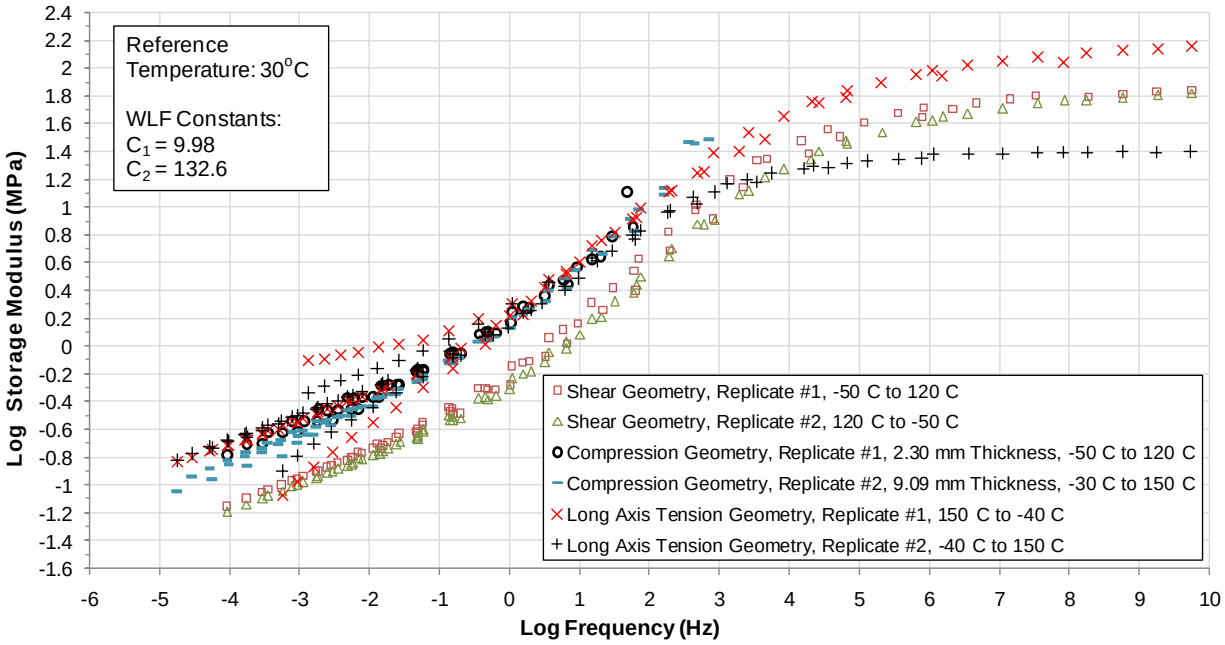

Figure 2.12 G23F storage modulus master curve at 30°C (86°F) reference temperature and using WLF shift factors with C1 = 9.98 and C2 = 132.6.

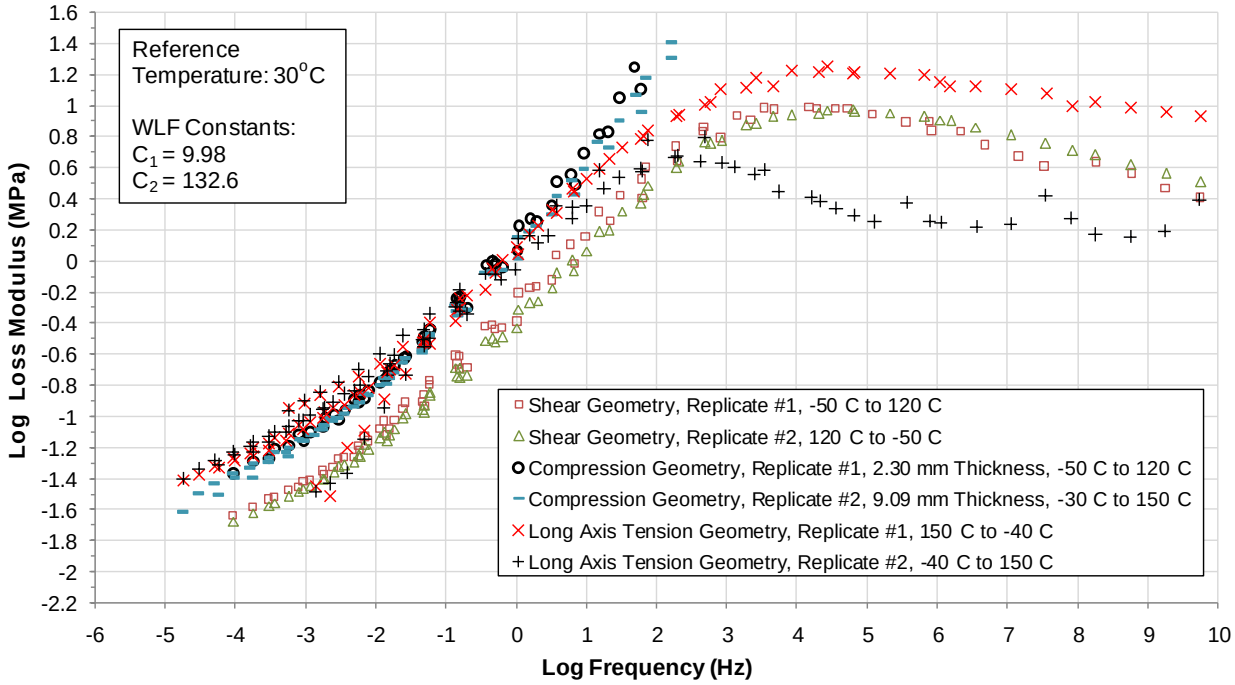

Figure 2.13 G23F loss modulus master curve at 30°C (86°F) reference temperature and using WLF shift factors with C1 = 9.98 and C2 = 132.6.

The shear geometry demonstrated internal consistency, as the two replicates produced similar curves. The shear storage modulus changed by roughly three decades as it passed through the glass transition, which was consistent with typical amorphous polymers (Aklonis and MacKnight 1983). The shear geometry master curves are shown individually in Fig. 2.15 and Fig. 2.16, along with loss modulus and tangent delta as a function of temperature in Fig. 2.17 and Fig. 2.18. The variation in the storage modulus of 0.1 to 0.2 decades between the replicates can be attributed to the direction in which the tests were run. As shown in Fig. 2.14, one replicate was performed by starting at a low temperature and increasing for each frequency sweep, while the other replicate was performed in the opposite manner. The DMA machine used approximately five minutes to heat or cool by 10°C (18°F) at each temperature step, using liquid N2 for cooling. After the internal thermocouple registered the correct temperature, the specimens were allowed five minutes to reach an isothermal state before the data was recorded. This value of roughly 1°C·sec^{-1} (1.8°F·sec^{-1}) is the rate of heating recommended by ASTM standard E 1640-04. However, the data suggests that the specimens did not fully achieve the target temperatures before the data was recorded. Taking the average of the two replicates, with one running hot to cold and the other running cold to hot, is a better method to determine values of G' and G" using this data.

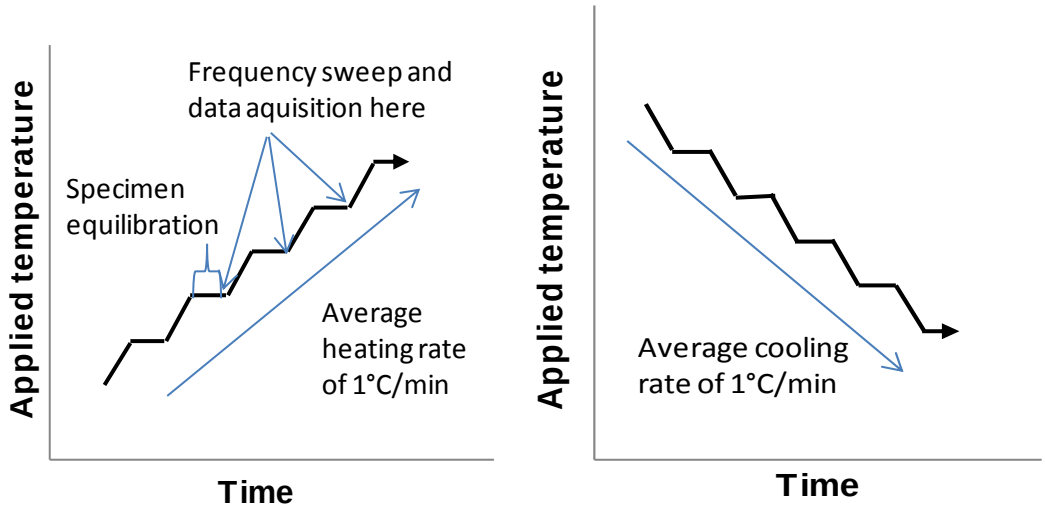

Figure 2.14 Application of temperature during DMA testing.

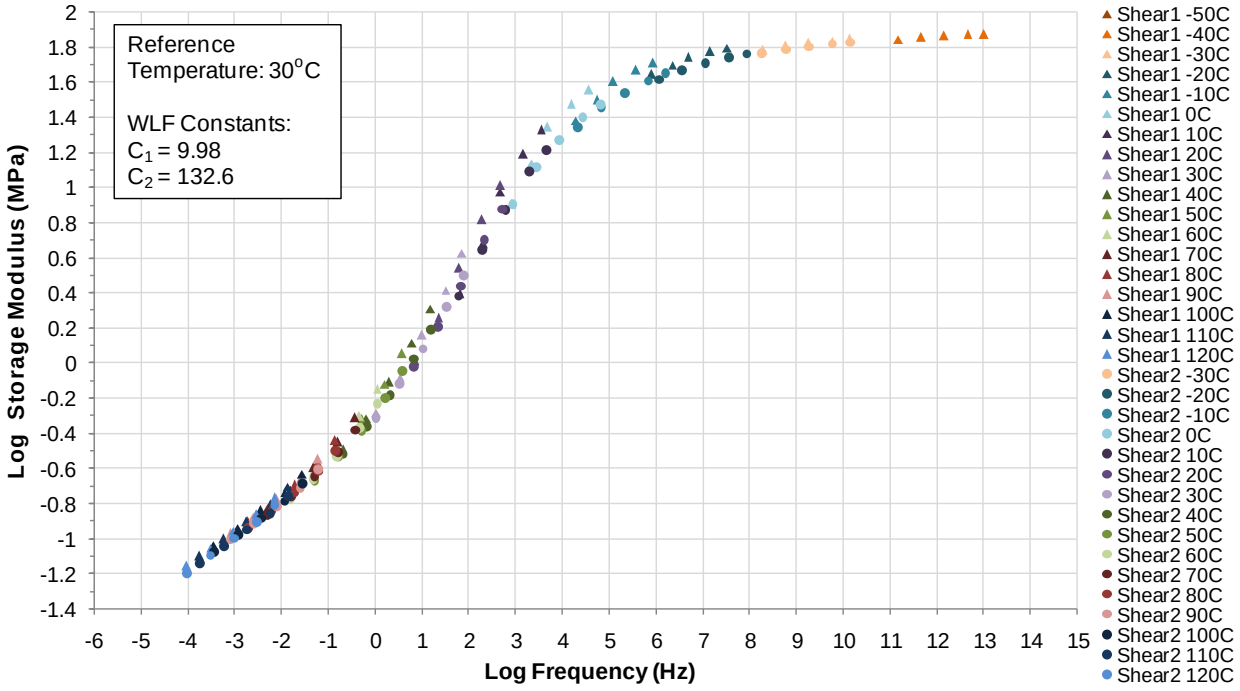

Figure 2.15 Shear geometry G23F storage modulus master curve at 30°C (86°F) reference temperature and using WLF shift factors with C1 = 9.98 and C2 = 132.6.

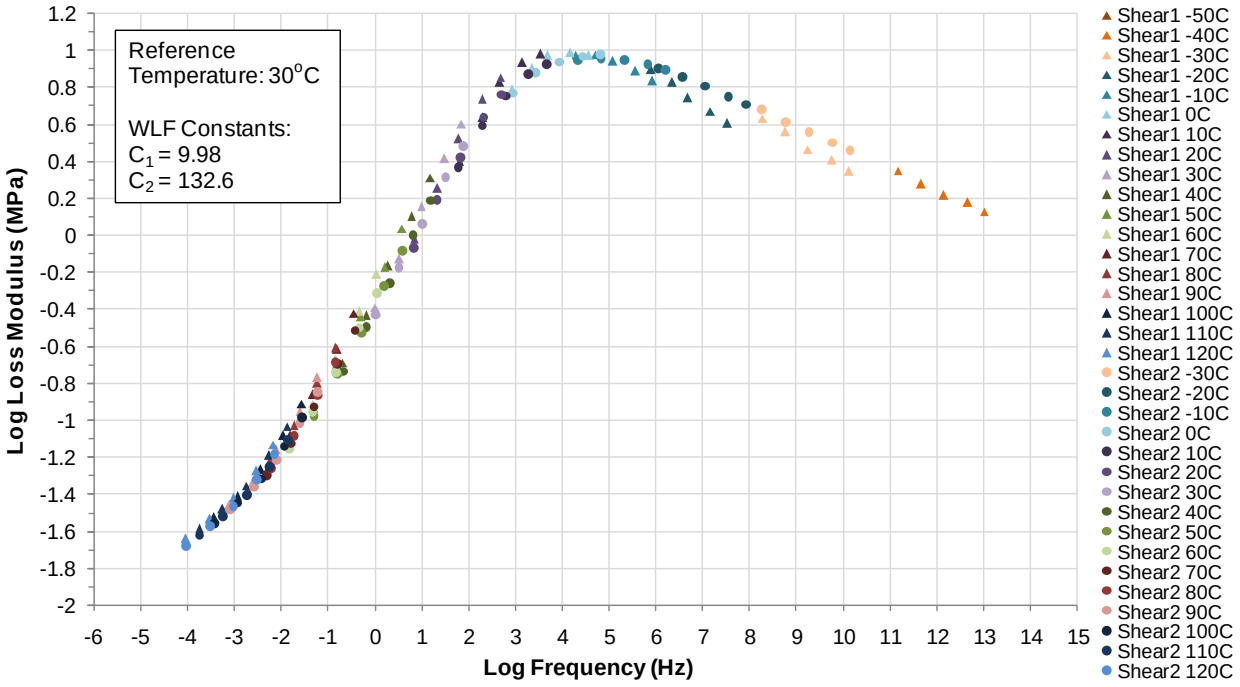

Figure 2.16 Shear geometry G23F loss modulus master curve at 30°C (86°F) reference temperature and using WLF shift factors with C1 = 9.98 and C2 = 132.6.

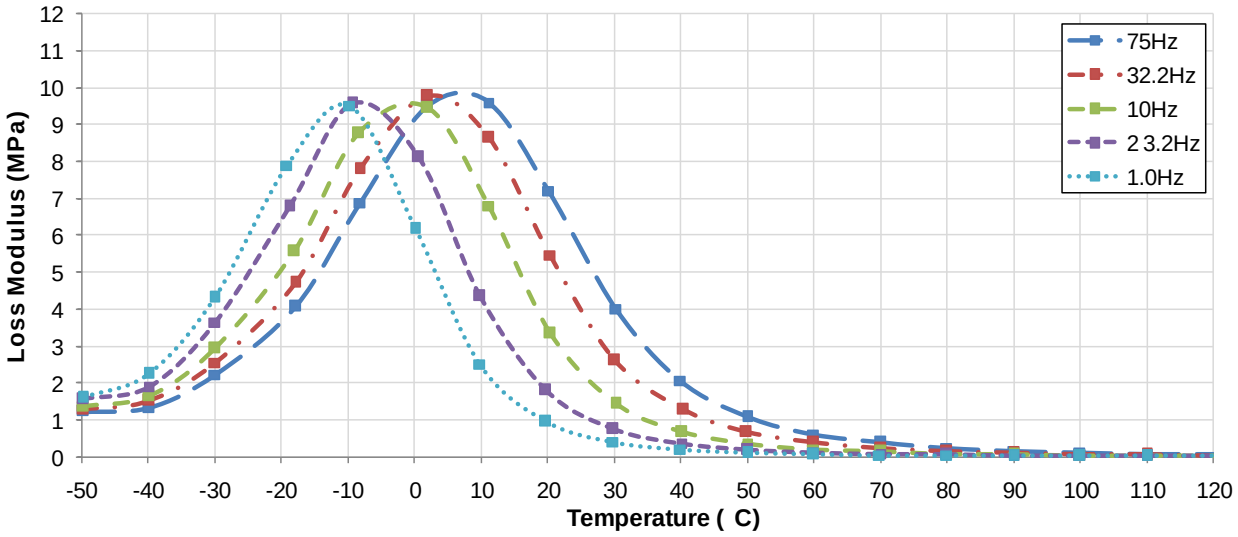

Figure 2.17 Loss modulus as a function of time from the first shear geometry replicate.

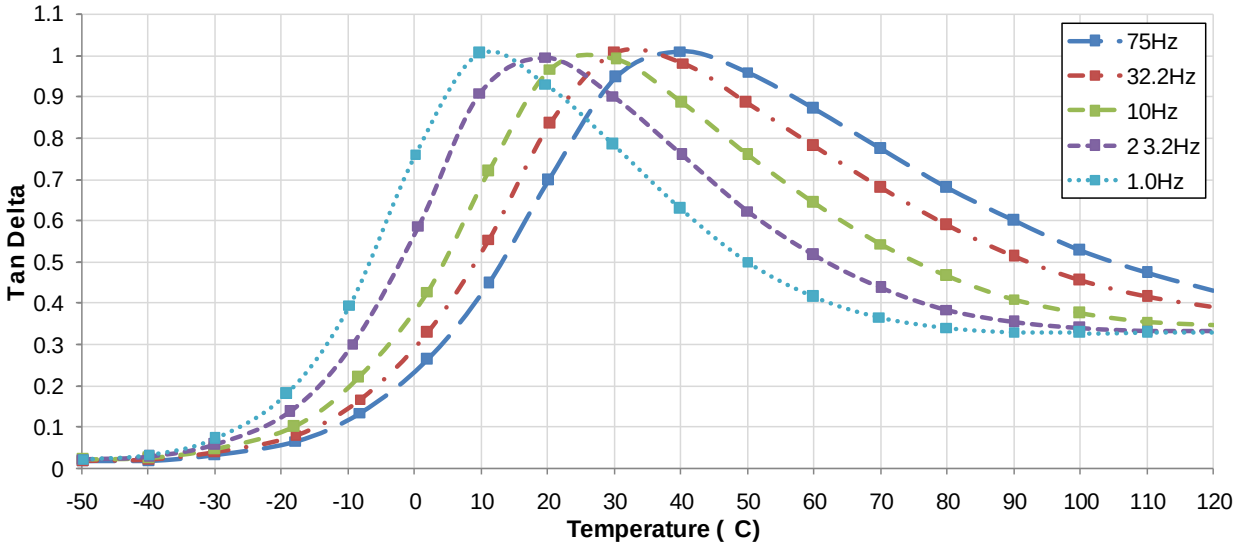

Figure 2.18 Tan delta (storage modulus over loss modulus) as a function of time from the first shear geometry replicate.

The values for storage and loss moduli determined from the compression geometry were less consistent compared to those obtained from the shear geometry. As shown in Fig. 2.19, the DMA apparatus reported a dramatic change in modulus during the glass transition. There were several reasons indicating that data from the high-frequency (> 10^3 Hz) portion of the master curve was not reliable, while the low-frequency portion remained accurate. First, the high-frequency data was not internally consistent between replicates, while the low-frequency data was. Second, the

high-frequency compression data was not consistent with the high-frequency data from the shear geometry. However, the curve of the low-frequency compression data matched the long-axis tension geometry, and was uniformly greater than shear data by a factor of E'/G'≈ 2.53 ±0.24. A useful check on this result can be performed by making the approximation that the dynamic moduli ratio *E'/G'* is equivalent to the ratio *E/G* of elastic moduli, then plugging into Eq. (2.4) which defined the relationship between these moduli and Poisson's ratio (ν):

$$\upsilon = \frac{E}{2G} - 1 \tag{2.4}$$

This produces ν = 0.29, which is quite reasonable for a foamed elastomer such as VHB tape. Note that this method is too sensitive to small variations in *G'* and *E'* to determine Poisson's ratio with much certainty. It is primarily a check on the offset between the *G'* and *E'* master curves.

For the reasons listed above, only compression geometry data gathered at -20°C (-4°F) and higher was used in the selection of the WLF constants.

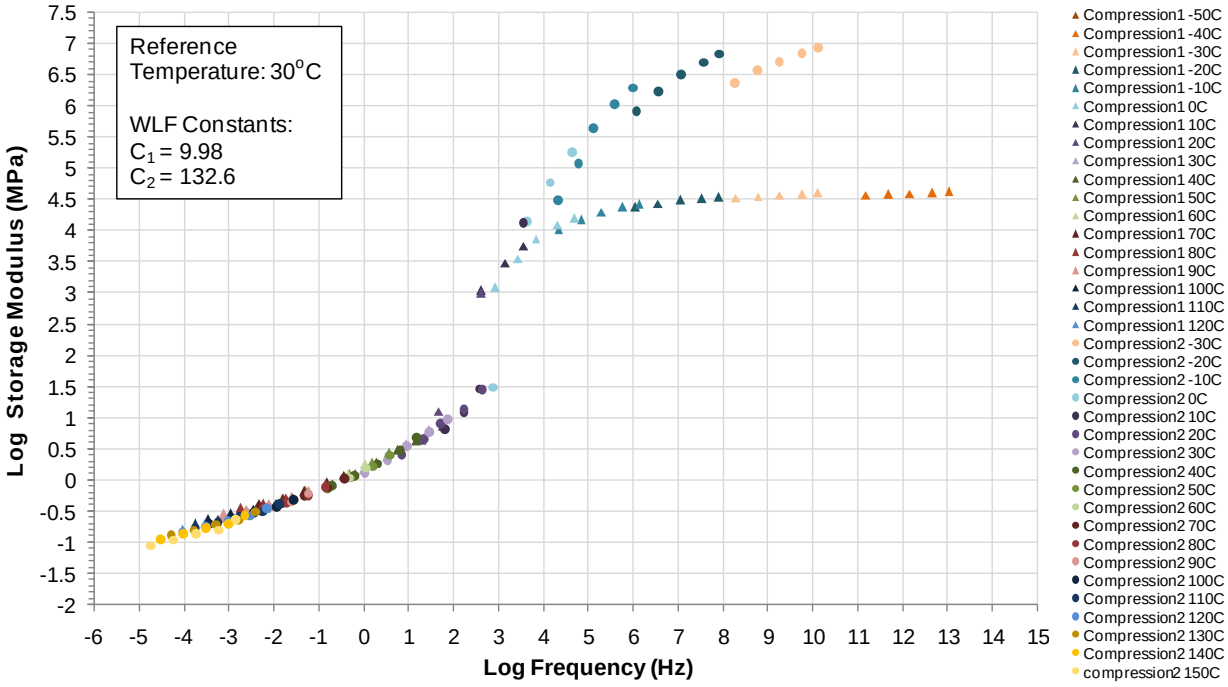

Figure 2.19 Compression geometry G23F storage modulus master curve at 30°C (86°F) reference temperature and using WLF shift factors with C1 = 9.98 and C2 = 132.6.

The long-axis tension geometry produced results with consistency intermediate to the shear and compression geometries. As seen in Fig. 2.20, the plot of log E' versus log frequency for long-axis tension, data from the two replicates diverged when shifted to the high-frequency range. Note that data that is shifted to high frequencies originated from low temperature testing.

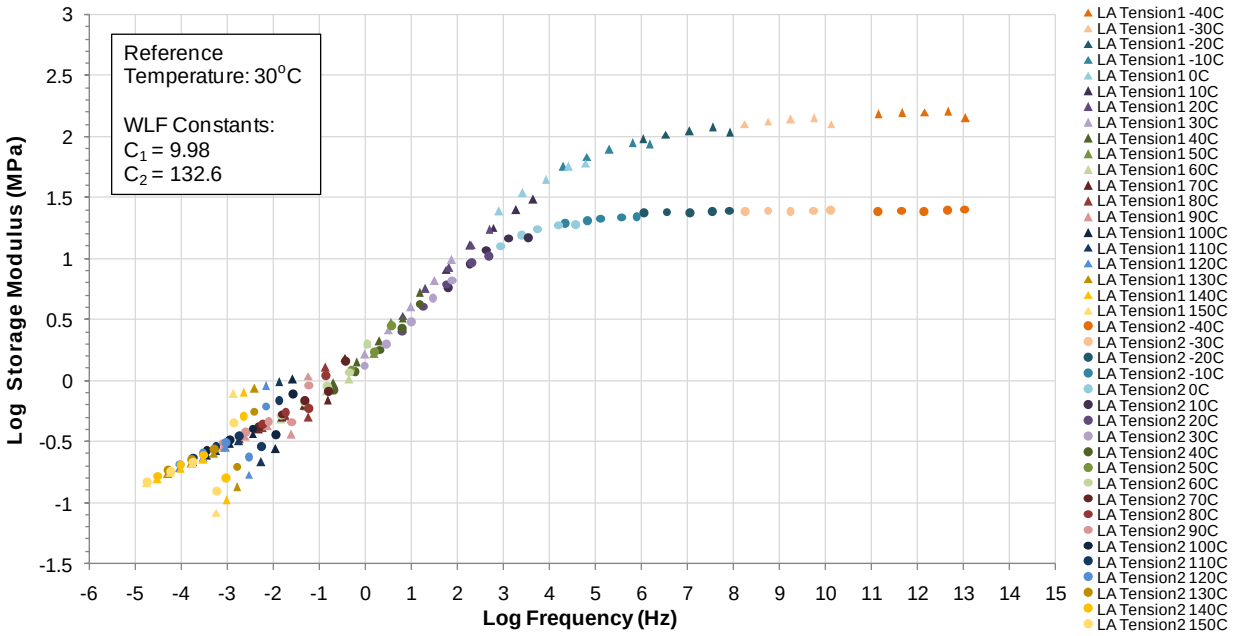

Figure 2.20 Long-axis tension geometry G23F storage modulus master curve at 30°C (86°F) reference temperature and using WLF shift factors with C1 = 9.98 and C2 = 132.6.

One possible reason for this divergence was the cold-to-hot procedure used for the first replicate versus the hot-to-cold procedure used for the second replicate. Another possible cause of the divergence was instrument miscalibration due to the complexity of the steel foil anchors (shown earlier in Fig. 2.3). For example, the anchors transferred load to the adhesive tape in a shear mode. The point where the specimen "begins" and "ends," used to calculate strain, was located at some point along the bond area between the tape and steel foil, and that point could only be estimated. One more possible source of divergence between the two replicates when shifted to the high-frequency range was a possible mechanical problem with the DMA apparatus related to resonance with the steel foil anchors. This interference of the foil anchors was also the probable cause of the two "whiskers" of data that extended above and below the bulk of the data in the low-frequency range. The whiskers that extended above consisted of all the data recorded at 75

Hz, and the whiskers that extended below consisted of all the data recoded at 31.2 Hz. The other three frequencies (1 Hz, 3.2 Hz, and 10 Hz) fell along a similar line. In the low-frequency range ($<10^3$ Hz), the two long-axis tension replicates agreed with each other and with the low-frequency compression geometry data, within a spread of 0.2 decades. This helped to confirm the accuracy of both methods along the low-frequency range of the master curves, and confirmed that the constitutive properties of VHB tape were primarily isotropic. As for the high-frequency range of the long-axis tension master curve, the accuracy of the data was inconclusive.

Beyond determining thermal shift factors, the results of the DMA testing provided values for the glass transition temperature T_g of G23F VHB tapes. The exact value of T_g depends both on the time-scale of the measurement and the constitutive property examined, and so Table 2.3 presents the values using three methods at two representative frequencies. Loss and storage moduli from the shear geometry tests were used to determine these values, because the shear geometry often provided the most consistent and trustworthy results near the apparent glass transition temperature.

There is significant ambiguity as to how and where the glass transition should be defined. As pointed out by Chartoff et al. (1994), there are several distinct definitions even within the ASTM standards. ASTM D 4065 – 06 Standard Practice for Plastics: Dynamic Mechanical Properties: Determination and Report of Procedures states that T_g should be determined from peak loss modulus when plotted against temperature. ASTM D 4092 – 07 Standard Terminology for Plastics: Dynamic Mechanical Properties defines the glass transition temperature as "the approximate midpoint of the temperature range over which the glass transition takes place." However, ASTM E 1640 – 04 Standard Test Method for Assignment of the Glass Transition Temperature By Dynamic Mechanical Analysis defines the glass transition as a temperature near the onset of decrease in storage modulus, which will occur at a lower temperature than the criteria described in ASTM D 4065 – 06 and ASTM 4092 – 07.

Table 2.3 Tg Values Derived from DMA Testing on Shear Specimens

Method	T_g @ Frequency	
	1 Hz	75 Hz
(1) G' [a]	-32°C (-26°F)	-24°C (-11°F)
(2) Peak G"	-12°C (10°F)	4°C (39°F)
(3) Peak tan δ	12°C (54°F)	37°C (99°F)

Notes:

[a] Extrapolated onset of decrease in storage modulus.

The first method employed in this document for determining T_g is the standard method presented in ASTM E 1640 – 04. This method measures the extrapolated onset of the decrease in storage modulus and, according to ASTM E 1640 – 04, tends to provide a lower value of T_g compared to the other two methods employed here. When the storage modulus is plotted as a function of temperature, as was done in Fig. 2.21, the glass transition can be taken as the intersection of a tangent fit to the sub-T_g glassy plateau and a tangent centered at the inflection point of the transition region.

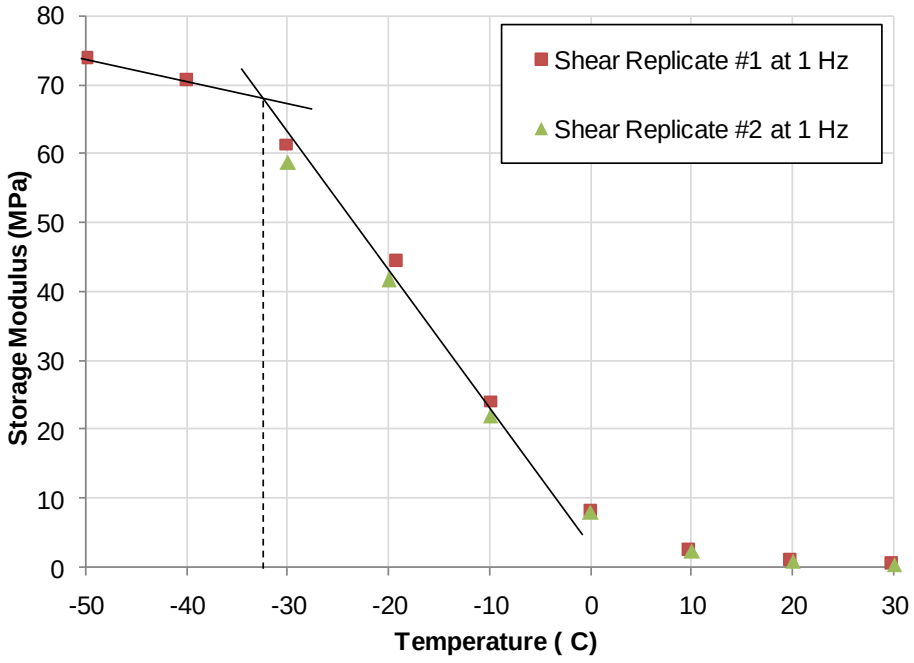

Figure 2.21 Method (1) for determination of Tg at 1 Hz: intersection of tangents to glassy plateau region of storage modulus and transition region of storage modulus.

The second and third methods of determining T_g utilize the temperature at which the values of storage modulus or tangent delta peak at a given frequency (Chartoff et al. 1994). The values presented in Table 2.3 were obtained from the average of the two shear replicates.

Additional test replicates would help refine the DMA data and clarify inconsistencies, but further testing was outside the scope of this project. The collected data fulfilled the primary research goals of determining T_g of G23F VHB tape, determining thermal shift factors for application to creep rupture and ramp-to-fail data, and determining constitutive properties for input into finite element analysis programs. Furthermore, the unreliable ranges of the storage and loss moduli master curves were primarily on the very high-frequency time scale. Inconsistency of high-frequency data does not directly bear on the focus of this project, which was the characterization of response to intermediate and long-term loading.

Creep Rupture

Fig. 2.22 presents creep rupture failure times for G23F VHB tape and the three structural silicone sealants. S1 denotes one-component DC 995 sealant, S2 denotes two-component DC 983 sealant, and S3 denotes one-component DC 795 sealant. Note that arrows on the plot indicate that some or all specimen replicates did not fail within several weeks and were aborted prior to failure.

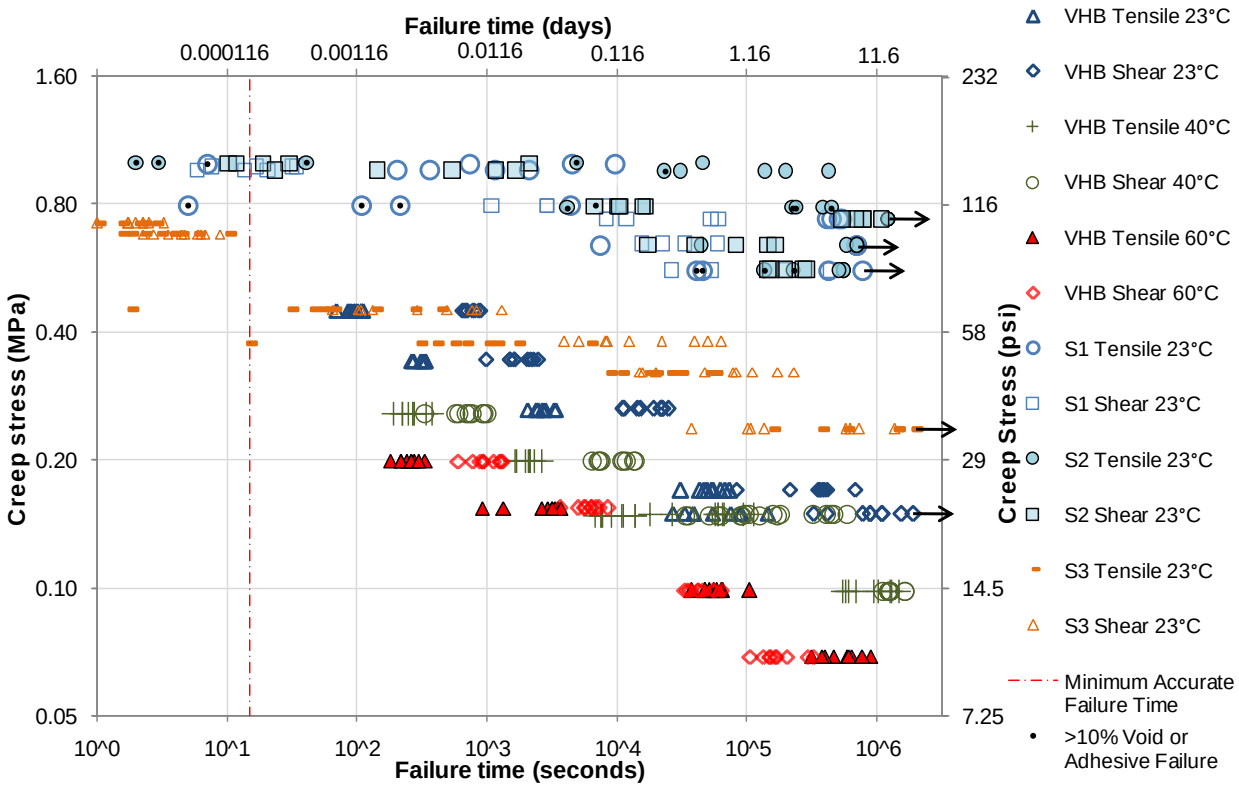

Figure 2.22 Creep rupture data – anodized aluminum adherends bonded with G23F VHB tape and three structural silicone sealants.

The VHB tape specimens exhibited a comparatively tight scatter of failure times, with replicates nearly always failing within the range of one decade of time. Most replicate sets failed within a quarter-decade range. The average coefficient of variation of log time-to-failure for a set of test conditions was 0.033 for tensile VHB tape specimens, and 0.035 for shear specimens. When the data was plotted on log-log scale, it demonstrated a linear relationship between creep stress applied and time to failure. This linear appearance on a log-log plot corresponds to a power relation of the form:

$$\sigma_{creep} = A \cdot t_{fail}^{B} \tag{2.5}$$

If the shift factors derived from DMA testing are applied to the shear and tensile creep rupture data sets gathered at three temperatures, the data aligns into the master curves shown in Fig. 2.23 and Fig. 2.24.

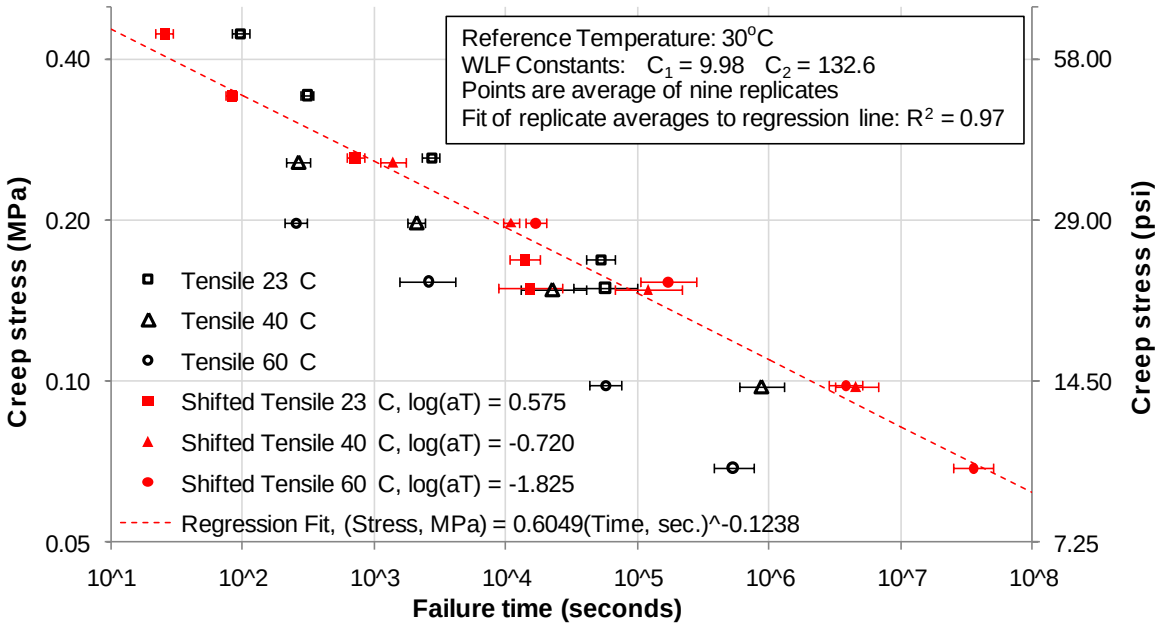

Figure 2.23 Log-log plot of unshifted tensile VHB tape creep rupture data, along with data which has been shifted to 30°C (86°F) reference temperature; each data point is an average of nine replicates, and error bars represent ± one standard deviation.

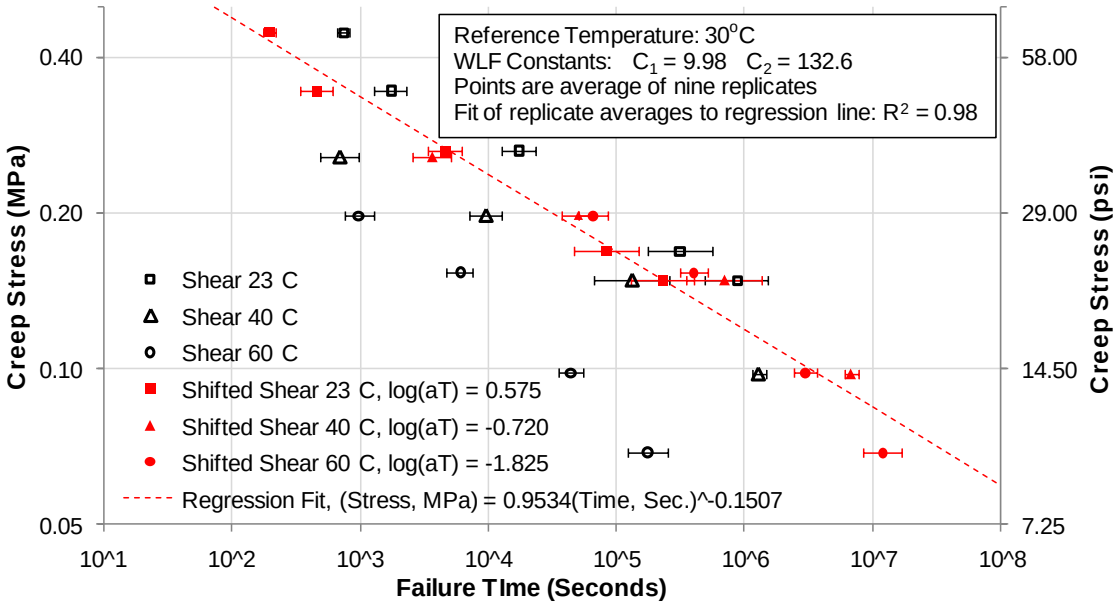

Figure 2.24 Log-log plot of unshifted shear VHB tape creep rupture data, along with data which has been shifted to 30°C (86°F) reference temperature; each data point is an average of nine replicates, and error bars represent ± one standard deviation.

The shifted tensile VHB tape data was fit with a least-squares regression line, which minimized log creep stress error, resulting in Eq. (2.6) with stress in MPa and time in seconds:

$$\sigma_{creep} = 0.6049 \cdot t_{fail}^{-0.1238} \tag{2.6a}$$

and the inverse:

$$t_{fail} = \left(\frac{0.6049}{\sigma_{creep}} \right)^{8.078} \tag{2.6b}$$

Regression fit of Eq. (2.6a) to shifted log (σ_{creep}) experimental data: $R^2 = 0.967$

The shifted shear VHB tape data was similarly fit with Eq. (2.7):

$$\tau_{creep} = 0.9534 \cdot t_{fail}^{-0.1507} \tag{2.7a}$$

and the inverse:

$$t_{fail} = \left(\frac{0.9534}{\tau_{creep}} \right)^{6.636} \tag{2.7b}$$

Regression fit of Eq. (2.7a) to shifted log (τ_{creep}) experimental data: $R^2 = 0.975$

These equations fit to creep rupture data can provide an evaluation of the established dynamic allowable stress of 85 kPa (12 psi) for VHB tape. This evaluation is applicable for G23F VHB tape bonding two anodized aluminum adherends at 30°C (86°F) and roughly 20% relative humidity. The established ASCE 7-05 wind load is a peak gust speed over three seconds, and so the creep rupture data is extrapolated to the high stress, short time to fail range. For tensile loading, Eq. (2.6a) indicates a creep rupture load of 530 kPa (77 psi) will produce an average failure time of three seconds. For shear loading, Eq. (2.7a) indicates a creep rupture load of 810 kPa (118 psi) will produce an average failure time of three seconds. When compared to the allowable dynamic stress of 85 kPa (12 psi), the experimental creep stress producing an average three second time to failure is greater by a factor of 6.2 in tension and 9.5 in shear. This can be compared to the safety factor of 5 that was applied by 3M to determine the established 85 kPa (12 psi) design strength (Kremer 2005). Note that 3M did not base their determination of

dynamic design strength on three seconds, but on “loads lasting seconds or minutes,” so this analysis based on three seconds should be expected to provide higher safety factors.

Another way to compare the creep rupture data gathered by this study with the established dynamic allowable strength is to examine the predicted time to fail of 85 kPa (12 psi) multiplied by the safety factor of 5. At a creep stress of 85 kPa (12 psi) · 5 = 425 kPa (60 psi), tensile specimens will fail in 17 seconds and shear specimens will fail in 213 seconds.

There were several sources of statistical variation in the creep rupture tests. The test frame introduced some error when the load applied by each cylinder varied slightly. When 220 N (50 lb) of load was applied to the indicating cylinder, the test cylinders applied loads ranging from 218 N to 227 N (49 lb to 51 lb). Variation in the specimens also contributed to scatter in the data. 28% (35 out of 126) of the tensile VHB tape specimens exhibited defects in the form of small (~5 mm, 0.2 in.) circular regions where the VHB tape had either a) debonded from the adherend during testing, leaving no residual adhesive, or b) never formed a bond with the adherend during specimen fabrication. The second option appears to be more likely, and could have been caused by bubbles of air trapped between the VHB tape and aluminum adherend during fabrication. There was no obvious correspondence between the voids and creep stress or test temperature. Fig. 2.25 demonstrates these voids with a representative set of failed tensile VHB tape specimens, tested at ambient 23°C (73°F). On average, void-containing specimens failed 0.01 decades sooner (reduction of time to fail to 80%) compared to the average failure time for all replicates of the relevant condition set.

In the photos presented here, the specimens have relaxed back to nearly the original dimensions of the tape before testing. However, during testing both shear and tensile specimens were observed to stretch to as much as 25 mm (1.0 in.) between adherends before failure, resulting in strains of up to 1100%. Fig. 2.26 shows tensile and shear VHB tape specimens at approximately 900% strain.

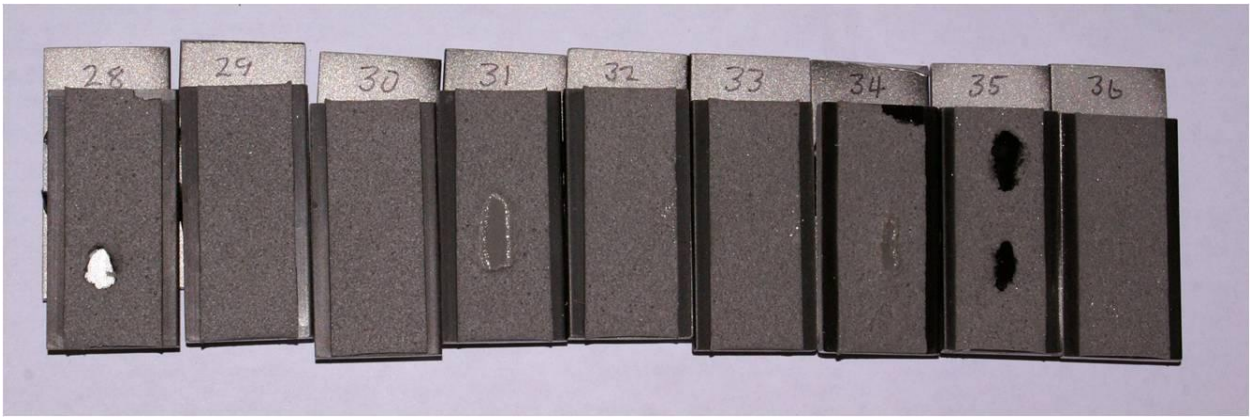

Figure 2.25 Representative failed tensile VHB tape specimens, tested at 23°C (73°F), showing some entrapped air voids.

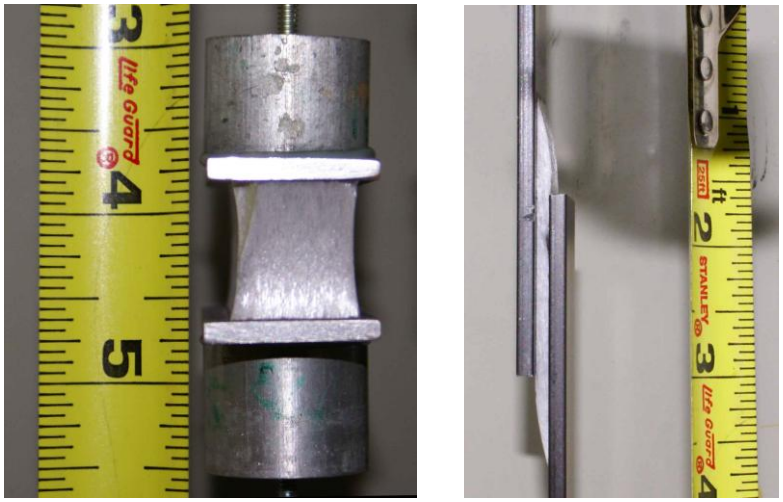

Figure 2.26 VHB tape specimens in a) tension and b) shear at nearly 900% strain.

Fig. 2.27 and Fig. 2.28 show representative examples of failed shear VHB tape specimens. When loaded in shear, the VHB tape failures were reminiscent of classic hackle patterns as described by Chai (1986). The residual wedges of VHB tape were highly elongated, due to the high extension at failure of as much as 25 mm (1.0 in.). The initial cohesive split of the foam core was oriented at roughly 45° to the face of the adherend, but after failure occurred the residual adhesive relaxed back to the elongated wedge seen in Fig. 2.27. Some of the shear specimens also contained voids of entrapped air, but the voids were often obscured after failure and could not be accurately counted to determine the effect on time to failure.

Figure 2.27 Representative failed shear VHB tape specimens, tested at 23°C (73°F), showing wedge-shaped residual adhesive.

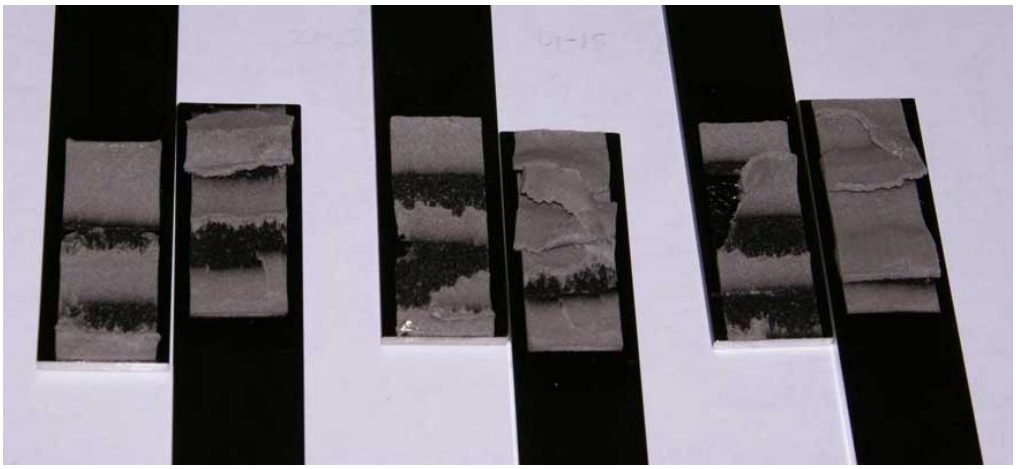

Figure 2.28 Representative failed shear VHB tape specimens, tested at 23°C (73°F).

When the test temperature increased or the applied load decreased, the appearance of the failed VHB tape specimens changed. It cannot be stated for certain whether this change in failure surface appearance was related to the initial failure event, or to events that occurred after failure had initiated and the tape was continuing to pull apart. Using the 72-station creep frame, it was impractical to track the location of failure initiation because the specimens were enclosed in the test frame and not observable during testing. When the specimens were tested for longer duration at lower stresses and elevated temperature, as shown in Fig. 2.29 and Fig. 2.30, the failed

specimens showed a combination of adhesive and cohesive failure surfaces. The lower-temperature, higher-stress, and shorter-duration tests, such as those shown in Figs. 2.25, 2.27, and 2.28, exhibited a more cohesive failure mode. This possible change in the mode of failure must be taken into account when discussing the master curve of creep rupture data generated from tests shifted from elevated temperatures to 30°C (86°F). The important question is whether the shift from a primarily cohesive failure surface to a mixture of adhesive and cohesive failure surfaces would have occurred during very long-term and low-stress testing, which was simulated in this research by elevated temperatures. Is the change in failure mode purely a reaction to high temperature, or is it the result of long-term loading, and the high temperatures simply accelerated the occurrence of this behavior? Furthermore, does the change in failure mode shorten or lengthen the creep rupture time to failure? These questions bear directly on the accuracy of the creep rupture master curve.

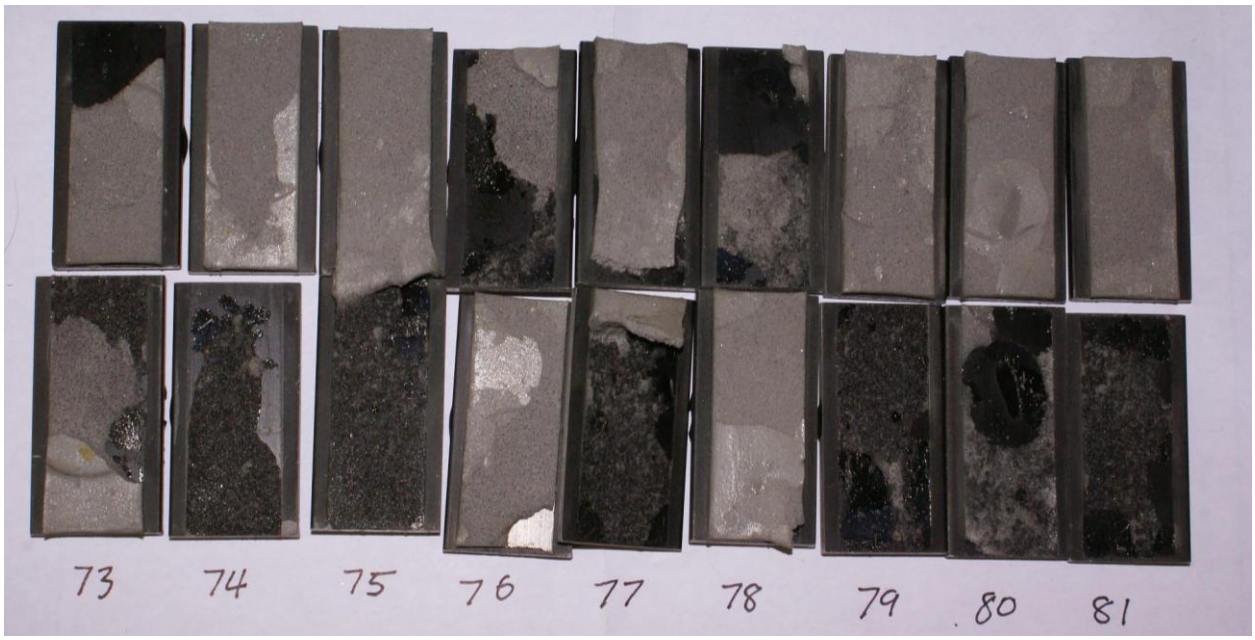

Figure 2.29 Failed tensile VHB tape specimens, tested at 60°C (140°F) and 0.07 MPa (10 psi).

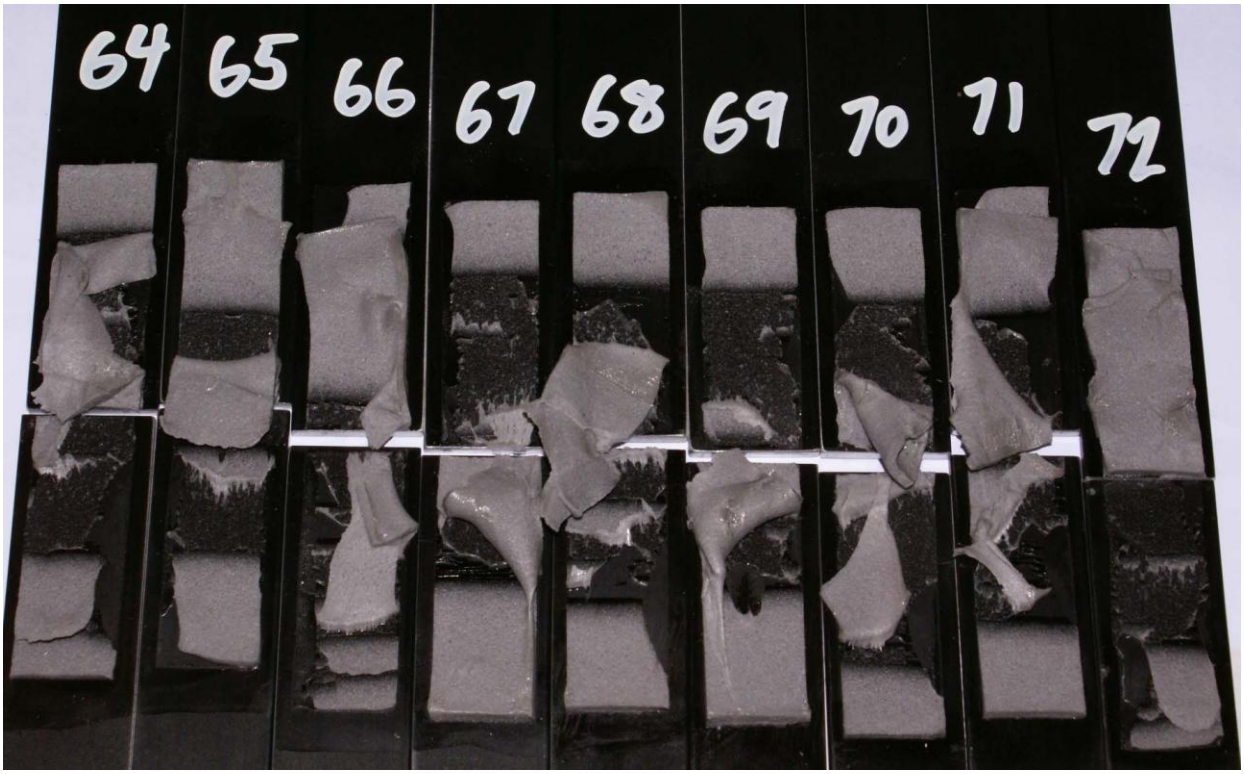

Figure 2.30 Failed shear VHB tape specimens, tested at 60°C (140°F) and 0.15 MPa (22 psi).

In order to investigate the relation between failure time, creep stress, test temperature, and adhesive failure surfaces, tensile VHB tape specimens with greater than 10% and greater than 95% adhesive failure surface were counted, and plotted against creep stress in Fig. 2.31 and against log time to failure in Fig. 2.32. This survey of adhesive failure was not performed for shear VHB tape specimens, because the differences in failure surface were more subtle and difficult to quantify.

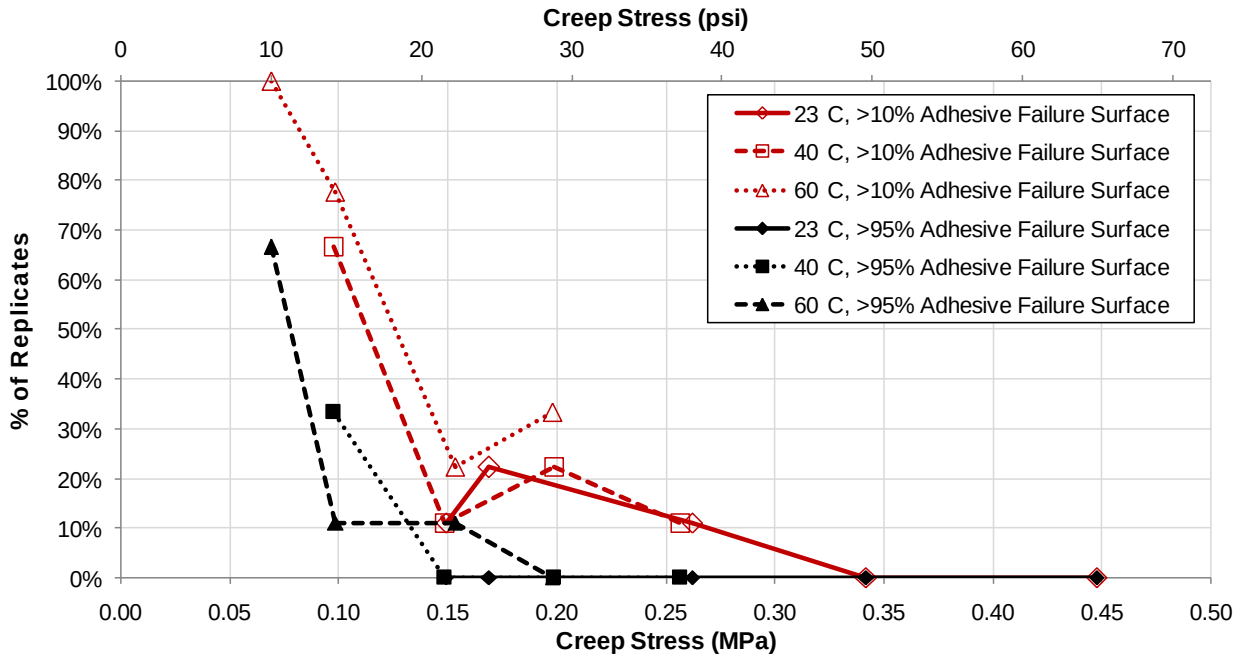

Figure 2.31 Occurrence of adhesive failure surface in relation to creep stress and temperature.

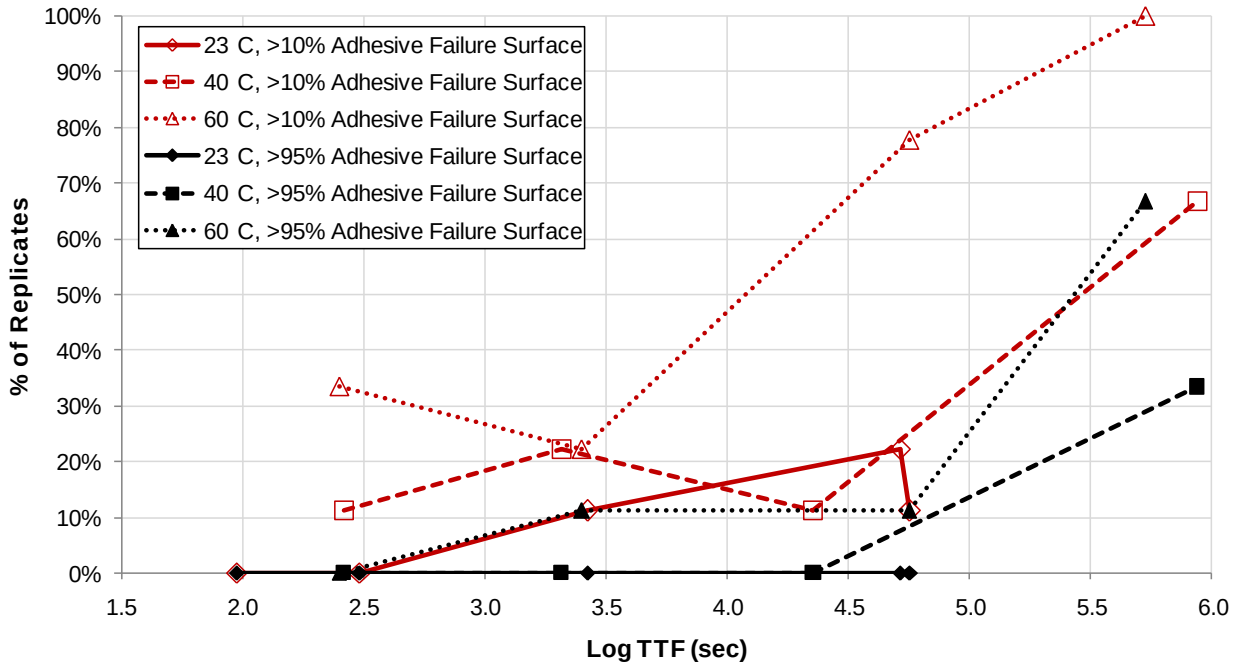

Figure 2.32 Occurrence of adhesive failure surface in relation to log time to fail and temperature.

Within each temperature set on both of the proceeding figures, decreasing creep stress or increasing time to failure corresponded to an increase in the adhesive failure surface.

Furthermore, for the plots of creep stress versus adhesive failure in Fig. 2.31, the three temperature sets aligned into a consistent curve. This alignment suggested that creep stress is dominant over temperature as a determining factor for the occurrence of adhesive failure surfaces. The plots of time to failure versus adhesive failure did not align into a smooth curve, until 30°C (86°F) reference thermal shift factors were applied, as shown in Fig. 2.33.

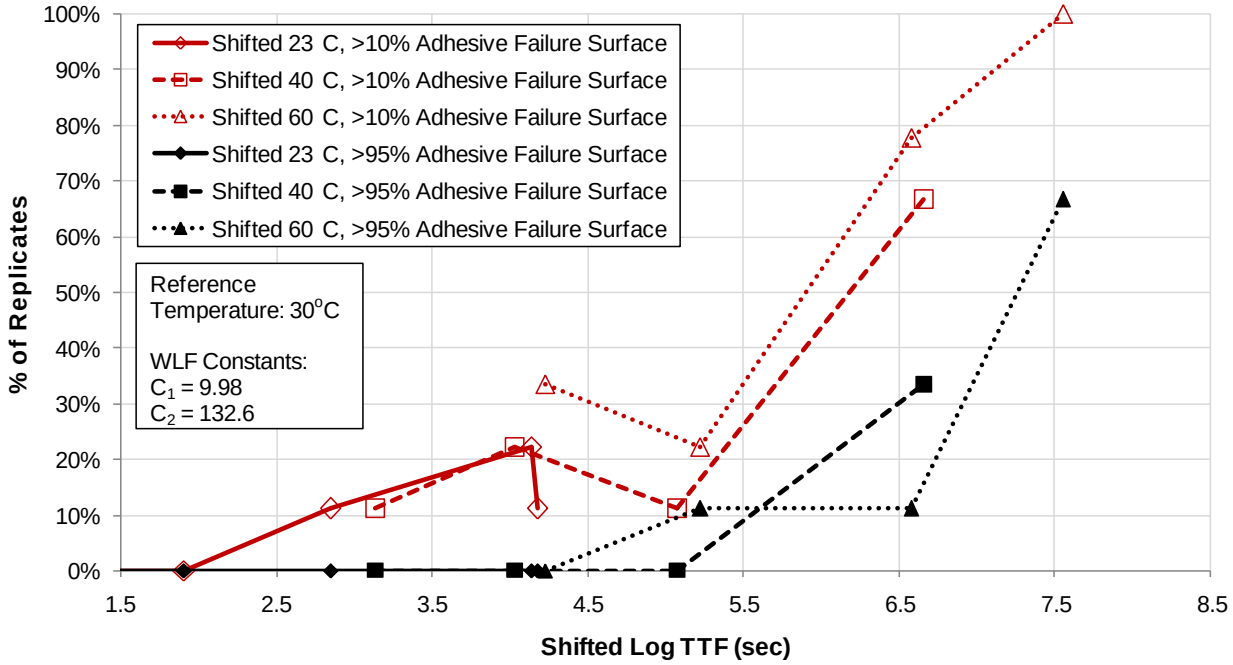

Figure 2.33 Occurrence of adhesive failure surface in relation to log time to fail shifted to 30°C (86°F) reference temperature.

The offset seen in Fig. 2.32 demonstrated that temperature did influence the occurrence of the adhesive failure surface; however, the fact that the thermally-shifted data in Fig. 2.33 aligned into a smooth curve suggested that time temperature superposition could be applied to the appearance of failure surfaces. The data suggested that temperature increased adhesive failures because high temperatures simulated long loading durations. This was significant because if temperature had influenced the mode of failure in a manner entirely independent from TTSP, then thermal shift factors would be less accurate as a prediction of long-term creep rupture behavior.

The silicone specimens exhibited higher scatter of time to failure, in comparison to the VHB tape specimens. Fig. 2.34 presents the log time to failure coefficient of variation for each specimen type.

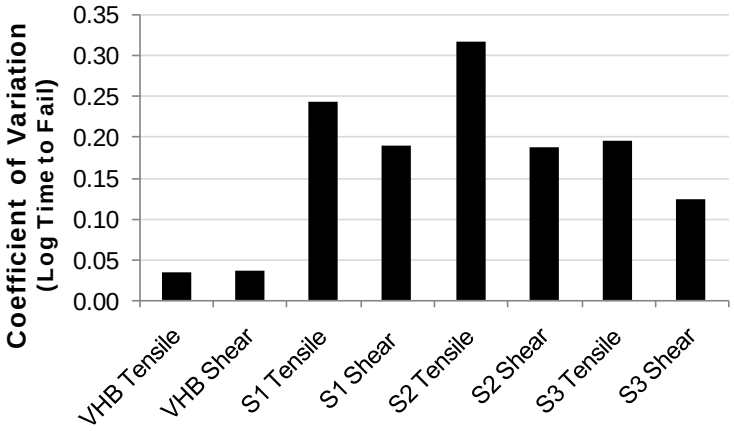

Figure 2.34 Creep rupture coefficient of variation by specimen type.

The scatter seen in the S1 silicone specimens can in part be attributed to the widespread presence of and sensitivity to interior voids and defects that became visible after the specimens failed. Fig. 2.35 and Fig. 2.36 demonstrate a representative set of tensile and shear S1 specimens.

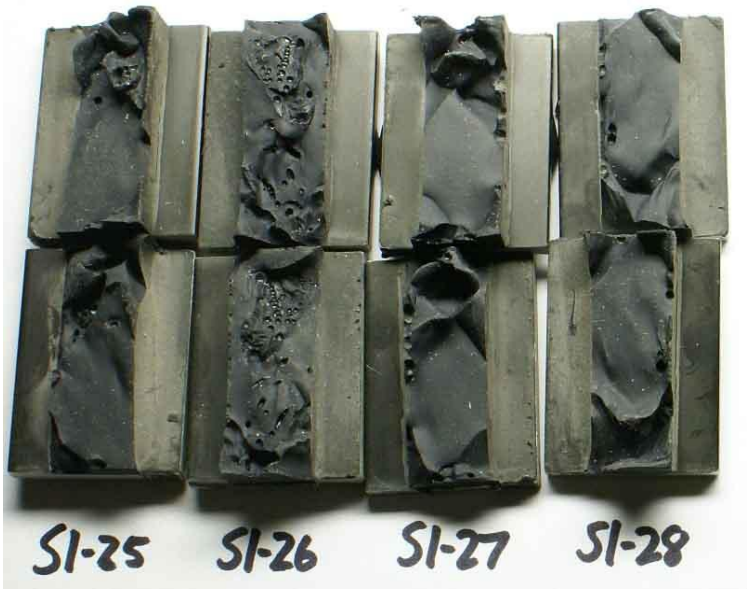

Figure 2.35 Failed S1 tensile creep rupture specimens.

Figure 2.36 Failed S1 shear creep rupture specimens.

The correlation between visible defects and time to failure was especially strong for the tensile S1 silicone specimens. Nearly all the S1 shear and tensile specimens had voids occupying 10% or less of the failure surface area; however, 17% (4 out of 24) of the S1 tensile specimens had failure surfaces with more than 10% voids by area. These specimens failed 1.2 decades sooner (reduction of time to fail to 6%) compared to the average failure time for all replicates of the relevant condition set. The shear S1 silicone specimens also demonstrated a high degree of scatter, but none of those specimens exhibited failure surfaces with more than 10% voids.

S2 silicone specimens exhibited few voids. The scatter seen in the S2 silicone specimens can instead be attributed to partial adhesive failures along the face of the anodized aluminum adherends. Fig. 2.37 and Fig. 2.38 show a representative set of tensile and shear S1 specimens. Note that the tensile S2-5 and S2-6 specimens exhibit partially adhesive failure surfaces.

Figure 2.37 Failed S2 tensile creep rupture specimens.

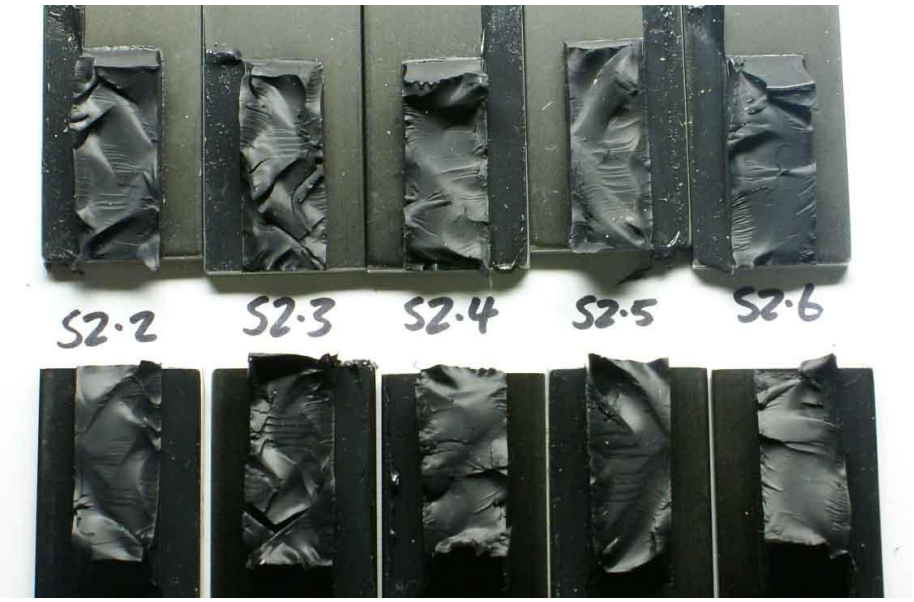

Figure 2.38 Failed S2 shear creep rupture specimens.

Of the tensile S2 silicone specimens, 37% (11 out of 30) had failure surfaces that exhibited more than 10% adhesive failure by visual inspection (the remaining area was cohesive). These specimens failed 0.41 decades sooner (reduction of time to fail to 39%) compared to the average failure time for all replicates of the relevant condition set. Of the shear S2 silicone specimens,

7% (2 out of 30) had a failure surface that was more than 10% adhesive. These specimens failed 0.42 decades sooner (reduction of time to fail to 38%) compared to the average failure time for all replicates of the relevant condition set.

The S3 specimens demonstrate a distinct pattern of voids, along with a combination of cohesive and adhesive failure surfaces. Roughly 80% of the S3 specimens contained thin, crack-like voids, which were often visible before testing. These voids may have been the result of contraction of the silicone during curing. Fig. 2.39 and Fig. 2.40 present a representative set of tensile and shear S3 specimens. It was not productive to attempt to describe the effect of voids or failure surface appearance for the S3 specimens, because nearly all the specimens exhibited a uniform mix of thin voids, adhesive failure at the adherend, and cohesive failure through the body of the sealant.

The common defects of tested VHB tape and silicone sealant specimens and the effect on creep rupture failure time are summarized in Table 2.4.

Figure 2.39 Failed S3 tensile creep rupture specimens.

Figure 2.40 Failed S3 shear creep rupture specimens.

Table 2.4 Summary of the Common Defects and Associated Effect on Time to Failure

Material	Geometry	Common defect	Criteria	Fraction with defect	Effect on TTF (compared to condition set average)	
					reduction of log (TTF)	to % of average (lasts X% as long)
VHB	Tensile	~5 mm air bubble voids	1 or more	35/126 (28%)	0.099	80%
	Shear	~5 mm air bubble voids	-	Difficult to spot	-	-
S1	Tensile	Bubble-shaped voids	> 10% of failure surface	4/24 (17%)	1.20	6%
	Shear	Bubble-shaped voids	> 10% of failure surface	0%	-	-
S2	Tensile	Adhesive failure at adherend	> 10% of failure surface	11/30 (37%)	0.41	39%
	Shear	Adhesive failure at adherend	> 10% of failure surface	2/30 (7%)	0.42	38%
S3	Tensile	Adhesive failure at adherend, and long thin voids	-	Nearly all specimens	-	-
	Shear	Adhesive failure at adherend, and long thin voids	-	Nearly all specimens	-	-

A question raised by the prevalence of voids in the structural silicone sealants is whether the degree of voids encountered is representative of a typical field installation. No tested S1 or S2 silicone specimen had voids visible on the exterior before failure, although crack-like voids were visible on the surfaces of the S3 specimens. The S1 and S3 specimens were prepared by 3M personnel following the procedure described in the experimental section. The S2 specimens were prepared by an experienced window-glazing applicator. No matter the source, some specimens of each type of structural silicone contained voids. However, more voids were found in the S1 and S3 specimens.

Ramp-to-Fail

Fig. 2.41 and Fig. 2.42 present the tensile and shear ultimate strengths of the silicone and VHB tape specimens, plotted on a log-log scale. As the rate of strain increased, the ultimate strength of the VHB tape increased. The silicone specimens also increased ultimate strength as strain rate increased, but to a lesser extent. The S2 tensile specimens (two-component DC 983 sealant) were least affected by rate of strain. The S3 shear and tensile specimens (one-component DC 795

sealant) demonstrated ultimate strength that was nearly equivalent to the G23F VHB tape specimens, with the S3 specimens providing slightly more resistance at 5 mm/min (0.197 in./min) and the VHB tape specimens providing slightly more resistance at 500 mm/min (19.7 in./min). See Appendix H for tabulated data.

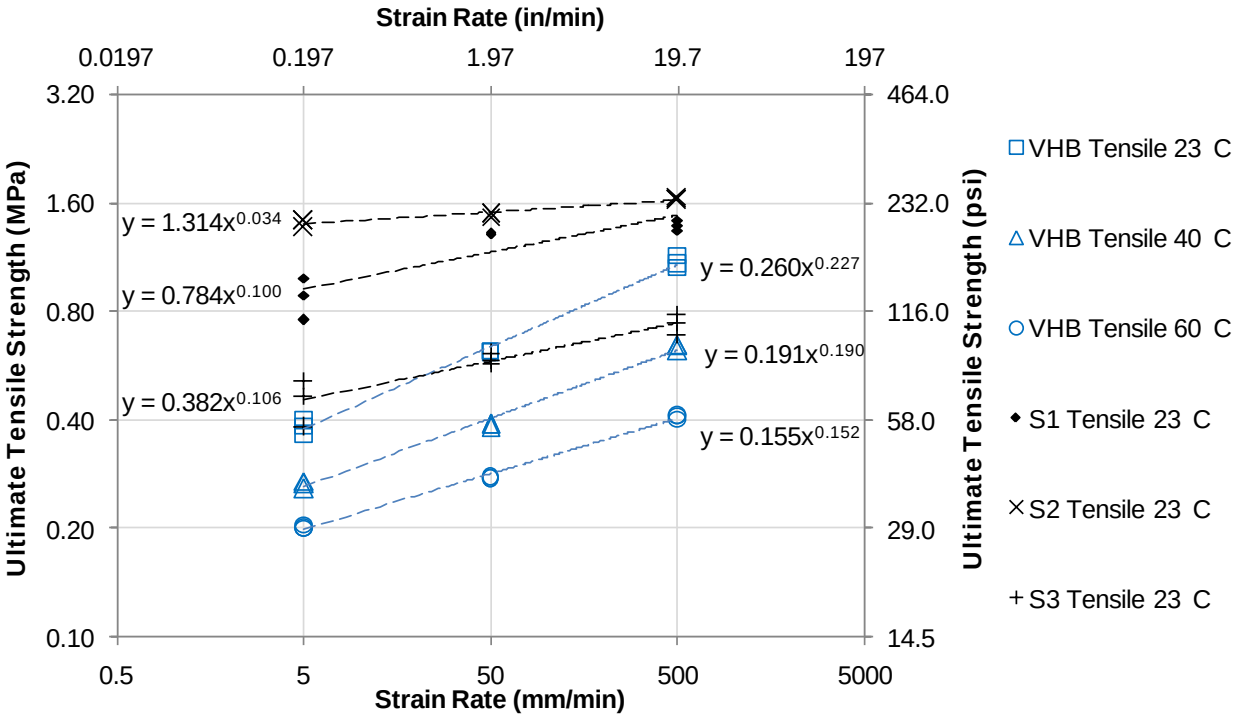

Figure 2.41 Peak tensile stress resistance of specimens subject to several ramp-to-fail strain rates.

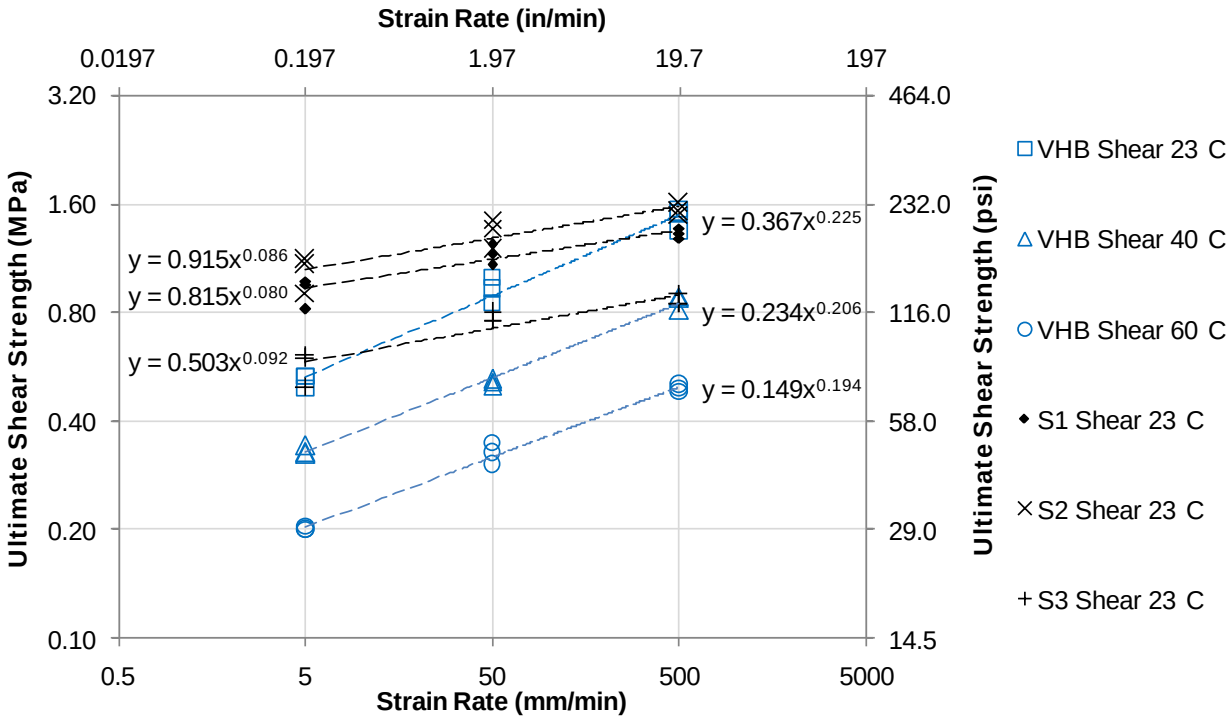

Figure 2.42 Peak shear stress resistance of specimens subject to several ramp-to-fail strain rates.

In this discussion, the initial failure mode is defined as the event that immediately leads to a sudden drop in strength. The failure mode event did not always coincide with the point of ultimate strength. As can be seen in Fig. 2.47 through Fig. 2.52, after ultimate strength was achieved, some specimens continued to provide a lesser degree of load resistance until complete failure occurred. This failure mode could only be determined by observing the specimens during testing; after failure occurred, it was difficult to distinguish which element of the failure surface represented the initial failure mode.

The initial mode of failure for the tensile VHB tape specimens at all temperatures and strain rates was a cohesive split in the acrylic foam core. For the shear VHB tape specimens, all initial failures were cohesive in the foam core except for some of the specimens tested at 60°C (140°F). Two of the three shear replicates tested at 60°C (140°F) and 500 mm/min (19.7 in./min) failed by a combination of cohesive splitting of the acrylic foam core and cohesive splitting of the acrylic adhesive which bonds the foam core to the anodized aluminum adherend. This failure mode left a hackle pattern, shown in Fig. 2.43. One shear replicate tested at 60°C (140°F) and 50 mm/min

(1.97 in./min) failed by a combination of the hackle pattern and an adhesive failure mode which left no visible residue on the adherend.

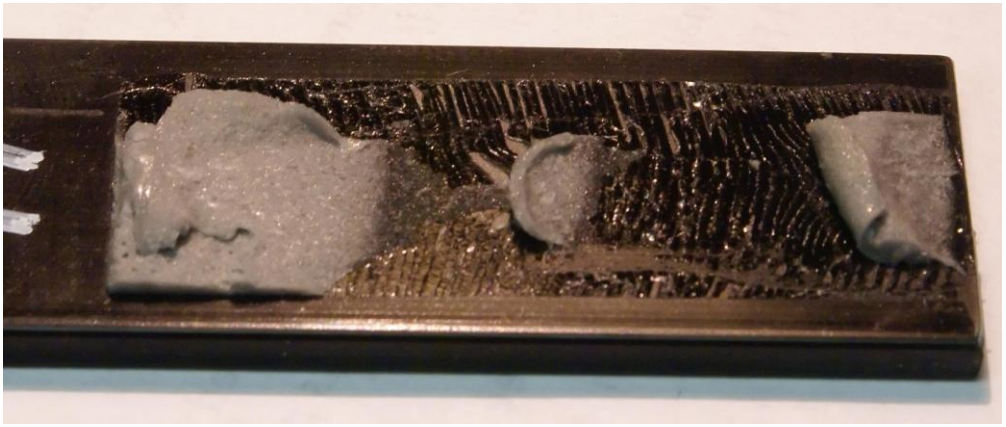

Figure 2.43 Hackle pattern on shear VHB tape specimen tested at 60°C (140°F) and 500 mm/min (19.7 in./min).

Most of the final failure surface patterns were generated after the initial failure, and the appearance of the failed VHB tape specimens was often a combination of cohesive foam core, cohesive hackle, and adhesive failure modes. Final failure surface appearance did not clearly correlate to rate of loading or temperature.

Three out of a total of 27 tensile VHB tape replicates had small 5 mm (0.2 in.) diameter voids, probably resulting from pre-existing air bubbles trapped between the VHB tape and adherend. These three specimens exhibited an average reduction of peak stress of 5% compared to the other replicates. Some of the shear specimens also contained these pre-existing air voids, but the residual VHB tape on the failed shear specimens was distorted to a greater degree than the tensile specimens, making it impossible to spot the voids.

The initial mode of failure for the silicone specimens was primarily a cohesive split within the body of the silicone. However, some adhesive failures did occur. Roughly one out of six of all silicone specimens tested at 5 mm/min (0.197 in./min) exhibited adhesive initial failures. The S3 silicone (one-component DC 795 sealant) often exhibited a rougher failure surface, and it was not always clear where the initial failure took place.

Nearly all of the S1 silicone specimens had small bubble voids consisting of roughly 5% of the area of the failure surface. Fig. 2.44 demonstrates a representative example. One out of six of the S2 silicone specimens had a similar pattern of voids. Nearly all of the S3 silicone specimens appeared to have many thin, crack-like voids. Fig. 2.45 demonstrates the appearance of the failure surface. These thin voids are visible in the S3 specimens before testing, as seen with the untested specimens in Fig. 2.46.

Figure 2.44 S1 tensile specimen with bubble voids highlighted.

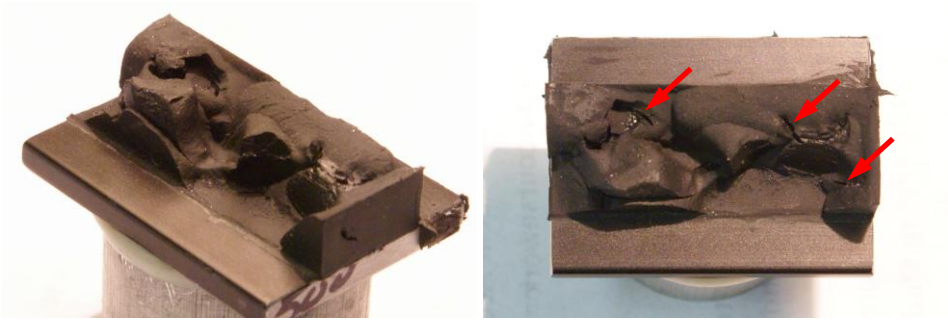

Figure 2.45 S3 tensile specimen with thin, crack-like voids highlighted.

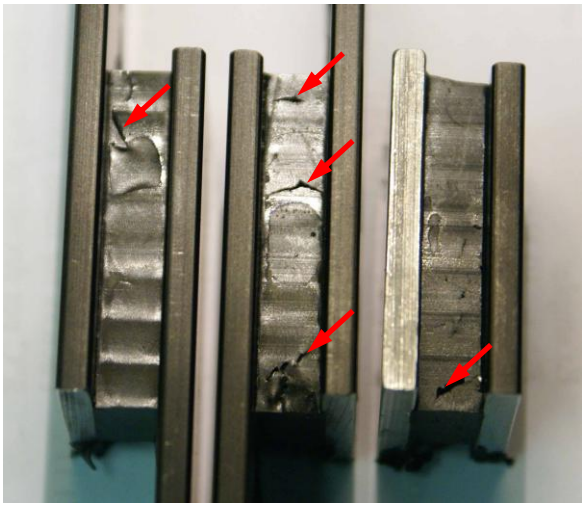

Figure 2.46 Untested S3 specimens with thin, crack-like voids highlighted.

Fig. 2.47 through Fig. 2.52 present plots of test frame crosshead extension versus resisting stress. These plots show only one representative replicate out of the three that were performed for each set of conditions. The VHB tape specimens were 2.3 mm (0.090 in.) thick and the silicone sealant specimens were 12.7 mm (0.50 in.) thick, so the strains experienced before failure were relatively higher for VHB tape specimens than for silicone sealant specimens at a given crosshead extension. For example, at 15 mm (0.59 in.) of extension the VHB tape would be at 650% strain and the silicone sealants would be at 118% strain.

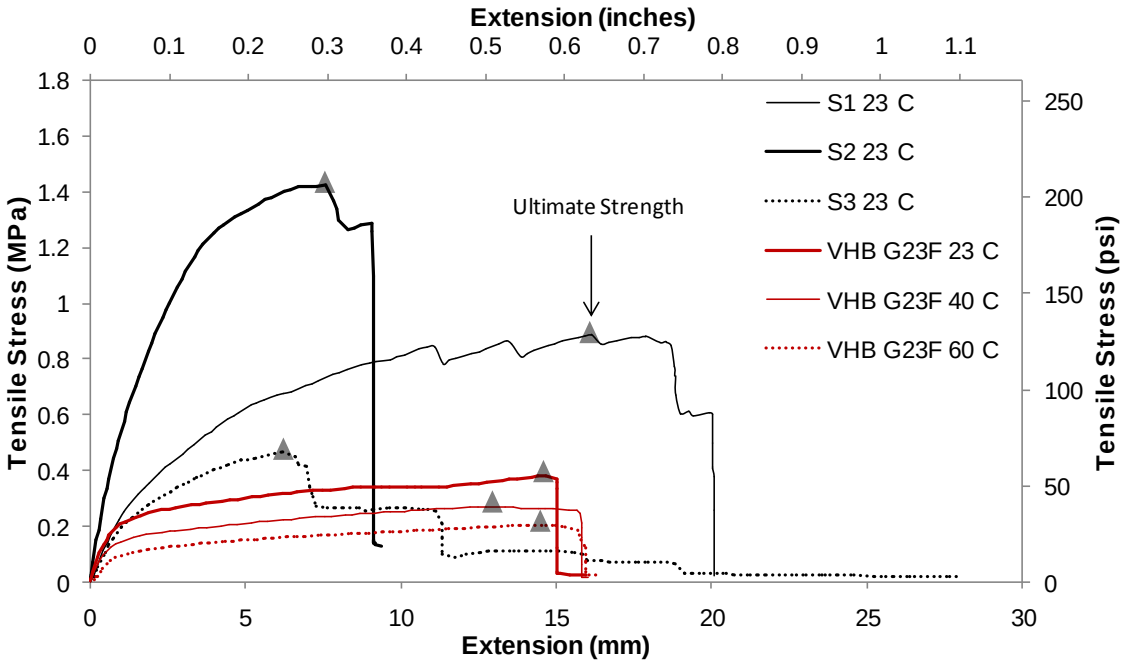

Figure 2.47 5 mm/min (0.197 in./min) tensile ramp-to-fail plots; one representative replicate shown for each condition set.

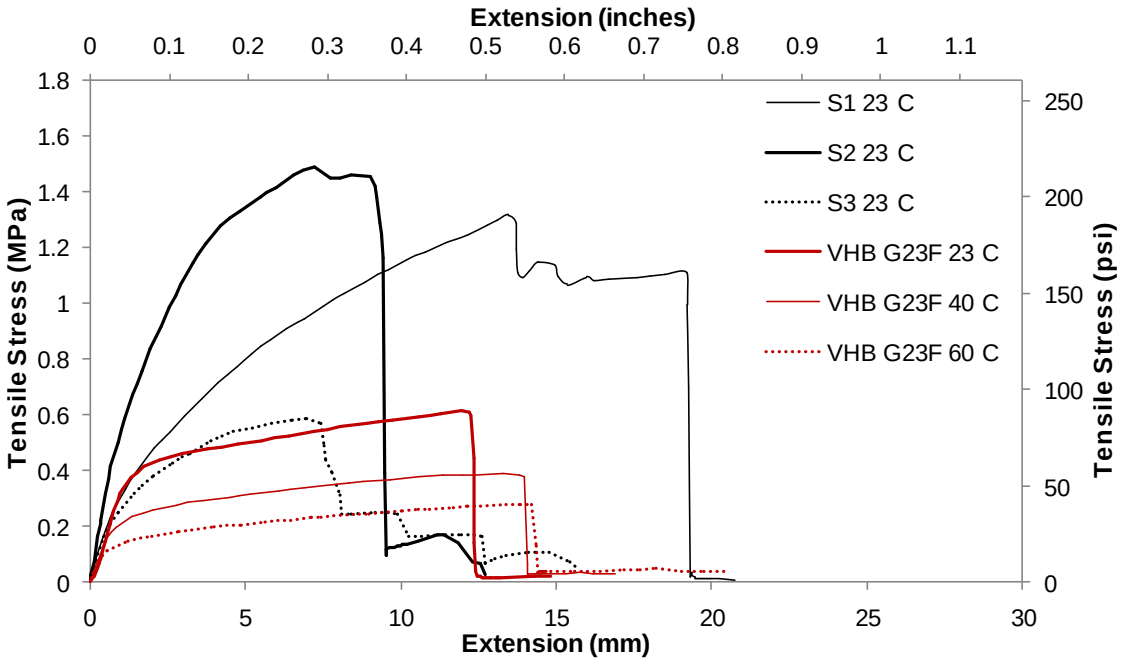

Figure 2.48 50 mm/min (1.97 in./min) tensile ramp-to-fail plots; one representative replicate shown for each condition set.

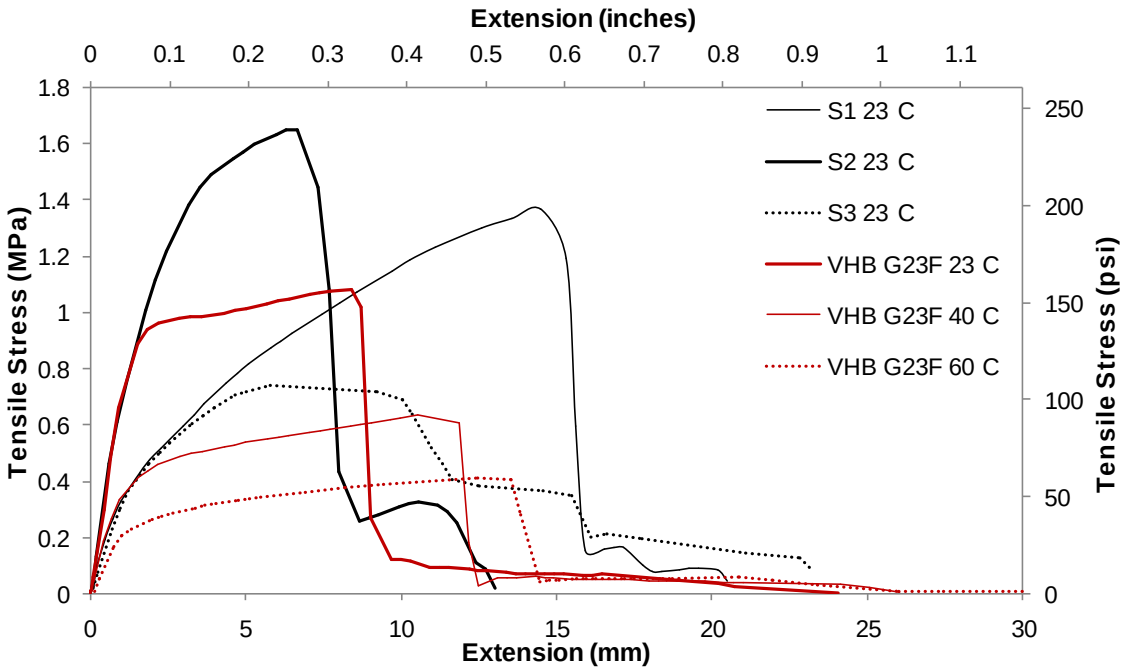

Figure 2.49 500 mm/min (19.7 in./min) tensile ramp-to-fail plots; one representative replicate shown for each condition set.

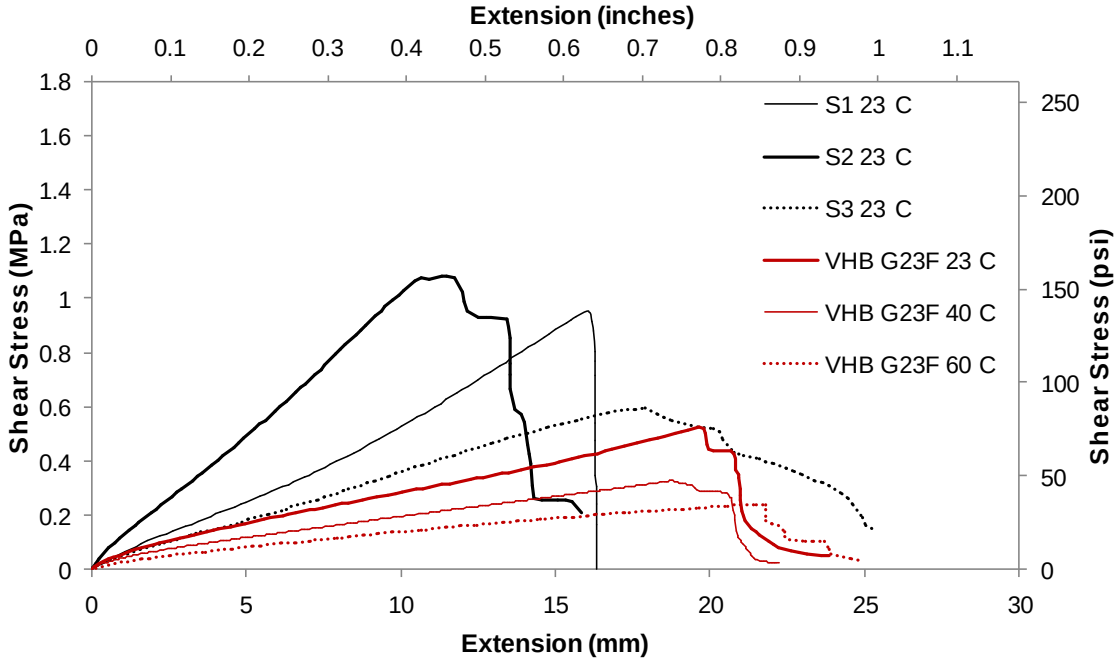

Figure 2.50 5 mm/min (0.197 in./min) shear ramp-to-fail plots; one representative replicate shown for each condition set.

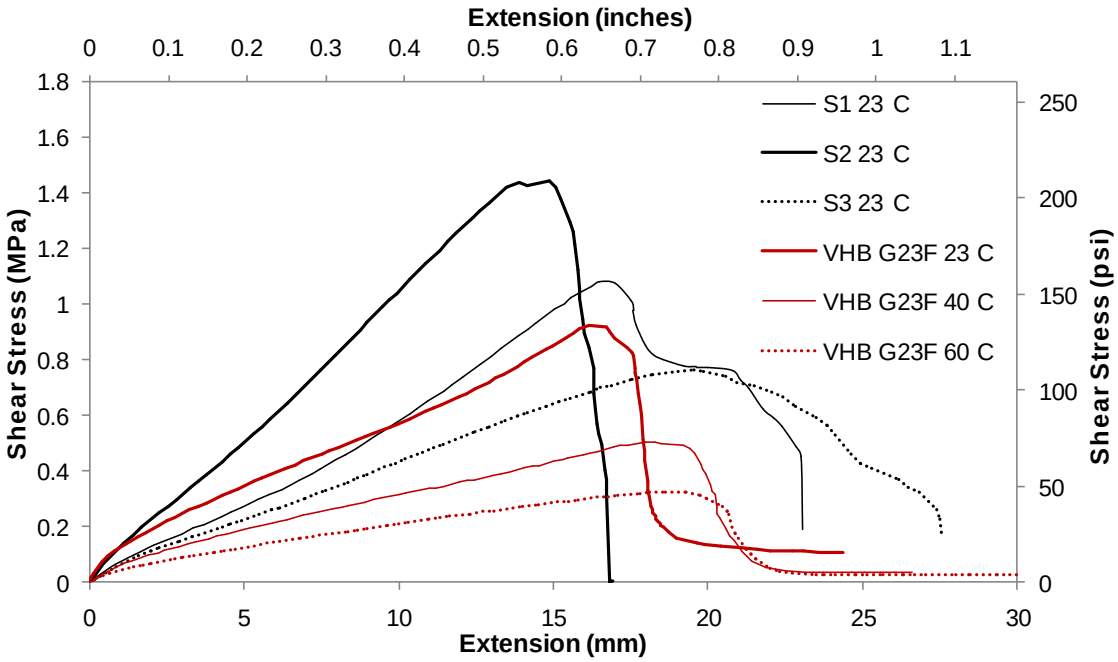

Figure 2.51 50 mm/min (1.97 in./min) shear ramp-to-fail plots; one representative replicate shown for each condition set.

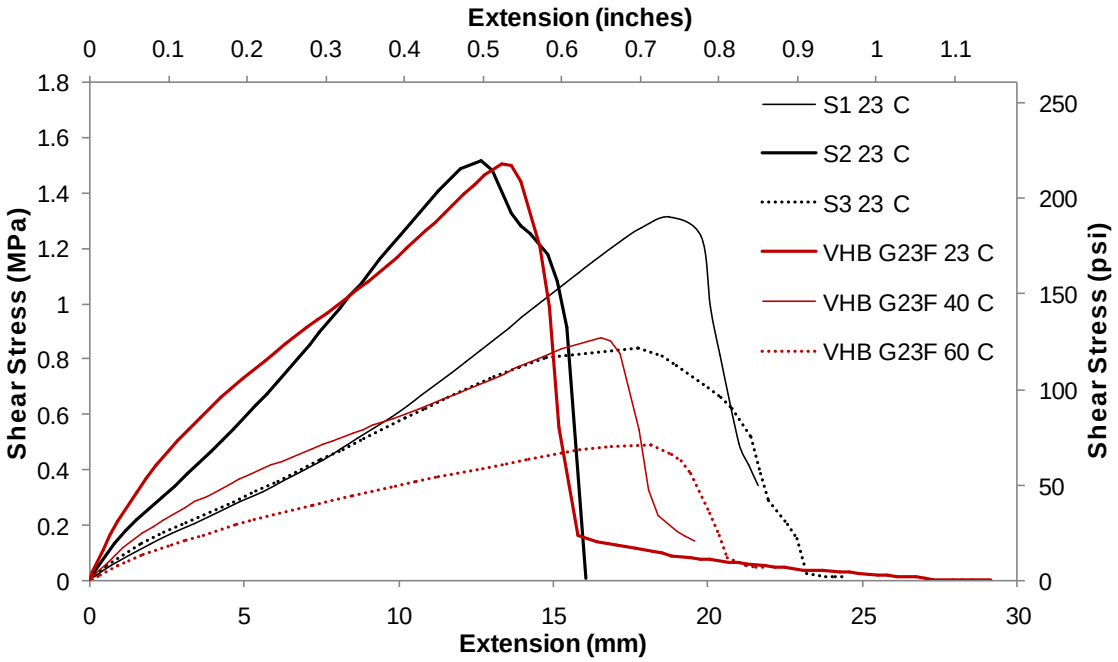

Figure 2.52 500 mm/min (19.7 in./min) shear ramp-to-fail plots; one representative replicate shown for each condition set.

For tensile and shear VHB tape specimens, elevated temperature had the effect of consistently lowering the strength over the entire range of extension, while also allowing the specimens to reach greater strain before failure. Changing the rate of strain had a similar effect, with lower rates of strain resulting in consistently lower strength and higher strain before failure. The silicone specimens did not show a relation between rate of strain and final extension before failure, although they did show a relation between rate of loading and peak strength.

The TTSP thermal shift factors generated from DMA testing were applied to VHB tape ramp-to-fail data, in a similar manner to the shifting done for the creep rupture data. The resulting 30°C (86°F) reference temperature master curves for tensile and shear specimens are shown in Fig. 2.53 and Fig. 2.54. Note that the actual shift factors used are slightly different from those used for the creep rupture master curves. The creep rupture shift factors were based on actual average test temperatures, which were very close but not exactly equal to the nominal 23°C, 40°C, and 60°C (73°F, 104°F, and 140°F). However, for the short-duration ramp-to-fail tests, the temperature could be rigorously controlled and so the nominal temperature values were used to generate shift factors.

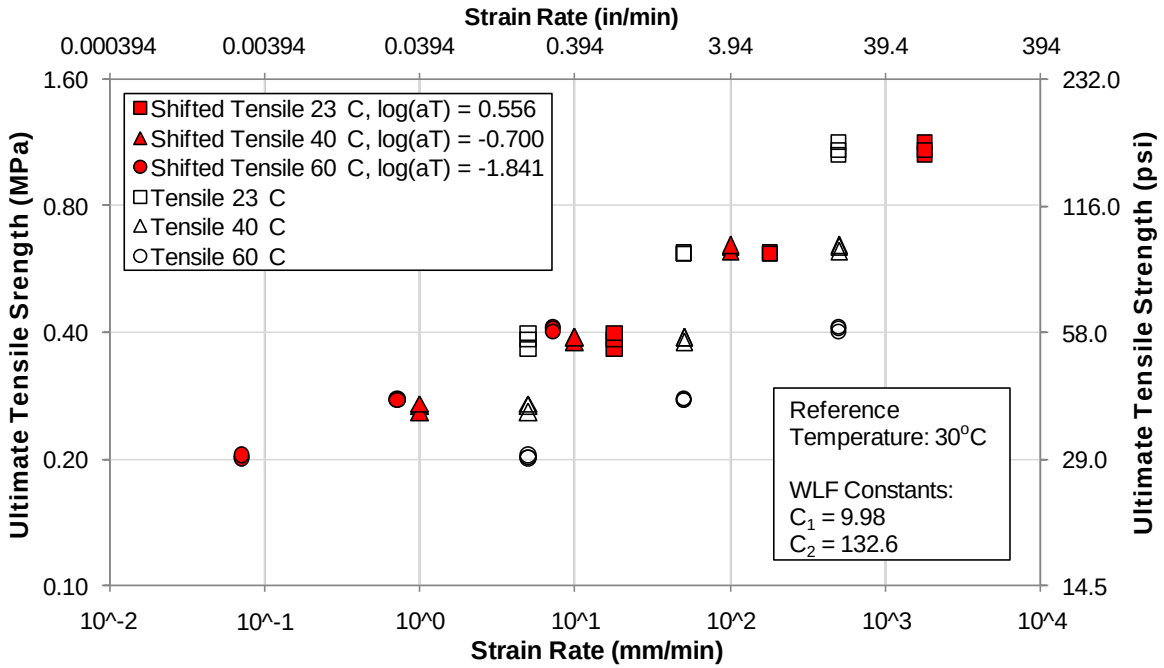

Figure 2.53 Tensile VHB tape master curve of shifted ramp-to-fail data; 30°C (86°F) reference temperature.

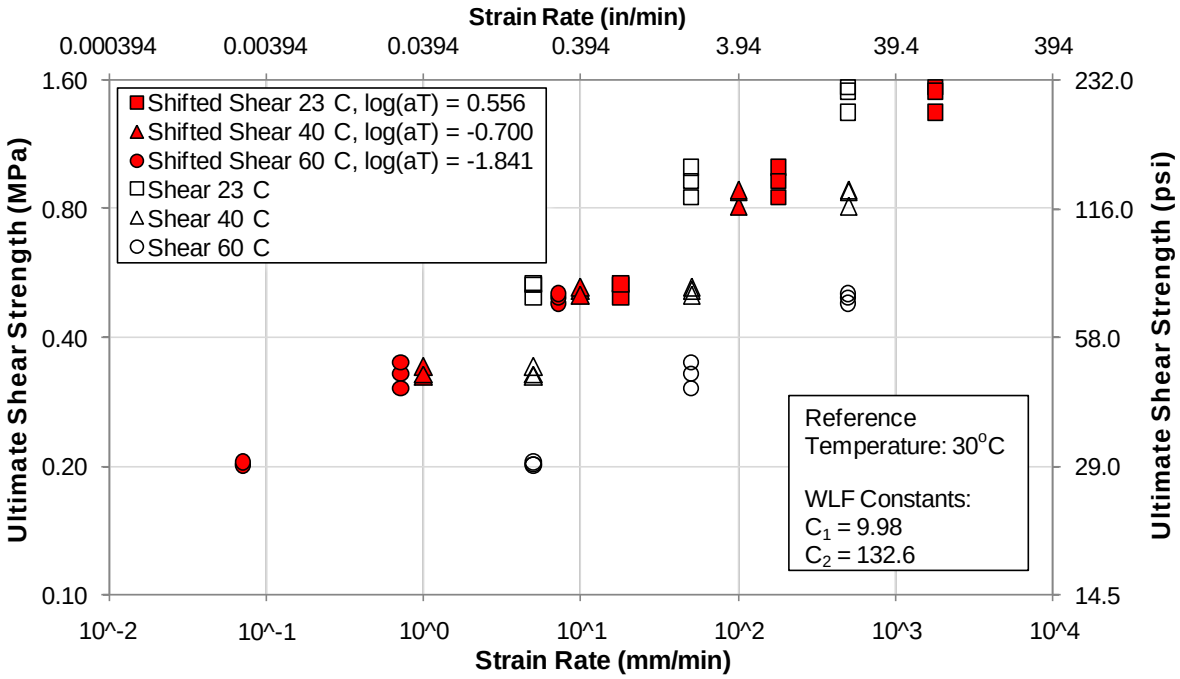

Figure 2.54 Shear VHB tape master curve of shifted ramp-to-fail data; 30°C (86°F) reference temperature.

The application of DMA-generated TTSP shift factors appeared to be less successful for the tensile ramp-to-fail data than it was for the shear ramp-to-fail data or creep rupture data. For the tensile ramp-to-fail master curve, the data collected at distinct temperatures retained an offset from one another of approximately 0.2 decades. Nevertheless, using thermal shift factors generated from DMA tests of constitutive properties, relatively consistent master curves were produced, confirming the general applicability of TTSP and a viscoelastic framework to convey the time and temperature dependence.

CONCLUSIONS

This project has generated a range of information regarding the characterization of 3M's G23F VHB structural glazing tape, while focusing on the relation between load, time, and temperature. The majority of the research effort was directed at generating a large and statistically significant body of tensile and shear creep rupture data. With the aid of a 72-station pneumatic creep frame, 270 VHB tape creep rupture specimens were tested at three temperatures. Three kinds of structural silicone sealants totaling 252 specimens were tested at ambient temperature for the purpose of comparison. In addition to creep rupture testing, shear and tensile ramp-to-fail testing was performed on 54 VHB tape specimens at three rates of strain and three temperatures. The three varieties of silicones, totaling 54 specimens, were tested at three rates of strain and ambient temperature.

Parallel testing of VHB tape and structural silicone sealants highlighted the distinct strengths of the two structural glazing materials. For VHB tape, the creep rupture time to failure was more sensitive to applied creep rupture stress, and the ultimate strength during ramp-to-fail tests was more sensitive to applied rate of strain. The one-component DC 995 sealant (S1) and two-component DC 983 sealant (S2) generally lasted longer than VHB tape under the applied creep rupture stresses, and provided higher ultimate strength at most ramp-to-fail strain rates. In practice, this means VHB tapes require a larger width of bond than S1 or S2 structural silicone sealants for a given design load. The one-component DC 795 sealant (S3) performed slightly better than VHB tape for creep rupture time to failure, and provided equivalent performance under ramp-to-fail loading. However, as the creep stress and rates of strain increased, the performance gap between VHB tape and the silicone sealants decreased. Both materials exhibited specimen defects (voids and imperfections) that reduced creep rupture time to fail. Generally, the presence of a defect in a silicone specimen reduced time to fail to a greater degree than the presence of a defect in a VHB tape specimen. The scatter within replicates of condition set for creep rupture time to failure was greater for the silicone specimens than for VHB tape specimens.

The multi-temperature body of VHB tape creep rupture specimens was converted to a master curve at a single 30°C (86°F) reference temperature using thermal shift factors, based on the time

temperature superposition principle (TTSP). The thermal shifting allowed tests performed under practical time constraints to simulate creep rupture failure times as long as one year. These thermal shifts originated from the relation of DMA-determined constitutive properties at various loading frequencies and temperatures. The shift factors transferred from constitutive properties to creep rupture properties in a manner that produced smooth master curves. A power law relation provides a good fit to these creep rupture master curves.

The same thermal shift factors were applied to the multi-temperature VHB tape ramp-to-fail data, again providing reasonably smooth shear and tensile master curves at a single 30°C (86°F) reference temperature.

Note that the successful application of DMA-generated TTSP shift factors to creep rupture and ramp-to-fail strength was phenomenological, meaning that the application of time temperature superposition was experimentally successful, although it may not be directly explained by theory. A basic assumption of TTSP is that viscoelastic material behavior over a long duration or at a slow loading rate is fundamentally the same as behavior over a short duration or at a fast loading rate, and the first can simulate the second by raising the material temperature. However, the failure mode of the VHB tape creep rupture specimens appeared to change at higher loads and the resulting shorter test durations. Longer tests appeared to produce failures that were more adhesive, and shorter tests appeared to produce failures that were more cohesive. The mechanical process leading to failure was different. However, the observed phenomenon was that DMA-generated thermal shift factors were successful at producing smooth, consistent master curves of strength and creep rupture data.

REFERENCES

3M Technical Guide (2007). VHB Structural Glazing Tape Tech Guide.

Aklonis, J. J. and W. J. MacKnight (1983). Introduction to Polymer Viscoelasticity. New York, John Wiley and Sons.

ASCE (2006). ASCE 7-05 Minimum Design Loads for Buildings and Other Structures. New York, American Society of Civil Engineers.

ASTM-D1002-05 (2005). Standard Test Method for Apparent Shear Strength of Single-Lap-Joint Adhesively Bonded Metal Specimens by Tension Loading (Metal-to-Metal). Annual Book of ASTM Standards. West Conshohocken, ASTM. **15.06**.

ASTM-D1640-04 (2004). Standard Test Method for Assignment of the Glass Transition Temperature by Dynamic Mechanical Analysis. Annual Book of ASTM Standards. West Conshohocken, ASTM. **14.02**.

ASTM-D4065-06 (2006). Standard Practice for Plastics: Dynamic Mechanical Properties: Determination and Report of Procedures. Annual Book of ASTM Standards. West Conshohocken, ASTM. **08.02**.

ASTM-D4092-07 (2007). Standard Terminology for Plastics: Dynamic Mechanical Properties. Annual Book of ASTM Standards. West Conshohocken, ASTM. **08.02**.

Austin, S. and U. Manert (2008). Acrylic Foam Structural Glazing Tapes. International Conference on Durability of Building Materials and Components. Istanbul, Turkey.

Chai, H. (1986). "On the Correlation between the Mode-I Failure of Adhesive Joints and Laminated Composites." Engineering Fracture Mechanics **24**(3): 413-431.

Chartoff, R. P., P. T. Weissman, and A. Sicar (1994). The Application of Dynamic Mechanical Methods to T_g Determination in Polymers: An Overview. Assignment of the Glass Transition, ASTM STP 1249. R. J. Seyler. Philadelphia, American Society for Testing and Materials**:** pp. 88-107.

Dow Corning (2007). Dow Corning Americas Technical Manual.

Heitman, B. T. (1990). Structural Engineering Properties of Acrylic Foam Tapes. MS thesis. Houghton, Michigan Technological University.

Kremer, T. (2005). Useful Design Criteria for Acrylic Foam Tapes in Demanding Industrial Applications. St. Paul, 3M Industrial Adhesives and Tapes Division.

Ward, I. M. and D. W. Hadley (1993). An Introduction to the Mechanical Properties of Solid Polymers. New York, John Wiley & Sons.

Ferry, J. D. (1980). Viscoelastic Properties of Polymers. New York, Wiley.

CHAPTER 3 POSTULATING A SIMPLE DAMAGE MODEL FOR THE LONG-TERM DURABILITY OF STRUCTURAL GLAZING ADHESIVE SUBJECT TO SUSTAINED WIND LOADING

ABSTRACT

This article presents a simple linear damage accumulation model to predict damage from sustained wind speeds on a double sided acrylic foam tape, such as 3M™ VHB™ structural glazing tape, used to attach curtain wall glazing to buildings. The purpose of the model is to investigate the magnitude of damage from the accumulation of sustained wind speeds that are less than the peak design wind speed. The model uses an equation derived from creep rupture testing relating static stress to failure time for VHB tape, extrapolated into the range of stresses that would typically be generated by wind loading. This equation is applied to each individual entry in the data files of several real wind speed histories, and the fractions of life used at each entry are combined into a total percentage of life used. Although the model did not provide evidence that the established design procedure is unsafe, it suggests that the accumulation of damage from wind speeds below the peak wind speed could cause a VHB tape mode of failure that merits examination along with the more traditional peak wind speed design procedure currently recommended by the vendor.

INTRODUCTION

Any construction material used to attach curtain wall glazing panels to building must perform a number of roles. It must be strong enough to withstand short, intense wind loads, while also retaining the compliance to maintain a bond with the glazing panel as the panel undergoes thermal expansion and contraction. Two materials used for this role are structural silicone sealants and VHB structural glazing tape. Manufacturers of these materials have well-established design guidelines to account for peak dynamic load resistance and static dead load resistance (see Dow Corning 2007 and 3M 2007). This article investigates the implications of sustained, wind-induced stresses which are lower than the established allowable dynamic load and greater than the established allowable static load. VHB tape is especially sensitive to the rate or duration of loading (from Chapter 2 of this document), and so this article specifically examines that material,

although the proposed model could apply to any glazing adhesive or sealant if the relation between creep rupture stress and time to failure is known.

Several types of information are required for this analysis:

1. the wind speed history representative of the location of design interest,
2. the equation relating wind speeds to stress on the tape or structural sealant holding glazing on to a building,
3. the required life of the glazing,
4. and the equation, generated from creep rupture data, relating applied constant stress to failure time.

Given all of the above, and based on the assumption that damage done to the VHB tape is cumulative, the fraction of life used at the end of the service life can be generated. The model incorporates wind loading as a multiple-year series of constant loads. Each constant load is the average wind-induced stress over a recording period such as ten minutes or one hour.

Differential thermal expansion and contraction of the glazing components bonded together by VHB tape will also generate shear stresses over the diurnal or annual temperature cycle. This loading mode was not incorporated into the linear damage accumulation model, but a discussion of these effect can be found in Appendix C.

The damage model assumes that after wind-induced damage has accumulated, strength would not be recovered during periods of zero loading. Evidence for or against this proposition is inconclusive, although this project included a side study to investigate the possible healing effect of interrupted loading, as described in Appendix A.

Dalgliesh (1998) proposed a method to model storm wind damage to glass glazing panels, in a manner similar to the model presented in this article to simulate damage on the glazing sealant or adhesive. His approach simulated peak winds using an exponential probability distribution, and then simulated the rest of the storm winds with a Gaussian distribution. The wind-induced stresses were converted to a prediction of damage on the glass glazing panel using a glass-specific cumulative damage equation presented by Brown (1969).

Because the wind loading is simplified to a series of static rather than dynamic loads, the present model does not examine cumulative damage in the form of fatigue. The effect of fatigue from the dynamic, cyclic nature of wind loading is certainly important. However, it is not examined for this project in order to be able to focus specifically on the effect of the long-term, sustained aspect of wind loading, which is known to be a limitation of the acrylic foam tapes (Heitman 1990). Simplifying complex dynamic wind histories down to a series of cumulative static loads also allows the use of real and long-term wind history files. A wind history file that covers many years at a single location will provide data on a recording interval that is too large to directly convey information about the dynamic properties of wind at that location.

Although the analysis of fatigue damage from dynamic wind loading was not undertaken by this research project, much research has been performed in these areas.

Heitman (1990) performed a study that subjected an adhesive tape similar to G23F VHB tape to full-reversal fatigue testing, establishing the relationship between full-reversal stress amplitude and cycles to failure at 0.33 Hz. He found that the compressive portion of the load cycle restored the bond that was damaged during the tension side of the load cycle, and so non-reversing tensile cycling may be a more critical failure mode than the full-reversal mode.

Kumar and Stathopoulos (1998) discussed modeling of wind pressure fluctuations using various probability distributions, in order to perform a fatigue analysis of roof cladding. They found that complex, non-Gaussian probability distributions are the most accurate and conservative method of modeling winds for fatigue life estimates.

Holmes (2007) provided an overview of the use of wind spectra to describe the distribution of turbulence with frequency. Spectral density functions such as the von Karman-Harris spectrum can describe not only how often a wind speed will occur, but also how quickly it will vary with time.

These methods of simulating the dynamic nature of wind loading, used in conjunction with fatigue-testing data, would produce a more comprehensive predictive model than the model presented here. However, the decision was made to forego fatigue analysis in order to focus on damage produced by the long-term, sustained aspect of wind loading.

SOURCES OF WIND DATA

For the analysis presented here, the wind data came from two sources. The first was Fowley Rocks, Florida data gathered by the National Data Buoy Center (NDBC 2007). The second was Chicago, Illinois data gathered by a National Weather Service station (NOAA 1995). The Fowley Rocks data consisted of roughly 707,000 data samples on a 10 minute interval, sampled over 15 years (1991 to 2007, excluding 1994 and 1995), at a height of 44 m (144 ft) above ground elevation. This included the close pass of Hurricane Wilma during October of 2005. Recorded data included average wind speed and direction over the 10-minute interval. The Chicago data consisted of roughly 52,000 data samples on a 60-minute interval, taken over six years from 1995 to 2000, and sampled at a height of 44 m (144 ft) above ground elevation. Again, the data included the average speed and wind direction at one-hour intervals.

The use of a 10-minute averaging interval versus a 60-minute averaging interval will influence the damage model results. A larger averaging time will tend to even out and absorb the short-duration peaks in wind speed, which is significant because peaks in wind speed are amplified by the process of converting wind speed to adhesive stress, and again when converting adhesive stress to damage on the structural glazing adhesive. The practical implication of this effect is that the Fowley Rocks data sets, with an averaging interval of 10 minutes, will be somewhat more conservative than the Chicago data set, with an averaging interval of 60 minutes.

The data sets were reduced by removing wind speed readings that were not within a selected 90° range of compass values. The assumption made was that the building face under examination would be a leeward face oriented in the middle of the 90° wind direction range. The 90° range for a particular wind history was selected to encompass the greatest number of wind speed readings, or to include a specific wind event. For Chicago, IL data the selected range was 180° (S) to 260° (WSW), which included the greatest number of wind speed readings. This reduced the number of readings from 52,000 to 18,600. The Fowley Rocks, FL data set was split into two sets. One encompassed the greatest number of wind speed readings but did not include the winds of Hurricane Wilma in 2005. This range was 55° (NE) to 145° (SE), and reduced the number of readings from 707,000 to 356,000. The second included the winds of Hurricane Wilma, which

fell between the range of 155° (SSE) to 245° (WSW), and reduced the data file to 112,000 readings. Fig. 3.1 shows the wind speed and direction during Hurricane Wilma.

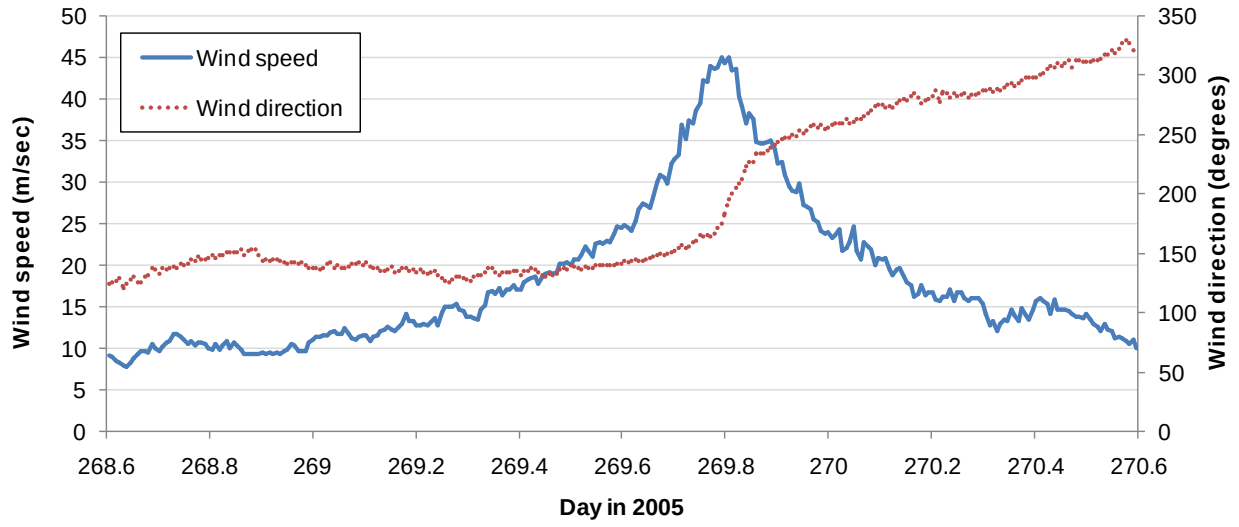

Figure 3.1 Wind speed and direction at Fowley Rocks, FL during Hurricane Wilma, showing average values sampled over ten-minute intervals.

WIND SPEED AND ADHESIVE STRESS

The building design code commonly used in the United States is ASCE 7-05, Minimum Design Loads for Buildings and Other Structures (ASCE 2006). Section 6 of the code relates to wind loading, and contains specific design aids and equations for building cladding. ASCE 7-05 allows designers to convert maximum expected wind speeds into negative pressure on the face of a cladding, using a modified version of Bernoulli's equation. The code supplies a wind chart of the US, which provides the speed of a three-second gust measured at 10 m (33 ft) above the ground. The ASCE 7-05 wind chart is calibrated so the resulting design wind pressure, when combined with the standard load factor of 1.6, will represent a roughly 500-year recurrence interval. The present analysis proposes to modify Section 6 of ASCE 7-05 to process a wind speed and direction data set and produce an equivalent wind pressure data set. In other words, the single peak load is replaced by a series of real wind loads, generating a series of pressures along with the duration that the glazing would experience each pressure.

Design guide equations have been calibrated for wind speeds that occur at 10 m (33 ft) above ground level. However, both the Chicago, IL and Fowley Rocks, FL anemometers used in this analysis were mounted at 44 m (144 ft) above ground level. Due to the lack of a precise factor to apply to correct for the increase in wind speed with elevation, a conservative approach was to use the unmodified 44 m (144 ft) elevation wind speeds.

The standard design method incorporates a directionality factor (K_d), commonly 0.85. This factor is calibrated in conjunction with the standard load combination factors in Section 2 of ASCE-7, and so is not consistent with the purpose of this analysis. Instead of a simple directionality factor, the wind speed data is reduced down to a selected 90° wind direction range. A more complete analysis could include the effects of winds outside of that direction range, and the ASCE-7 building design code does provide equations to determine the pressures on cladding located on the building faces that are windward and parallel to the direction of wind. However, those pressures are small enough in comparison to suction pressure on the leeward side of a building that they are neglected for this analysis (ASCE 2006).

Wind reduces the external pressure (creating suction) on the leeward side of a building, and if a building is enclosed, internal pressure from wind blowing on the windward side of the building contributes to the force pushing the glazing away from the leeward building face. Fig. 3.2 illustrates the conceptual model used by ASCE 7-05 to relate wind and pressure for an enclosed building. These effects are described by the internal pressure coefficient (GC_{pi}) and the external pressure coefficient (GC_p). For an enclosed building, GC_{pi} is given as 0.18, taken as positive or negative to produce the worst case. The highest negative external pressure tends to be on the edges of the leeward face (Holmes 2001), and the design aids in ASCE 7-05 also indicate that this location experiences the greatest pressure, with GC_p given as -1.8 for cladding on the leeward edge and at a height greater than 18 m (60 ft).

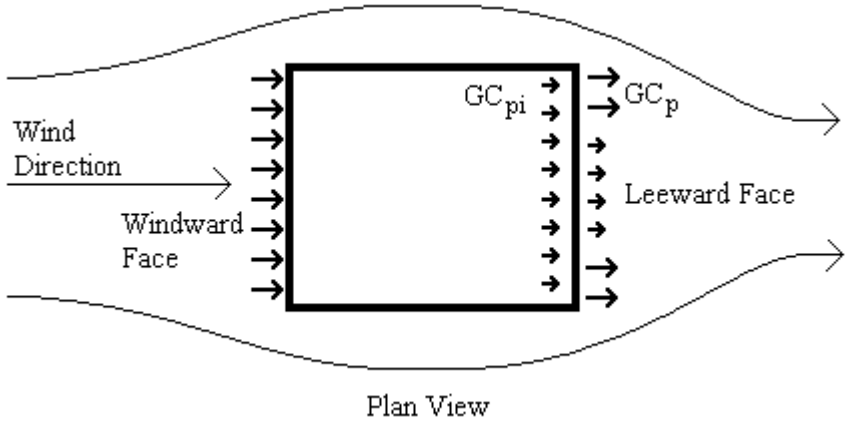

Figure 3.2 Conceptual model relating wind speeds to design pressure.

Other factors incorporated into the design pressure equation include a velocity pressure exposure coefficient (K_z), which accounts for both the height of the glazing and the degree of roughness of nearby terrain. K_z is given as 0.99 for a height of 30.5 m (100 ft) and exposure B, corresponding to urban or suburban areas. An importance factor (I) relates to value and occupant safety concerns. For example, hospitals are assigned an importance factor of 1.15, while office buildings are assigned 1.00. A topographical effect factor (K_{zt}) takes into account nearby hills or escarpments and is left at 1.0 if none are present.

The factors and coefficients described above are tied together by Eq. (3.1) and Eq. (3.2), which are valid for glazing at a height greater than 18.3 m (60 ft):

ASCE 7-05 Eq. 6-15, for V in m/sec and q_h in N/m^2:

$$q_h = 0.613 \cdot K_z \cdot K_{zt} \cdot K_d \cdot I \cdot V^2 \tag{3.1a}$$

ASCE 7-05 Eq. 6-15, for V in mph and q_h in lb/ft^2:

$$q_h = 0.00256 \cdot K_z \cdot K_{zt} \cdot K_d \cdot I \cdot V^2 \tag{3.1b}$$

ASCE 7-05 Eq. 6-23:

$$p = q_h(GC_p) - q_h(GC_{pi}) \tag{3.2}$$

where q_h is velocity pressure at height h and p is design pressure to be used in determination of wind loads for buildings, both in N/m^2 (lb/ft^2). Note that p will be negative, implying that the design pressure is suction away from the building.

Given a wind speed V, Eq. (3.2) provides the negative wind pressure (suction away from building) on the face of a window glazing. An important feature of this conversion is that pressure is equivalent to the square of velocity. This has the effect of amplifying the importance of peak wind speeds when they are incorporated into a damage model.

Given the negative wind pressure on the leeward surface of a building, the next step is to convert wind pressure to stress on the structural adhesive holding the glazing panel on to the building. A logical way to do this is to apply a trapezoidal load distribution as described by Haugsby (1989), shown in Fig. 3.3.

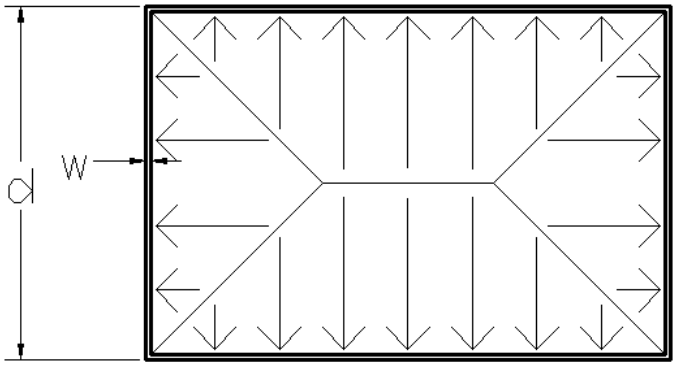

Figure 3.3 Trapezoidal load distribution.

The location of greatest stress on the structural adhesive or sealant would be at the center of the longer edges of the window or panel, and at that location the stress could be determined by Eq. (3.3):

$$\sigma_{\max} = \frac{p \cdot d}{2 \cdot w} \tag{3.3}$$

where p is wind pressure, d is the shorter dimension, and w is the width of the structural adhesive.

PREDICTION OF FAILURE TIME BASED ON ADHESIVE STRESS

Once a series of wind-generated stresses on the glazing adhesive has been generated, the next step is to relate these stresses to a predicted time to failure. Previous research (described in Chapter 2 of this document) has established Eq. (3.4a) and Eq. (3.4b), a power law fit to the tensile creep rupture master curve for G23F VHB structural glazing tape at a 30°C (86°F) reference temperature:

$$\sigma_{creep} = 0.6049 \cdot t_{fail}^{-0.1238} \tag{3.4a}$$

and the inverse:

$$t_{fail} = \left(\frac{0.6049}{\sigma_{creep}} \right)^{8.078} \tag{3.4b}$$

with σ_{creep} in MPa and t_{fail} in seconds. This power law fit is based on a data set of 126 laboratory-prepared VHB tape creep rupture specimens measuring 19.1 mm (0.75 in.) by 50.8 mm (2.00 in.). The specimens simulated a bond between two anodized aluminum adherends. Relative humidity was maintained at 15% to 25% during testing and storage of specimens. Applied static stresses ranged from 0.07 MPa to 0.45 MPa (10 psi to 65 psi). It is important to note that the wind-induced stresses usually remain below 0.07 MPa (10 psi), and so this formula was extrapolated into the low-stress range. In order to accelerate testing which would otherwise take years to complete, time temperature superposition was employed to simulate long-duration tests (Ferry 1980). Testing was performed at two elevated temperatures of 40°C (104°F) and 60°C (140°F) as well as at ambient 23°C (73°F). The thermal shift factors used to perform the time temperature superposition were derived from dynamic mechanical analysis (DMA) of VHB tape specimens. This testing was performed on smaller specimens than those used for creep rupture testing. The shear mode specimens were 10 mm by 10 mm (0.39 in. by 0.39 in.), and the specimens loaded along the 2.3 mm (0.090 in.) thickness of the tape were 12.7 mm (0.50 in.) diameter disks. The response of the specimens to varying load frequencies and varying temperatures can be combined into a master curve at a single reference temperature, simulating data over a wide range of loading frequencies. This master curve provides thermal shift factors

that describe the interrelation of time-dependent material properties and temperature. This interrelation was then applied to creep rupture data, converting tests performed at the three temperatures into a smooth master curve of data that is shifted to simulate the response of the material at 30°C (86°F). Further information regarding time temperature superposition and thermal shift factors can be found in the polymer viscoelasticity texts by Aklonis and Macknight (1983) and by Ward and Hadley (1993).

Fig. 3.4 shows the unshifted data and the resulting master curves of shifted creep rupture data (from Fig. 2.23 of Chapter 2). Each plotted point represents the average of nine replicates.

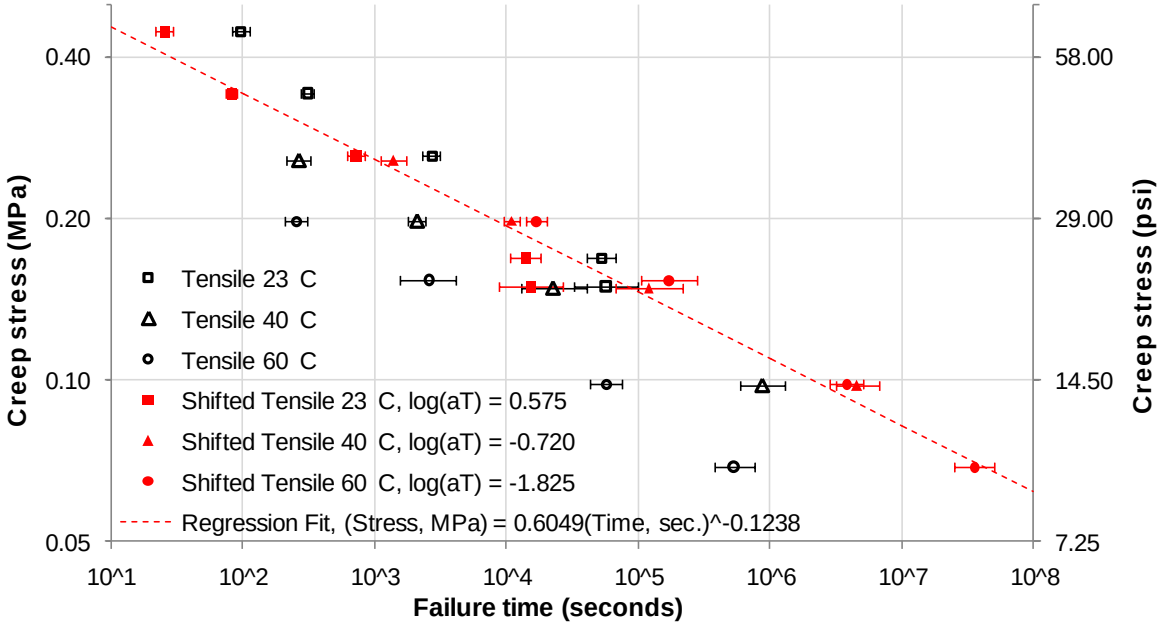

Figure 3.4 Log-log plot of unshifted tensile VHB tape creep rupture data, along with data which has been shifted to 30°C (86°F) reference temperature; each data point is an average of nine replicates, and error bars represent one standard deviation.

To establish a sense of the magnitude of time to failure that corresponds to wind speed, Table 3.1 provides the predicted VHB tape time to failure given a range of constant wind loads. This table was generated using the design parameters of a 1.22 m by 1.83 m (4 ft by 6 ft) glazing panel at 30.5 m (100 ft) elevation from ground, and a VHB tape width of 19.1 mm (0.75 in.).

Table 3.1 Constant Wind Speeds and Resulting Failure Times (based on a best fit of mean failure times for a limited data set)

Constant Wind Speed		VHB Tape Stress		Extrapolated Time to Failure		
m / sec	mph	MPa	lb / in^2	Seconds	Days	Years
5	11.2	0.000962	0.140	4.03E+22	4.67E+17	1.28E+15
10	22.4	0.003849	0.558	5.52E+17	6.39E+12	1.75E+10
20	44.7	0.015395	2.233	7.56E+12	87551789	239867.9
30	67.1	0.034639	5.024	1.08E+10	125122.3	342.8008
40	89.5	0.061580	8.931	1.04E+08	1199.014	3.284971
50	111.8	0.096219	13.955	2816177	32.59464	0.0893
60	134.2	0.138555	20.096	148049.8	1.713539	0.004695
70	156.6	0.188589	27.353	12269.18	0.142004	0.000389
80	179.0	0.246321	35.726	1418.723	0.01642	4.5E-05
90	201.3	0.311749	45.215	211.5814	0.002449	6.71E-06

After the average stress at each time increment had been run through Eq. (3.4b), the duration of the time increment was divided by the predicted time to failure, resulting in a small fraction of VHB tape life used by that average wind-induced stress over the individual time increment.

This concept is similar to the Palmgren-Miner Rule for cumulative fatigue damage (Dowling 2007), shown by Eq. (3.5):

$$D = \sum_{i=1}^{n} \frac{N_i}{N_{fail,i}} \tag{3.5}$$

where D is the fraction of life used (alternately described as damage done), N_i is the number of observed fatigue cycles at a particular stress amplitude, and $N_{fail,\,i}$ is the number of fatigue cycles that will lead to failure at that stress amplitude. These fractions of damage are summed for n stress amplitudes, and failure is predicted to occur when $D = 1$. This simple method of describing the accumulation of damage was first published by Miner (1945).

For this analysis, creep rupture stress replaces stress amplitude, and duration at a particular stress replaces the number of cycles at a particular stress amplitude. The summation of life used is shown by Eq. (3.6):

$$D = \frac{L_s}{L_d} \sum_{i=1}^{n} \frac{t_i}{t_{fail,i}} \tag{3.6}$$

L_d is the length of time encompassed by the wind history data file, L_s is the length of time for the desired service life, n is the number of entries in the wind speed data file, t_i is the time spent during data entry i, and $t_{fail,\,i}$ is the creep rupture time to failure due to the average wind-induced stress at data entry i. The model predicts that failure occurs when the fractions sum to unity, or $D = 1$. The inclusion of the L_s/L_d ratio is necessary if the source data file of wind speeds is too short to represent the life of a glazing installation.

All the equations required to convert a wind speed history into life used are combined and presented in a general form as Eqs. (3.7), (3.8a), and (3.8b):

$$D = \frac{L_s}{L_d} \sum_{i=1}^{n} \frac{t_i}{\left(\dfrac{0.6049}{\Omega \cdot p_i \cdot \dfrac{d}{2w}} \right)^{8.078}} \tag{3.7}$$

$$p_i = 0.613 \cdot K_z \cdot K_{zt} \cdot K_d \cdot I \cdot V_i^{\,2} \cdot (GC_p - GC_{pi}) \cdot \frac{1}{1000000} \left(\frac{\text{MPa}}{\text{Pa}} \right), \quad \text{for } V_i \text{ in m/sec} \tag{3.8a}$$

$$p_i = 0.00256 \cdot K_z \cdot K_{zt} \cdot K_d \cdot I \cdot V_i^{\,2} \cdot (GC_p - GC_{pi}) \cdot \frac{1}{20900} \left(\frac{\text{MPa}}{\text{psf}} \right), \quad \text{for } V_i \text{ in mph} \tag{3.8b}$$

Definition of terms: (values in parentheses are those used for plots and tables in the results and discussion section)

- D Fraction of life used, or fraction of damage done by end of service life
- L_s Duration of service life, in years (50 years)
- L_d Duration of wind speed data file, years (15 years for Fowley Rocks, FL and 6 years for Chicago, IL)
- n Number of entries in wind speed data file
- i Designation of individual entry in wind speed data file
- t_i Duration of individual entry, in seconds
- Ω Safety factor

d Length of shorter dimension of rectangular glazing panel, mm or in. (1220 mm, 48 in.)

w Width of VHB tape, mm or in. (19.1 mm, 0.75 in.)

p_i Wind pressure on glazing panel for entry in wind speed data file, in MPa to match creep rupture terms

V_i Wind speed from individual entry in source data file, mph or m/sec – data file should be reduced to encompass a 90° range of wind directions, which represents the worst case

Terms from ASCE 7-05:

K_z Velocity pressure exposure coefficient (0.99 for 30.5 m (100 ft) height, exposure B)

K_{zt} Topographical effect factor (1.0 for no nearby hills or escarpments)

K_d Directionality factor (1.0; directionality accounted for by sampling 90° direction range of wind speeds)

I Importance factor (1.0 for office building)

GC_p External pressure coefficient (−1.8 for edge of leeward face of building)

GC_{pi} Internal pressure coefficient (0.18 for enclosed building)

The safety factor term (Ω) is placed so that it operates directly on the wind pressure term along with the glazing design parameters d and w.

If the specific parameters given above in parenthesis are substituted into Eq. (3.7), then the specific relation between D and the combined entries of a wind speed data file is given by Eq. (3.9a) or Eq. (3.9b):

$$D = 3.22 \times 10^{-49} \left(\Omega \frac{d}{w} \right)^{8.078} \frac{L_s}{L_d} \sum_{i=1}^{n} (t_i \cdot V_i^{16.16}), \quad \text{for } V_i \text{ in m/sec} \tag{3.9a}$$

$$D = 7.22 \times 10^{-55} \left(\Omega \frac{d}{w} \right)^{8.078} \frac{L_s}{L_d} \sum_{i=1}^{n} (t_i \cdot V_i^{16.16}), \quad \text{for } V_i \text{ in mph} \tag{3.9b}$$

RESULTS AND DISCUSSION

The plots and figures of this section are the result of running the three wind histories through the simple linear damage accumulation model as presented by Eq. (3.9a) and Eq. (3.9b). The Chicago, IL wind history is selected as a representative example of high, sustained wind speeds at a location in the interior of the U.S. The two Fowley Rocks, FL wind histories are selected to represent coastal wind speeds with and without a near pass by a hurricane.

The linear damage accumulation model predicts the values listed in Table 3.2 when no safety factor is included in the analysis, the glazing panel length *d* is set to 1220 mm (48 in.), VHB tape width *w* is set to 19.1 mm (0.75 in.), and the analysis is extrapolated to a 50-year service life. Note that the resulting fractions of life used are nearly zero; however, the inclusion of a safety factor term would increase the predictions by a power of 8.08. Similarly, design parameters (*w*, *d*) that have a direct relation to stress would influence the predicted fraction of life used by a power of 8.08. This is due to the high sensitivity of VHB tape creep rupture failure time to small changes in creep rupture stress.

Table 3.2 Predicted Damage With No Safety Factor

Wind history	Fraction of life used (for duration of wind history)	Fraction of life used (extrapolated to 50 year service life)
Chicago, IL	5.65×10^{-12} (6 years)	4.71×10^{-11}
Fowley Rocks, FL no hurricane	5.51×10^{-7} (15 years)	1.84×10^{-6}
Fowley Rocks, FL Hurricane Wilma	3.09×10^{-4} (15 years)	1.03×10^{-3}

The relation of frequency of wind speeds to the predicted fraction of life used at those wind speeds is demonstrated in Figs. 3.5, 3.6, and 3.7. Tables 3.3, 3.4, and 3.5 provide tabulated values of top wind speeds and accompanying life used. The fractions of damage as presented in these plots and tables are normalized by dividing by the life fraction used by the end of the analysis. In other words, 100% life used does not mean the tape has failed; at 100%, all the predicted damage had occurred for the period under examination. The purpose of this

normalization was to more easily examine the relative damage contribution of the categories of wind speed at a given location.

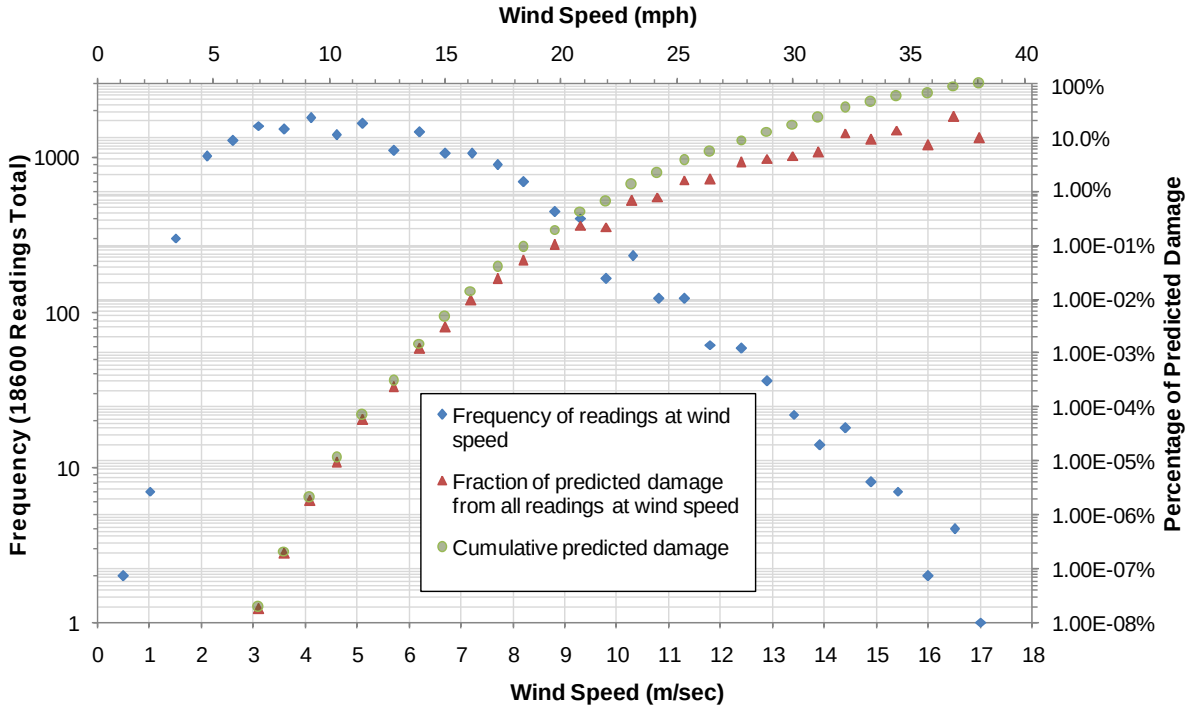

Figure 3.5 Frequency of readings and percentage of predicted damage from wind speeds at Chicago, IL.

Table 3.3 Top Wind Speeds and Accompanying Life Used at Chicago, IL

Wind speed (only speeds with at least one reading shown)		Frequency (out of 18600 readings)	Hours at wind speed	Percentage of damage due to all readings at wind speed
in m/sec	in mph			
17	38.0	1	1.00	9.8%
16.5	36.9	4	4.00	24.3%
16	35.8	2	2.00	7.4%
15.4	34.4	7	7.00	13.9%
14.9	33.3	8	8.00	9.4%
14.4	32.2	18	18.00	12.1%
13.9	31.1	14	14.00	5.3%
13.4	30.0	22	22.00	4.6%
12.9	28.9	36	36.00	4.1%
12.4	27.7	59	59.00	3.5%
11.8	26.4	62	62.00	1.7%
11.3	25.3	123	123.00	1.6%
< 11.3	< 25.3	18244	3041	2.1%

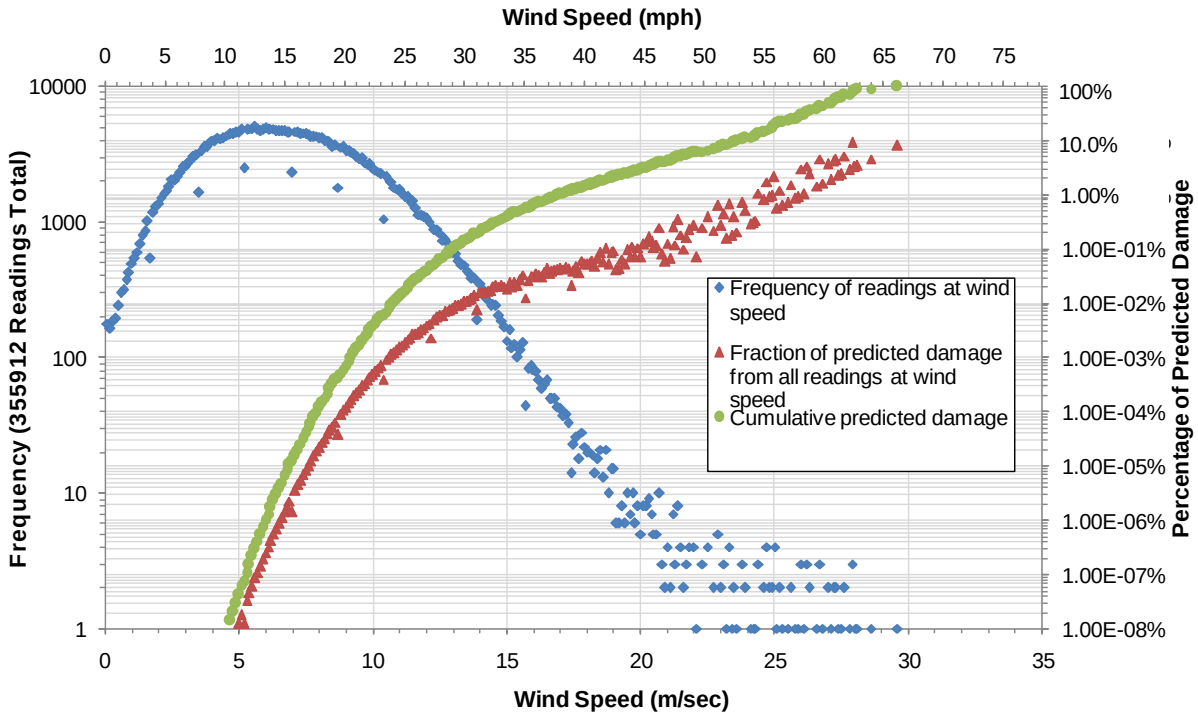

Figure 3.6 Frequency of readings and percentage of predicted damage from wind speeds at Fowley Rocks, FL, without hurricane winds.

Table 3.4 Top Wind Speeds and Accompanying Life Used at Fowley Rocks, FL, Without Hurricane Winds

Wind speed (only speeds with at least one reading shown)		Frequency (out of 355912 readings)	Hours at wind speed	Percentage of damage due to all readings at wind speed
in m/sec	in mph			
29.6	66.2	1	0.17	8.1%
28.6	64.0	1	0.17	4.7%
28.1	62.9	1	0.17	3.5%
28	62.6	1	0.17	3.3%
27.9	62.4	3	0.50	9.4%
27.8	62.2	1	0.17	2.9%
27.6	61.7	2	0.33	5.2%
27.5	61.5	1	0.17	2.5%
27.4	61.3	1	0.17	2.3%
27.3	61.1	2	0.33	4.4%
27.2	60.8	2	0.33	4.1%
27.1	60.6	1	0.17	2.0%
27	60.4	2	0.33	3.7%
26.8	59.9	1	0.17	1.6%
26.7	59.7	3	0.50	4.6%
26.6	59.5	1	0.17	1.4%
26.3	58.8	2	0.33	2.4%
< 26.3	< 58.8	355886	59314	33.7%

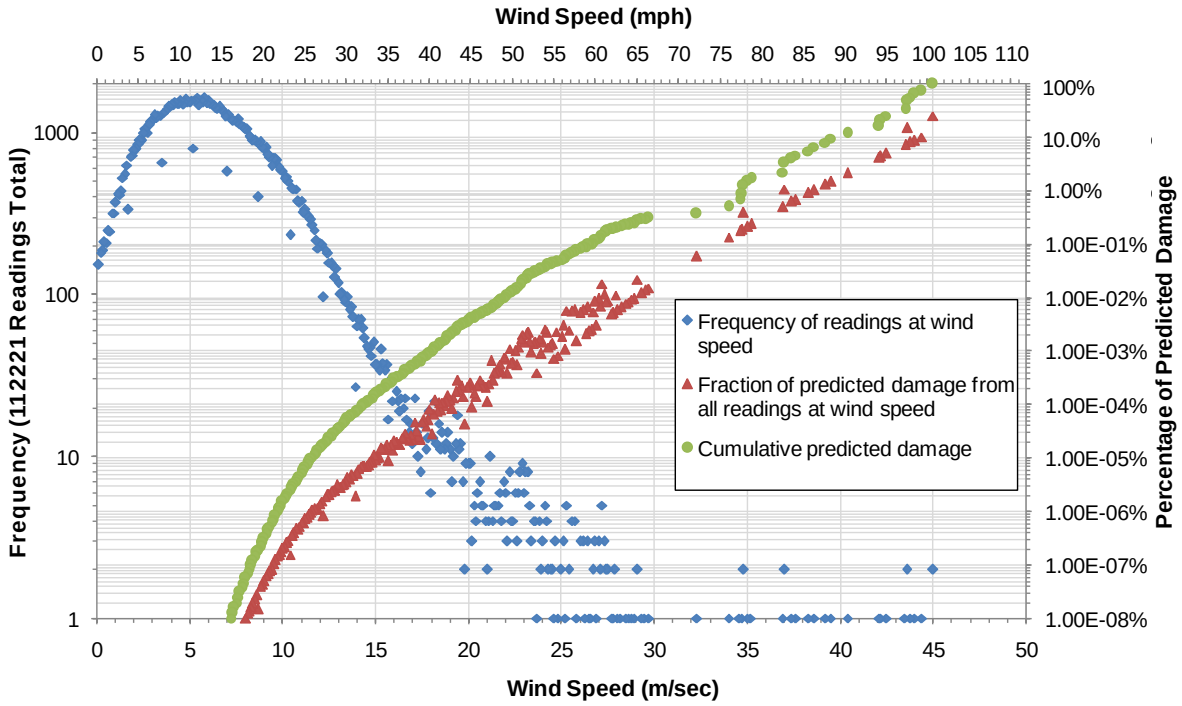

Figure 3.7 Frequency of readings and percentage of predicted damage from wind speeds at Fowley Rocks, FL, including hurricane winds.

Table 3.5 Top Wind Speeds and Accompanying Life Used at Fowley Rocks, FL, Including Hurricane Winds

Wind speed (only speeds with at least one reading shown)		Frequency (out of 112221 readings)	Hours at wind speed	Percentage of damage due to all readings at wind speed
in m/sec	in mph			
45.0	100.7	2	0.33	25.2%
44.4	99.3	1	0.17	10.1%
44.0	98.4	1	0.17	8.8%
43.8	98.0	1	0.17	8.1%
43.6	97.5	2	0.33	15.1%
43.5	97.3	1	0.17	7.3%
42.5	95.1	1	0.17	5.0%
42.2	94.4	1	0.17	4.5%
42.1	94.2	1	0.17	4.3%
40.4	90.4	1	0.17	2.2%
39.5	88.4	1	0.17	1.5%
39.2	87.7	1	0.17	1.4%
38.6	86.3	1	0.17	1.1%
38.3	85.7	1	0.17	0.9%
37.6	84.1	1	0.17	0.7%
37.4	83.7	1	0.17	0.6%
37.0	82.8	2	0.33	1.1%
< 37.0	< 82.8	112201	18700	2.2%

For the Fowley Rocks analysis which included Hurricane Wilma, approximately 98% of the life used during the analysis was a result of the 17 highest wind speed readings, which equated to the top 2.8 hours out of the total of 18,703 hours of data (2.8 / 18,703 = 0.015%). For the Fowley Rocks analysis, which excluded Hurricane Wilma, approximately 98% of the life used was a result of the 82 highest wind speed readings, which equated to the top 13.7 hours out of the total of 59,319 hours of data (13.7 / 59,319 = 0.023%). For the Chicago analysis, approximately 98% of the life used was a result of the 356 highest wind speed readings, which equated to the top 356 hours out of the total of 18,600 hours of data (356 / 18,600 = 1.9%). Again, in this discussion the term "100% of life used" does not mean that the VHB tape had failed according to the damage model. The percentages given above are not scaled so that the model predicts failure at 100%. Instead, all the damage that will be done (such as the values in Table 3.2) had occurred at 100%. The percentages provide information on the relative importance of various categories of wind speeds.

Another way to visualize the relative importance (in terms of life used) of various wind speeds is to plot the range of wind-induced stresses against the amount of time that the VHB tape will experience those stresses during the recorded wind histories. If the creep rupture prediction line is plotted on the same figure, then information could be gathered by comparing the slope of the creep rupture line against the slope of the distribution of the real wind-induced stresses. Fig. 3.8 through Fig. 3.11 may help illustrate this concept.

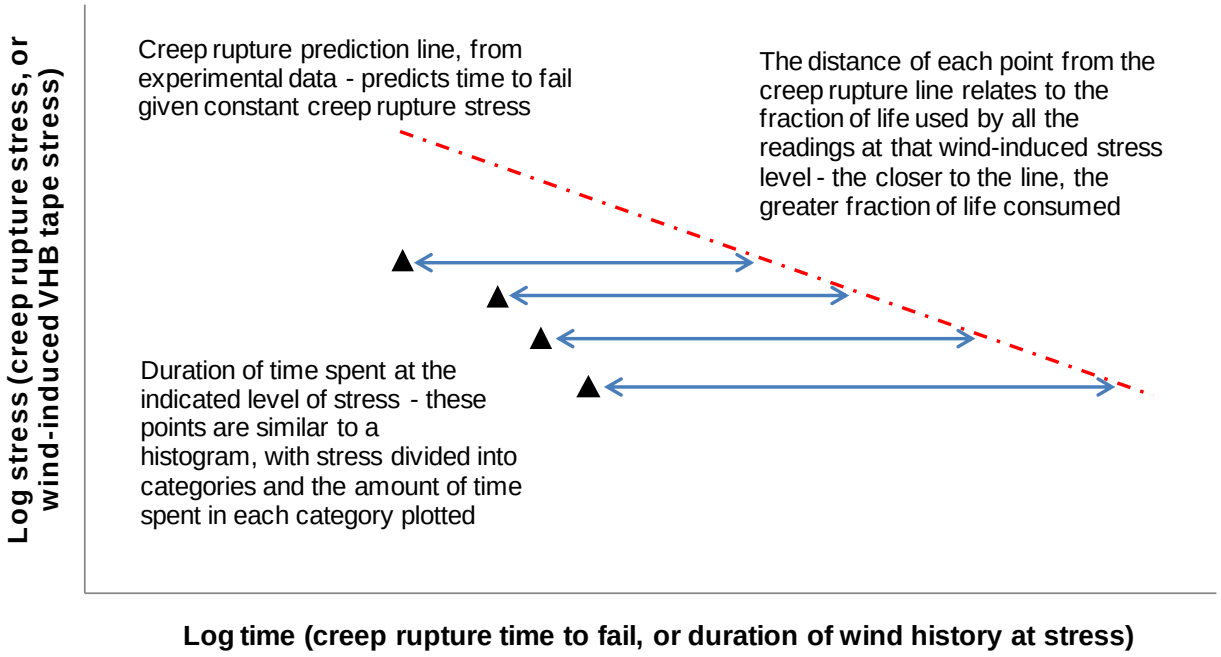

Figure 3.8 Illustration of comparison between creep rupture line and wind-induced stress distribution.

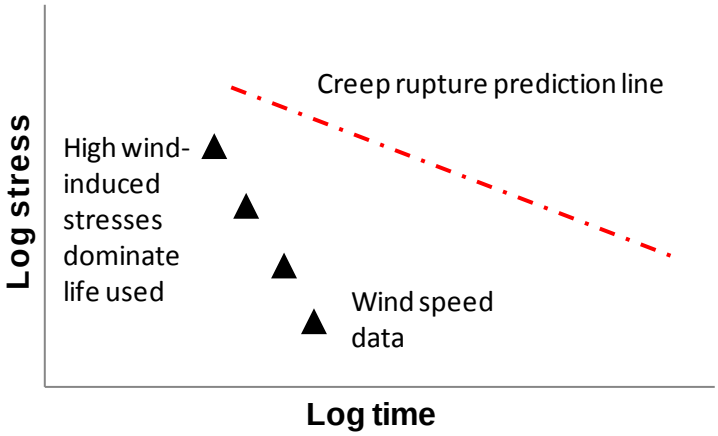

Figure 3.9 Comparison between creep rupture line and wind-induced stress distribution where high wind-induced stresses dominate life used.

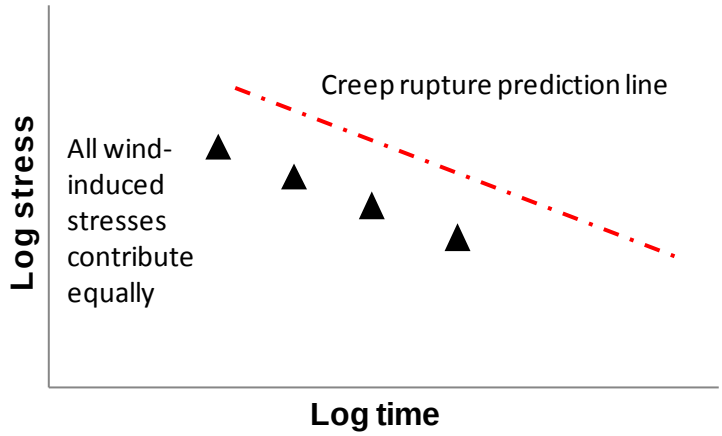

Figure 3.10 Comparison between creep rupture line and wind-induced stress distribution where all wind-induced stresses contribute equally.

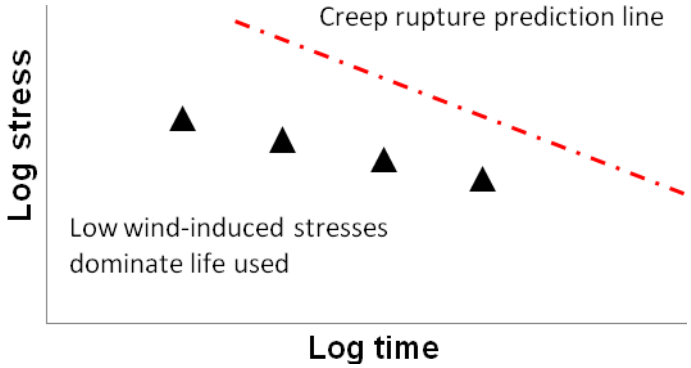

Figure 3.11 Comparison between creep rupture line and wind-induced stress distribution where low wind-induced stresses dominate life used.

Fig. 3.12 presents the actual distribution of wind-induced stresses compared to the creep rupture prediction line from Eq. (3.4). Note that the Fowley Rocks data set with a hurricane includes more readings at high wind speeds and fewer readings at lower wind speeds compared to the Fowley Rocks data set without a hurricane. This is because the 90° compass sampling range of the data set without a hurricane included a greater quantity of wind speed readings over the 15 year sampling duration, even though the close pass of Hurricane Wilma in 2005 did not produce winds in those directions.

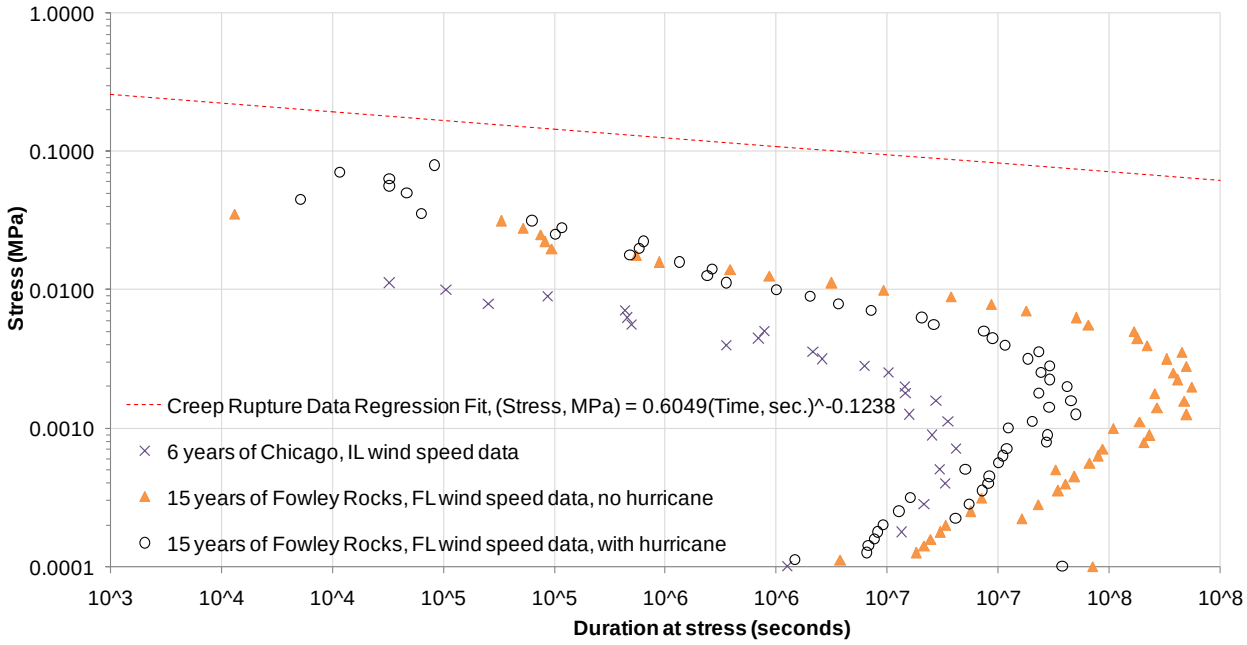

Figure 3.12 Comparison between creep rupture line and wind-induced stress distributions.

For all three wind histories, the slope of the points representing the top (roughly > 0.004 MPa) wind-induced stresses is similar to the slope of the creep rupture prediction line, although the higher stresses tend to contribute more to the percentage of life used. The same conclusion could be drawn from Tables 3.3, 3.4, and 3.5. To put these results into perspective, the standard peak load design methodology contains the inherent assumption that 100% of the life is used by the highest expected wind-induced stress and all lesser stresses contribute negligible damage, no matter the duration.

Compared to VHB tape, the structural silicone sealant creep rupture time to failure is less sensitive to variations of the creep rupture stress (from Chapter 2 of this document). This means that the silicone creep rupture prediction line would be flatter, increasing the relative importance of the higher wind-induced stresses for that material. Accordingly, structural silicones are more suited to the traditional peak stress design procedure than VHB tape.

The existing design procedure established by 3M for the resistance of wind loading on glazing with VHB tape is simple, and follows the allowable strength design methodology (also known as permissible stress). Using this design method, the peak wind-induced stress (S) is specified for a given return period. If the ASCE 7-05 design code is used, S is the stress resulting from the

maximum three-second gust that is expected to occur over a desired return period (ASCE 7-05 commentary). On the resistance side, 3M has performed the testing to establish a dynamic stress resistance, which is the stress that VHB tape can sustain for short-term, dynamic loads such as produced by the peak three-second gust (Kremer 2005). The experimentally established resistance is then divided by a safety factor (Ω) of five, resulting in the value 85 kPa (12 psi) as an allowable dynamic stress on VHB tape. This value, when combined with design parameters such as the size of glazing panels and width of VHB tape, results in the resistance ΩR. The design parameters must be sized so that

$$\Omega R > S \tag{3.10}$$

Using this methodology, the required VHB tape width is 31.8 mm (1.25 in.) for Fowley Rocks and 12.7 mm (0.50 in.) for Chicago, using a 1.22 m by 1.83 m (4 ft by 6 ft) glazing panel and the same ASCE 7-05 parameters that were used to generate Eq. (3.9a) and Eq. (3.9b). The three-second peak gust wind speeds used for this calculation are 40 m/sec (90 mph) for Chicago, IL and 65 m/sec (145 mph) for Fowley Rocks, FL (ASCE 7-05).

The application of a factor of safety to the linear damage accumulation model presented in this document is less straightforward. The approach incorporated into Eq. (3.9a) and Eq. (3.9b) was to apply the safety factor Ω to the wind-induced stress. The load effect S was then interpreted as the multi-year series of wind-induced stresses determined from a real history of wind speeds. The resistance ΩR was that same wind-induced stress history, increased by the factor Ω so that the accumulation of life used (D) reached unity at the end of the desired service life. The safety factors generated by this method are presented in Tables 3.6, 3.7 , and 3.8. These tables present safety factors at various tape widths, using the assumption that the stress on the tape will be directly and inversely related to the width. However, the creep rupture prediction equation was originally performed using 19.1 mm (0.75 in.) wide VHB tape specimens.

Table 3.6 Chicago, IL Safety Factors Corresponding to 50 Year Service Life

VHB adhesive tape width	Safety Factor Ω
31.8 mm (1.25 in.)	19.0
25.4 mm (1.00 in.)	15.2
19.1 mm (0.75 in.)	11.4
12.7 mm (0.50 in.)	7.6

Table 3.7 Fowley Rocks, FL Safety Factors Corresponding to 50 Year Service Life With No Hurricane

VHB adhesive tape width	Safety Factor Ω
31.8 mm (1.25 in.)	8.6
25.4 mm (1.00 in.)	6.8
19.1 mm (0.75 in.)	5.1
12.7 mm (0.50 in.)	3.4

Table 3.8 Fowley Rocks, FL Safety Factors Corresponding to 50 Year Service Life With Hurricane

VHB adhesive tape width	Safety Factor Ω
31.8 mm (1.25 in.)	3.9
25.4 mm (1.00 in.)	3.1
19.1 mm (0.75 in.)	2.3
12.7 mm (0.50 in.)	1.6

A discussion of safety factors is incomplete without examining the probability that a given safety factor will be exceeded. Statistical variation of resistance *R* and load effect *S* can be accounted for with the safety index β (also known as the reliability index), given for the case where *R* and *S* are normally distributed (Gaussian) variables by Eq. (3.11):

$$\beta = \frac{\mu_R - \mu_S}{\sqrt{\sigma^2{}_R + \sigma^2{}_S}} \tag{3.11}$$

where μ represents the mean value and σ represents the standard deviation of *R* or *S* (Madsen 1986). The safety index relates directly to the probability of failure p_f by Eq. (3.12):

$$\beta = \Phi^{-1}(1 - p_f) \tag{3.12}$$

where $\Phi(\ )$ is the normal (Gaussian) cumulative probability distribution of a unit variate (i.e. $\mu = 0$ and $\sigma = 1$) (Holmes 2007). Table 3.9 presents this relation evaluated for specific probabilities of failure.

Table 3.9 Relation Between Probability of Failure and Safety Index

Probability of failure p_f	Safety index β
0.1	1.282
0.01	2.326
0.001	3.09
0.0001	3.719
0.00001	4.265

The safety index can be evaluated directly for normal (Gaussian) or lognormal probability distributions, but for more complex probability distributions such as Weibull, reverse Weibull, Gumbel, or Rayleigh distributions, numerical methods must be employed (Holmes 2007). Normal or lognormal distributions are usually not the best fit of *R* and *S* for wind design; according to Simiu (2001), wind speeds (peak wind speeds especially) are best characterized by a reverse Weibull distribution.

R and *S* are also combinations of separate random variables, which adds a further level of complexity when attempting to determine the safety index for wind design. For example, determining the history of wind-induced stresses that represent the load effect S involves multiple parameter uncertainties, defined by Blockley (1980) as "the lack of dependability of theoretical propositions concerning the parameters of the theoretical model used to represent the proposed structure, assuming that the model is precise." Such parameters include wind speeds, width of VHB tape, size of the glazing panel, location of the glazing panel on the building, and the ASCE 7-05 parameters related to the effects of building location and surrounding terrain. Errors in these parameters could result from the process of collecting wind speeds, incorrect application of the VHB tape, or miscalculations in the design process.

Likewise, determining the resistance predicted by the linear damage accumulation model contains a significant degree of system uncertainty, defined by Blockley (1980) as "the lack of dependability of a theoretical model when used to describe the behavior of a proposed structure, assuming a precisely defined set of parameters describing the model." For example, the creep rupture prediction line was developed from a limited experimental data set, and furthermore had to be extrapolated down into a range of wind-induced stresses smaller than the experimental stresses used to develop the prediction line. Another example of system uncertainty relates to the

size of the sampling interval of the source wind speed history. If the sampling interval was large, such as one hour, then wind speed peaks were ignored as all wind speeds during the sampling interval were averaged into one value. Because wind speeds were squared when converted to stress on the adhesive, those peak values could contribute a significant portion of damage, but were not accounted for by the linear damage accumulation model.

CONCLUSIONS

The goal of this study was to investigate the effects of sustained wind-induced stresses on VHB tape, a time dependent viscoelastic material used to attach curtain wall glazing panels to buildings. Previous research established time dependent creep rupture data, and this was incorporated into a simple linear damage accumulation model. Wind histories were examined from several representative locations, with one loading history including a near pass by a hurricane.

Based on the experimental data from laboratory tests and design methodology described in this research, time dependent adhesives or sealants used in glazing applications are likely to experience some damage from sustained wind loading over the life of an installation. A general conclusion suggested by this analysis, however, is that a curtain wall glazing system utilizing VHB tape and designed to withstand the traditional single peak wind load is not likely to fail due to the accumulation of many years of low and intermediate sustained wind loads. This conclusion is based on safety factors corresponding to a 50 year analysis of two locations, using representative parameters relating to the building location, location of the glazing panel on the building, and size of the glazing panel. Using these assumptions, the safety factor from the linear damage accumulation model was greater than the safety factor currently incorporated into the established peak load design procedure, when examining wind loading at Chicago, IL and Fowley Rock, FL without a hurricane event. For the Fowley Rocks wind history that did include a close pass by a hurricane, the safety factor from the linear damage accumulation model was slightly less than from established design procedure.

These conclusions must be considered along with the following caveats:

1. The linear damage accumulation model examined only the sustained aspect of wind loading, such as provided by average wind speeds over ten minutes or one hour, and not fatigue loading.
2. The reliability index has not been established for the safety factors provided by the model, and so it is not possible at this time to compare the exact probability of failure of the two design methods.
3. The testing that established the creep rupture prediction equation was performed at stresses greater than those usually generated by winds, and had to be extrapolated into the range of low stress and long time to failure. The use of time temperature superposition helped to partially alleviate this problem by simulating longer tests with higher temperature.
4. The linear damage accumulation model assumed no residual strength recovery takes place during periods of no stress on the VHB tape.
5. The linear damage accumulation damage model and creep rupture prediction equations have not been validated with long-term testing over months or years, nor with forensic investigations of real VHB tape installations.
6. Although the wind histories examined here were picked to represent conservative examples of locations with high sustained wind speeds, other locations may be more critical in providing sustained, unidirectional wind speeds and storm events.

Beyond the quantitative comparison between the proposed linear damage accumulation model and established design procedure, there are several qualitative conclusions established by this study that are less dependant on the assumption listed above. First, the model suggests that storm events and hurricanes contribute wind-induced stresses that use up several orders of magnitude more VHB tape life compared to everyday wind speeds, even at locations such as Chicago and the coast of Florida which exhibit high sustained wind speeds on a regular basis. Second, the model indicates that all of the wind speed readings making up the highest 0.02% of reading at Fowley Rocks, Florida have a similar magnitude of importance in terms of fractions of life used. The same was true for the top 2% of readings at Chicago, Illinois. Even though these readings

only account for a handful of hours or days out of the entire multi-year wind speed histories, the linear damage accumulation model suggests that these sustained wind-induced stresses from speeds below the expected peak speed might represent an important loading mode for VHB tape used to attach curtain wall glazing panels.

REFERENCES

3M Technical Guide (2007). VHB Structural Glazing Tape Tech Guide.

Aklonis, J. J. and W. J. MacKnight (1983). Introduction to Polymer Viscoelasticity. New York, John Wiley and Sons.

ASCE (2006). ASCE 7-05 Minimum Design Loads for Buildings and Other Structures. New York, American Society of Civil Engineers.

Austin, S. and U. Manert (2008). Acrylic Foam Structural Glazing Tapes. International Conference on Durability of Building Materials and Components. Istanbul, Turkey.

Blockley, D. I. (1980). The Nature of Structural Design and Safety. Chichester, Ellis Horwood.

Brown, W. G. (1969). A load duration theory for glass design. Annual Meeting of the International Commission on Glass, Toronto, National Research Council of Canada.

Dalgliesh, W. A. (1998). Design of glass and glazing for wind pressure and rain. Jubileum Conference on Wind Effects on Buildings and Structures, Porto Alegre, Brazil, A. A. Balkema.

Dow Corning (2007). Dow Corning Americas Technical Manual.

Dowling, N. (2007). Mechanical Behavior of Materials. Upper Saddle River, New Jersey, Pearson Prentice Hall.

Ferry, J. D. (1980). Viscoelastic Properties of Polymers. New York, Wiley.

Heitman, B. T. (1990). Structural Engineering Properties of Acrylic Foam Tapes. MS thesis. Houghton, Michigan Technological University.

Holmes, J. D. (2007). Wind Loading of Structures. New York, Taylor & Francis.

Kremer, T. (2005). Useful Design Criteria for Acrylic Foam Tapes in Demanding Industrial Applications. St. Paul, 3M Industrial Adhesives and Tapes Division.

Kumar, K. S. and T. Stathopoulos (1998). "Fatigue analysis of roof cladding under simulated wind loading." Journal of Wind Engineering and Industrial Aerodynamics **77&78**: 171-183.

Madsen, H. O., S. Krenk, et al. (1986). Methods of Structural Safety. Englewood Cliffs, NJ, Prentice-Hall.

Miner, M. A. (1945). "Cumulative damage in fatigue." Journal of Applied Mechanics **12**: 159-164.

NDBC. (11-8-2007). "National Data Buoy Center." from http://www.ndbc.noaa.gov/.

NOAA (1995). Hourly United States Weather Observations (1990-1995) CD-ROM.

Simiu, E., et al. (2001). "Extreme wind load estimates based on the Gumbel distribution of dynamic pressures: an assessment." Structural Safety **23**(3): 221-229.

Ward, I. M. and D. W. Hadley (1993). An Introduction to the Mechanical Properties of Solid Polymers. New York, John Wiley & Sons.

CHAPTER 4 CONCLUSIONS

The conclusions from this project are split into two categories: conclusions relating to the first article presented in Chapter 2, and conclusions relating to the second article presented in Chapter 3.

The experimental testing and analysis performed in Chapter 2 established the relation between loading, time, and temperature for G23F VHB tape. The majority of the research effort was directed at generating a large and statistically significant body of tensile and shear creep rupture data. With the aid of a 72-station pneumatic creep frame, 270 VHB tape creep rupture specimens were tested at three temperatures. Three kinds of structural silicone sealants totaling 252 specimens were tested at ambient temperature for the purpose of comparison. In addition to creep rupture testing, shear and tensile ramp-to-fail testing was performed on 54 VHB tape specimens at three rates of strain and three temperatures. The three varieties of silicones, totaling 54 specimens, were tested at three rates of strain and ambient temperature.

For Chapter 2, the following conclusions are made:

1. Parallel testing of VHB tape and structural silicone sealants highlighted the distinct strengths of the two structural glazing materials. For VHB tape, the creep rupture time to failure was more sensitive to applied creep rupture stress, and the ultimate strength during ramp-to-fail tests was more sensitive to applied rate of strain. The one-component DC 995 sealant (S1) and two-component DC 983 sealant (S2) generally lasted longer than VHB tape under the applied creep rupture loads, and provided higher ultimate strength at most ramp-to-fail strain rates. The one-component DC 795 sealant (S3) performed slightly better than VHB tape for creep rupture time to failure, and provided equivalent performance under ramp-to-fail loading. However, as the creep stress and rates of strain increased, the performance gap between VHB tape and the silicones decreased. Both materials exhibited specimen defects (voids and imperfections) that reduced creep rupture time to fail. Generally, the presence of a defect in a silicone specimen reduced time to fail to a greater degree than the presence of a defect in a VHB tape specimen.

2. The multi-temperature body of VHB tape creep rupture specimens could be successfully converted to a master curve at a single 30°C (86°F) reference temperature using thermal shift factors, based on the concept of time temperature superposition (TTSP). The thermal shifting allowed tests performed under practical time constraints to simulate creep rupture failure times as long as one year. These thermal shifts originated from the relation of DMA-determined constitutive properties at various loading frequencies and temperatures. The shift factors transferred from constitutive properties to creep rupture properties in a manner that produced smooth master curves. A power law relation provides a good fit to these creep rupture master curves.
3. The same thermal shift factors were applied to the multi-temperature VHB tape ramp-to-fail data, again providing reasonably smooth shear and tensile master curves at a single 30°C (86°F) reference temperature.
4. The successful application of DMA-generated TTSP shift factors to creep rupture and ramp-to-fail strength was phenomenological. A basic assumption of TTSP is that viscoelastic material behavior over a long duration or at a slow loading rate is fundamentally the same as behavior over a short duration or at a fast loading rate, and the first can simulate the second by raising the material temperature. However, the failure mode of the VHB tape creep rupture specimens appeared to change at higher loads and the resulting shorter test durations. Longer tests appeared to produce failures that were more adhesive, and shorter tests appeared to produce failures that were more cohesive. The mechanical process leading to failure was different. Nevertheless, the process of applying DMA-generated thermal shift factors was phenomenologically successful at producing smooth, consistent master curves. Interestingly, the same shift factors produced a smooth 30°C (86°F) reference master curve when applied to multi-temperature data relating failure surface to creep rupture failure time.

The simple linear damage accumulation model in Chapter 3 proposed to explore the damage produced by real wind histories of sustained, wind-induced stresses on the structural sealant or adhesive used to attach curtain wall glazing panels to buildings. The damage model incorporated

an equation fit to VHB tape creep rupture data from Chapter 2, and so conclusions derived from the model are specific to VHB tape.

For Chapter 3, the following conclusions are made:

1. When comparing the safety factors provided by the linear damage accumulation model with those provided by the established peak wind gust design procedure, the linear damage model safety factors are higher with the exception of a close pass by a hurricane.
2. A reliability index would need to be established in order to determine the exact probability of failure that is associated with the safety factors of the two design methods. Due to this statistical uncertainty and to the unresolved system uncertainties, this simple linear damage accumulation model should not be considered a design equation that can be relied upon to provide specific predictions for failure due to the accumulation of wind-induced stresses.
3. When comparing life used by similar wind speed histories, the inclusion of a hurricane wind event will dominate the analysis. Life used by hurricane wind speeds was predicted to be several orders of magnitude greater than damage done by non-hurricane winds. Additionally, the non-hurricane winds at Fowley Rocks, FL did several orders more damage than the Chicago, IL wind history.
4. All of the wind speed readings making up the highest 0.02% of reading at Fowley Rocks, FL were nearly equally important in terms of fraction of life used. The same was true of the top 2% of readings at Chicago, IL. Even though these readings only accounted for a handful of hours or days out of the entire multi-year wind speed histories, the linear damage accumulation model suggested that wind-induced stresses from speeds below the expected peak speed might represent an important loading mode for VHB tape used to attach curtain wall glazing.

FUTURE WORK

- Determination of the response of VHB tape to cyclic fatigue would be invaluable. A series of experiments examining the non-reversing tensile cycles to failure at several frequencies and several stress amplitudes could be combined with a dynamic wind-induced history simulated using wind spectra, and then incorporated into the linear damage accumulation model. This would result in a damage model that incorporates the effect of both sustained winds and short-term fluctuations.
- The linear damage accumulation model could be further refined by accounting for the occasions when a glazing panel will not be oriented leeward to the wind direction. ASCE 7-05 does provide equations to calculate the wind-induced stresses along the sides and windward faces of a building.
- Another method of refining the linear damage accumulation model would be to account for the recorded temperature and humidity at each entry in the historical data file. The creep rupture equation could be modified to incorporate those terms, with higher temperature and humidity reducing the time to failure at a given stress.
- Long-term validation of the creep rupture data that was simulated by TTSP would be desirable. This could be accomplished through forensic investigation of aged VHB tape glazing installations, or through long-term, low-stress laboratory tests.

APPENDIX A

Damage and Healing

A wind loading history will have interspersed periods of calm winds that produce nearly zero stress. The linear damage accumulation model assumes that these periods of no loading do not allow the tape to recover strength lost due to previous periods of stress. The purpose of this side study was to explore the effect of interrupted loading (periods of zero load during the loading profile) on the residual strength of VHB tape, and see if a healing factor would be appropriate to incorporate into a cumulative damage model. Tensile VHB tape specimens were loaded in an Instron test frame at a constant stress of 0.171 MPa (24.8 psi) and a temperature of 23°C (73°F). Creep rupture data indicated that the average tensile VHB tape failure time would be 7.5 hours under this creep stress; however, the scatter of data seen in the creep rupture tests indicated that individual specimens could fail between 4 and 13 hours. Specimens were subjected to 0.171 MPa (24.8 psi) for two or four hours. Some were then ramped to failure at a rate of 25.4 mm/min (1.0 in./min) in order to determine the residual strength. Some specimens were given varying durations of time at no stress, and then ramped to failure. Some specimens were given durations of no stress, subjected to 0.171 MPa (24.8 psi) for another two hours, and then ramped to failure. Table A1 presents a summary of these testing parameters and results.

Table A1 Damage and Healing Testing Parameters and Results

Group	Specimen	Stress in MPa (psi)	1st load duration (hours)	Rest period (hours)	2nd load duration (hours)	Residual strength in MPa (psi)	Strain at maximum Load	Average residual strength
A	D-9t	0.171 (24.8)	4			0.467 (67.7)	644%	0.480 (69.6)
	D-22t	0.171 (24.8)	4			0.417 (60.4)	727%	
	D-24t	0.171 (24.8)	4			0.521 (75.6)	568%	
	D-25t	0.171 (24.8)	4			0.514 (74.5)	684%	
B	D-14t	0.171 (24.8)	2	14	2	0.540 (78.3)	598%	0.504 (73.1)
	D-21t	0.171 (24.8)	2	14	2	0.506 (73.3)	775%	
	D-26t	0.171 (24.8)	2	14	2	0.467 (67.7)	677%	
C	D-10t	Immediate Ramp to Failure				0.612 (88.7)	500%	0.633 (91.8)
	D-15t	Immediate Ramp to Failure				0.617 (89.4)	481%	
	D-16t	Immediate Ramp to Failure				0.652 (94.5)	540%	
	D-17t	Immediate Ramp to Failure				0.652 (94.6)	509%	
D	D-7t	0.171 (24.8)	4	14		0.461 (66.9)	612%	
	D-8t	0.171 (24.8)	4	8		0.474 (68.7)	652%	
	D-12t	0.171 (24.8)	2			0.598 (86.7)	542%	
	D-13t	0.171 (24.8)	2	14		0.592 (85.9)	491%	
	D-18t	0.171 (24.8)	2	2	2	0.441 (64.0)	708%	

Group A and group B were subjected to the same duration of loading, although group B was allowed 14 hours of no stress. Group A can also be compared to D-7t and D-8t of group D. In both cases, the inclusion of a recovery period in the middle of the loading period or at the end of the loading period did not significantly increase the residual strength. Group C established the initial strength of a specimen when immediately ramped to failure at 25.4 mm/min (1.0 in./min) and 23°C (73°F). The data does describe a residual strength curve, which is the reduction in residual strength with increasing load time. Points plotted on Fig. A1 describe this residual strength curve and provide a comparison between specimens tested with and without a rest period. If the addition of rest periods had influenced the residual strength, then the specimens with increasingly longer rest periods should have moved up to approach the initial strength line. Fig. A2 provides extension versus time for three representative tests, and Fig. A3, A4, and A5 provide the applied stress versus time for those tests.

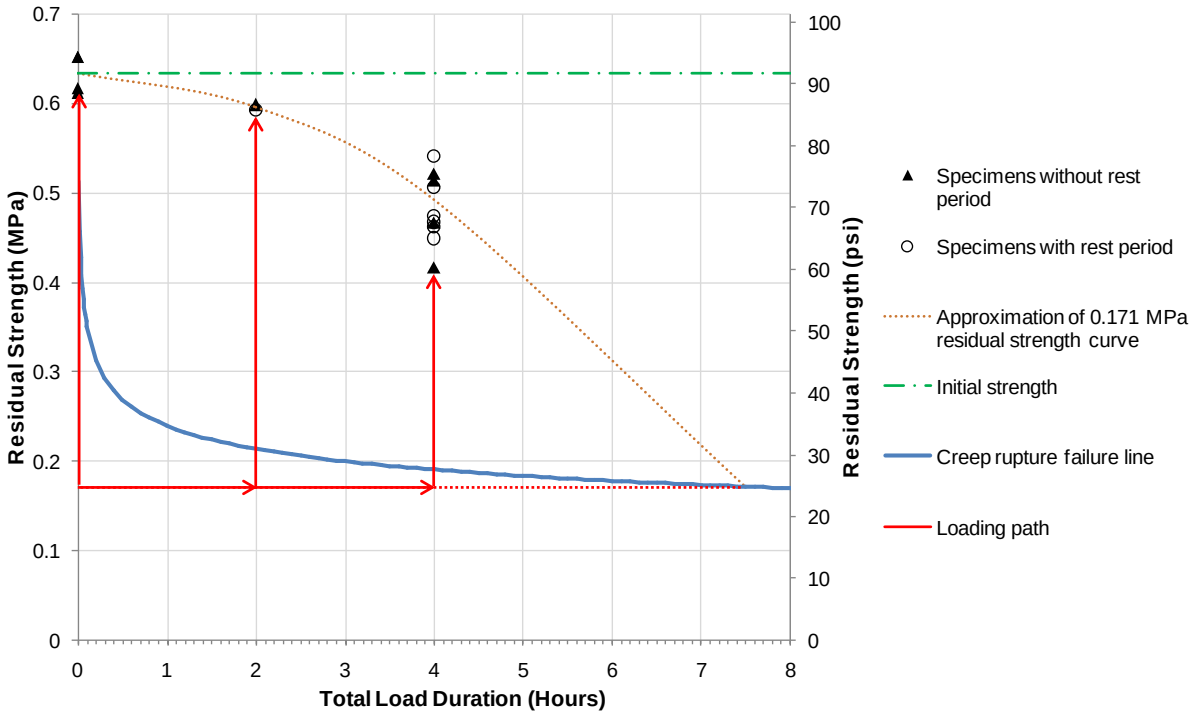

Figure A1 Residual strength curve of tensile VHB tape specimens.

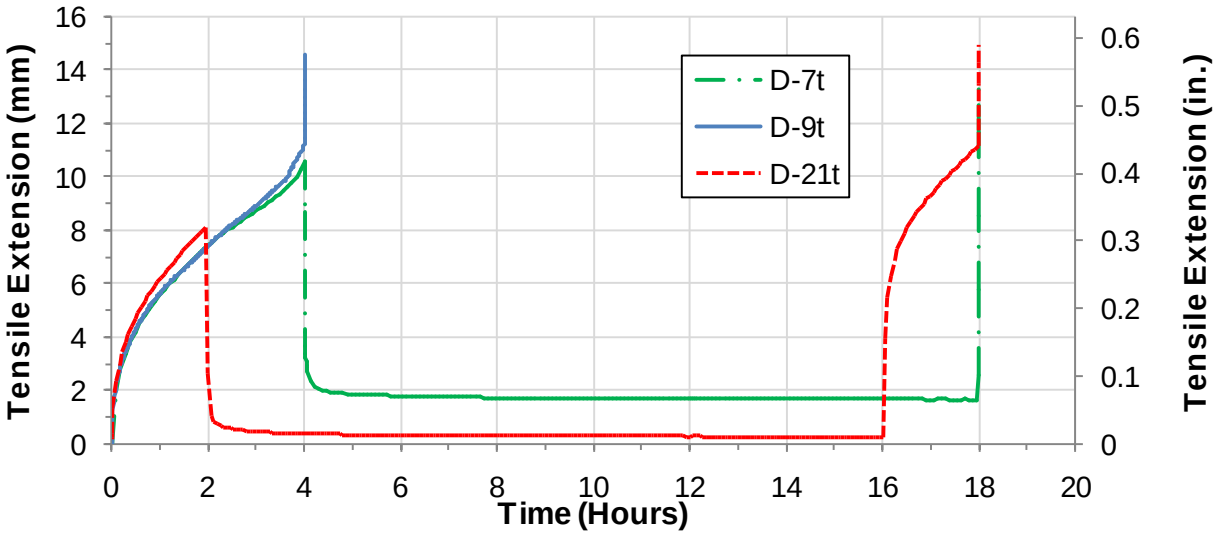

Figure A2 Tensile VHB tape extension of three representative specimens.

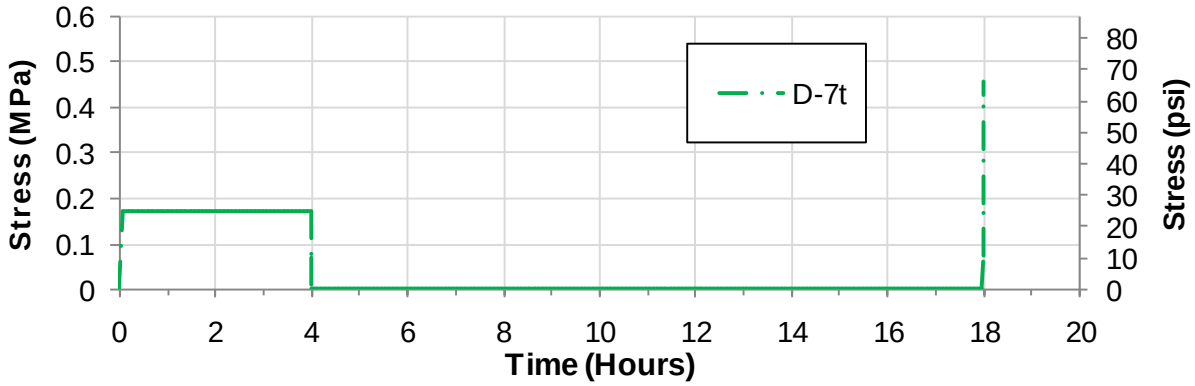

Figure A3 Stress applied to representative specimen D-7t.

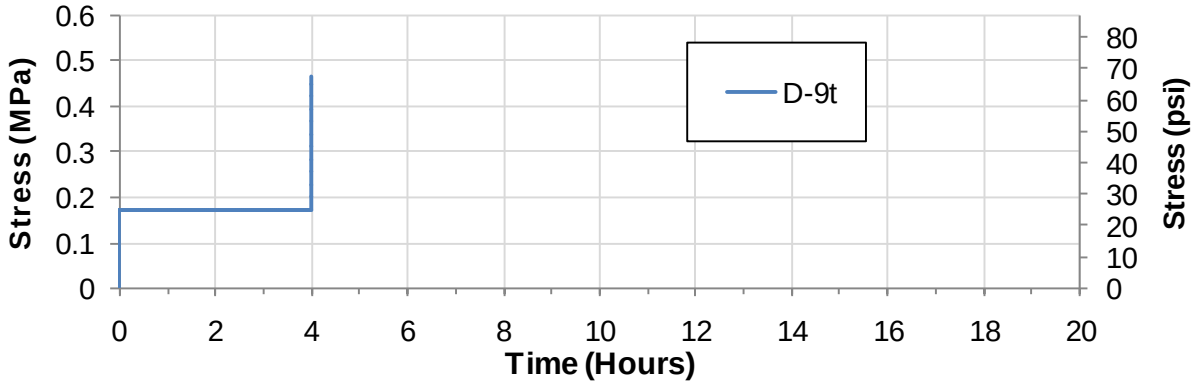

Figure A4 Stress applied to representative specimen D-9t.

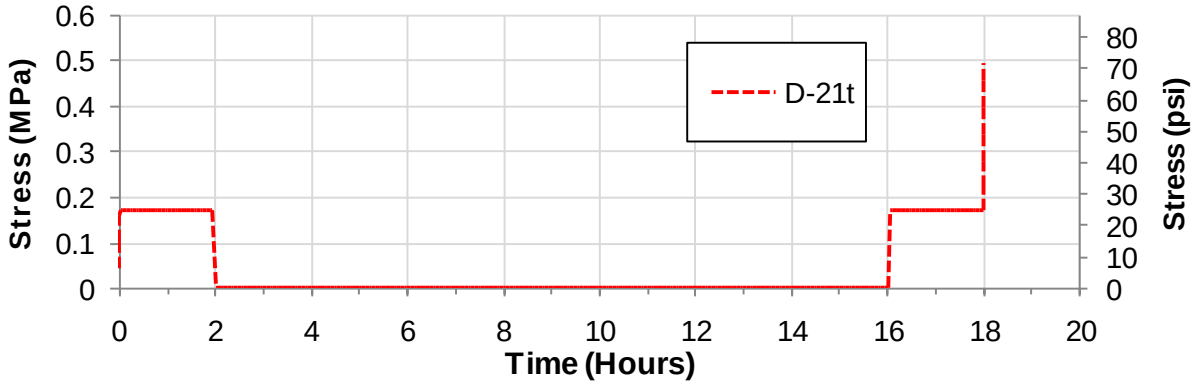

Figure A5 Stress applied to representative specimen D-21t.

The conclusion drawn from this side study was that strength did not noticeably recover with the introduction of rest periods, at least at the creep stresses and durations of load examined. The effect may have been obscured by the scatter of residual strength data, or it may not occur at all

for the testing parameters used in this study. For future work, increasing the number of replicates performed would lessen the interference of scatter. Modifying test parameters such as creep stress, load duration, and rest duration could yield evidence of a healing effect; extending the rest period into days or weeks would seem to be an especially promising research path.

APPENDIX B

FE Inputs

A Prony series expansion was fit to the shear storage modulus (*G'*) 30°C (86°F) reference master curve, shown in Fig. B1. Note that compared to the data presented in the body of the thesis, this *G'* master curve extends about one decade further at the lower end of frequency. This is the result of a supplementary series of shear mode DMA testing performed at higher temperatures to extend the predictive range of the Prony series, and to attempt to establish the equilibrium modulus G_{∞}.

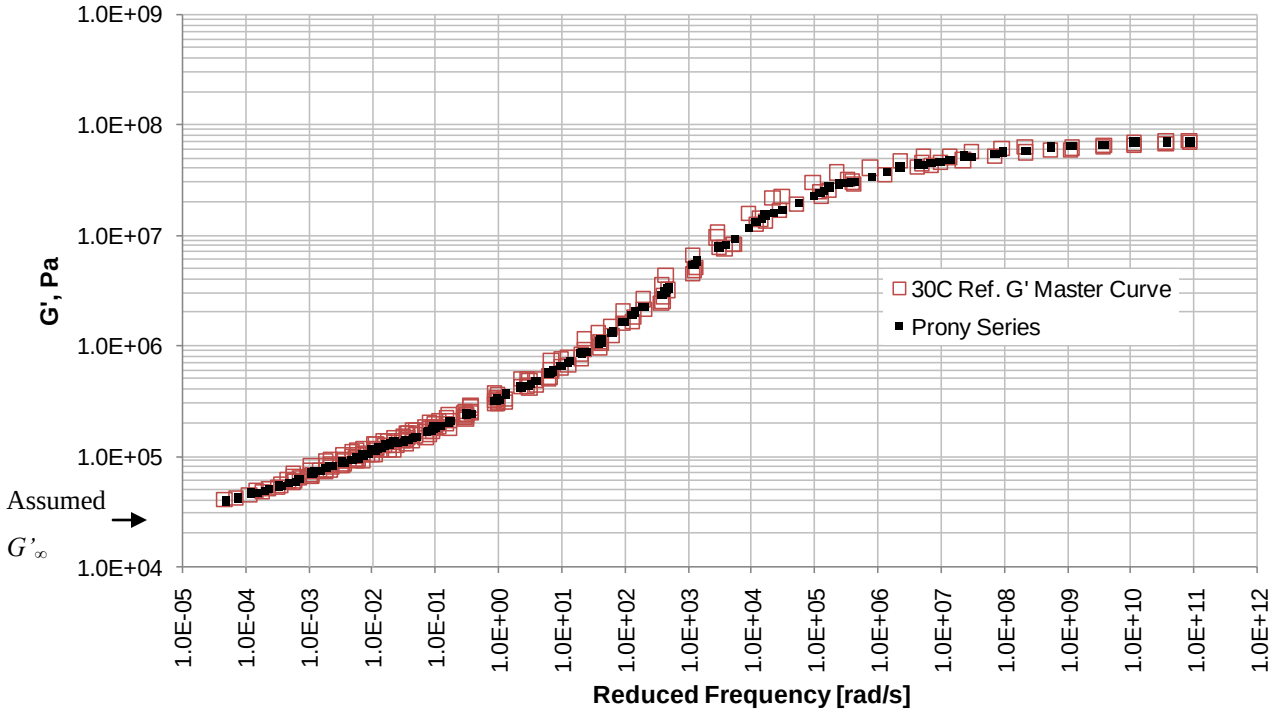

Figure B1 Prony series expansion fit to storage modulus master curve.

Table B1 presents the Prony series terms, with the assumption of $G'_{\infty} = 2.51 \cdot 10^{4}$ Pa. The shear relaxation modulus G_{∞} was assumed to be the same. These Prony series terms are directly fit to the thermally shifted DMA data which extends over a simulated range of frequencies, from $4.7 \cdot 10^{-5}$ rad/s (period of 37 hours) to $8.6 \cdot 10^{10}$ rad/s (period of $7.3 \cdot 10^{-11}$ seconds).

Table B1 Prony Series Expansion Terms

τ_i (sec)	G_i (Pa)	g_i
1.0E-09	7.943E+06	1.160E-01
1.0E-08	7.943E+06	1.160E-01
1.0E-07	1.000E+07	1.461E-01
1.0E-06	1.259E+07	1.839E-01
1.0E-05	1.258E+07	1.837E-01
1.0E-04	9.992E+06	1.460E-01
1.0E-03	4.997E+06	7.300E-02
1.0E-02	1.528E+06	2.232E-02
1.0E-01	4.502E+05	6.576E-03
1.0E+00	2.045E+05	2.988E-03
1.0E+01	9.174E+04	1.340E-03
1.0E+02	5.123E+04	7.484E-04
1.0E+03	3.316E+04	4.844E-04
1.0E+04	1.578E+04	2.306E-04
1.0E+05	1.106E+04	1.615E-04

These terms were generated with shear storage modulus data using the Prony series expansion of Eq. (B1):

$$G'(\omega) = G_\infty + \sum G_i \frac{\omega^2 {\tau_i}^2}{1+\omega^2 {\tau_i}^2} \tag{B1}$$

where ω is the angular frequency (rad/s).

The same G_i and τ_i terms can be applied to produce shear relaxation modulus $G(t)$ using Eq. (B2):

$$G(t) = G_\infty + \sum G_i e^{-t/\tau_i} \tag{B2}$$

Eq. (B3) gives the form of the Prony series expansion for shear relaxation modulus that Abaqus uses to define a viscoelastic material in the time domain:

$$g(t) = 1 - \sum g_i \left(1 - e^{-t/\tau_i}\right) \tag{B3}$$

where g_i is the dimensionless shear modulus ratio:

$$g_i = G_i / G_0 \tag{B4}$$

The instantaneous shear modulus G_0 can be found using Eq. (B5):

$$G_0 = G_\infty + \sum G_i \tag{B5}$$

The Prony series terms in Table B1 were generated using the estimated $G_\infty = 2.51 \cdot 10^4$ Pa, which produces $G_0 = 6.85 \cdot 10^7$ Pa. The accuracy of these terms could be improved with further testing; however, the given G_∞ and G_0 used in conjunction with the terms of Table B1 will provide a good estimate of $G(t)$ for a time period as long as 37 hours. Beyond that time frame, the predicted $G(t)$ may be accurate, but it has not been fit to thermally shifted DMA data. The accuracy of the assumed G_∞ term becomes critical as the time period of loading increases. Note that the given Prony series terms are only accurate for the given values of G_∞ and G_0.

A final assumption required to implement the Prony series expansion in Abaqus is the determination of bulk modulus K. A standard simplifying assumption is to set the $K(t)$ terms to zero, implying no relaxation associated with bulk modulus and a Poisson's ratio equal to 0.5. If Poisson's ratio for VHB tape is known, $K(t)$ can be determined with Eq. (B6):

$$K(t) = G(t)\frac{2 + 2\nu(t)}{3 - 6\nu(t)} \tag{B6}$$

Note that Poisson's ratio $\nu(t)$ will vary weakly with the rate or duration of loading and with temperature.

APPENDIX C

Thermal Expansion

As glazing components are heated and cooled over the diurnal or annual temperature cycle, some components may expand to a greater degree than others, applying shear strain to the VHB tape securing them together. Aluminum, with a coefficient of thermal expansion α of $2.4 \cdot 10^{-5}$ °C^{-1}, will expand more than glass, with α of $9.0 \cdot 10^{-6}$ °C^{-1} (Callister 2003). The critical bond length (l) is the distance from the point where aluminum and glass are fixed in relation to each other to the farthest point where VHB tape secures the two materials together. This value can be normalized by dividing by the thickness of the VHB tape (s), resulting in a geometry factor $\beta = l/s$.

Given geometry factor β, temperature mean, temperature amplitude, baseline temperature when the glazing materials were bonded together, period of temperature cycling (one day or one year), the WLF constants for thermal shift factors, and shear relaxation $G(t)$, then the maximum stress on the VHB tape can be predicted using an algorithm that converts a time history of strain into a time history of stress. A detailed description of this process is presented in the paper by Dillard et al. (2008).

The shear relaxation was developed using a Prony series expansion of $G(t)$ for G23F VHB tape. The method of developing $G(t)$ is described in Appendix B, FE Inputs. This Prony series was fit to DMA data which simulated a loading period as long as 37 hours; beyond that time period, the assumed equilibrium modulus G_∞ = 25 kPa becomes the controlling term for G(t). This means that this analysis of thermal expansion is most accurate for diurnal temperature cycles. For annual cycles, the assumed G_∞ is a dominant term in the Prony series expansion, although some of the terms corresponding to the higher characteristic relaxation times contribute as well.

The following plots and tables were generated using the WLF constants C_1 = 9.98 and C_2 = 132.6, and 25°C as a baseline temperature when the glazing materials were bonded together.

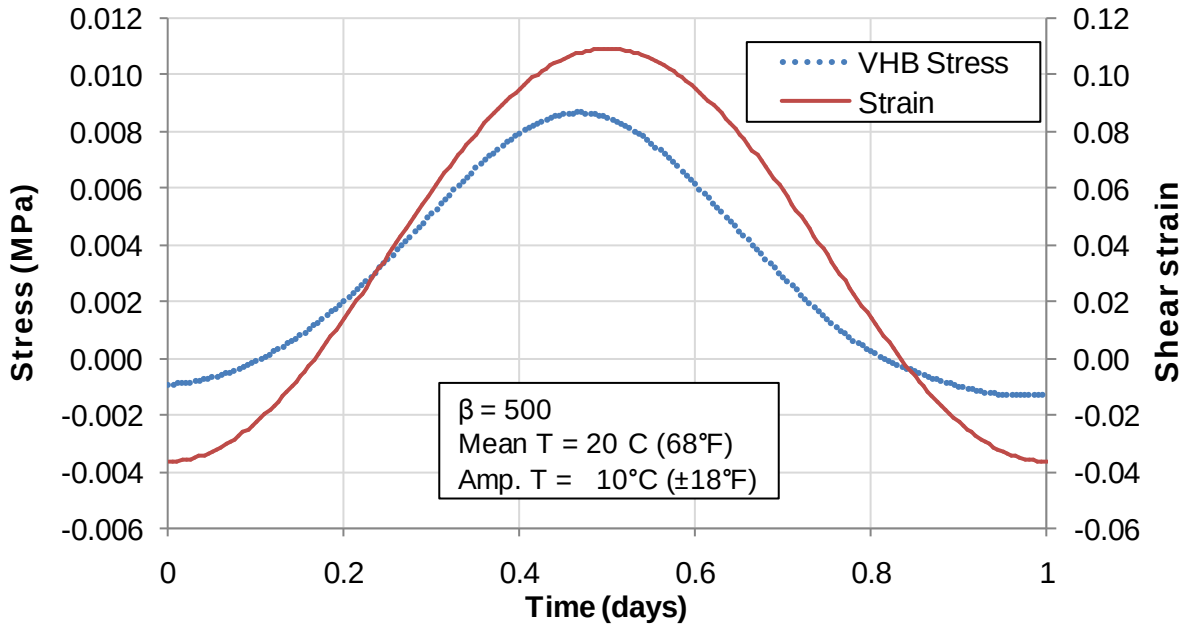

Figure G1 Shear stress from diurnal temperature cycle, β = 500 (2.3 mm tape thickness, 1150 mm bond length).

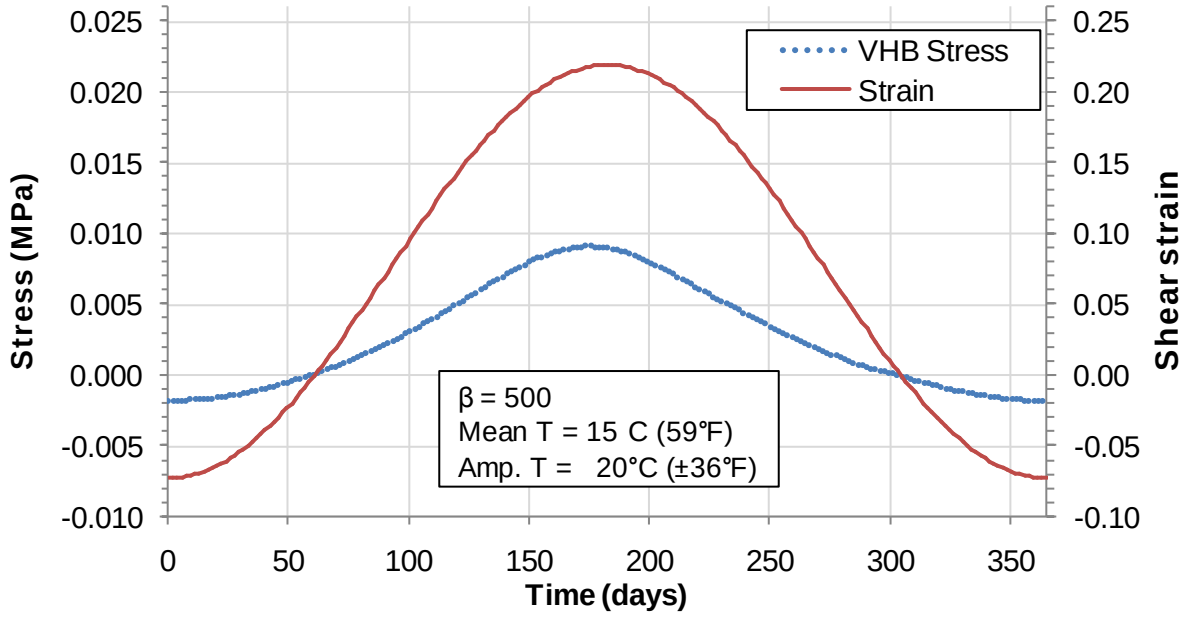

Figure G2 Shear stress from annual temperature cycle, β = 500 (2.3 mm (0.090 in.) tape thickness, 1150 mm (45.3 in.) bond length).

Table G1 Diurnal Cycle Maximum τ (MPa), β = 500 (2.3 mm tape thickness, 1150 mm bond length), Metric Units

Amplitude (°C)	Mean temperature (°C)							
	-10	-5	0	5	10	15	20	25
0	0.0064179	0.005501	0.00458	0.00367	0.002751	0.00183	0.00092	0
2.5	0.0199049	0.013548	0.00991	0.00744	0.005507	0.0039	0.00248	0.00123
5	0.0383279	0.02386	0.01641	0.0119	0.008726	0.00628	0.00428	0.00262
7.5	0.0649841	0.037336	0.02444	0.01718	0.012457	0.00902	0.00634	0.00419
10	0.1068056	0.05584	0.03463	0.02355	0.016809	0.01215	0.00868	0.00598
12.5	0.1767383	0.083185	0.04807	0.03144	0.021956	0.01578	0.01136	0.008
15	0.297937	0.126798	0.06686	0.04156	0.028201	0.02002	0.01443	0.01029
17.5	0.5032222	0.20029	0.09507	0.0551	0.036032	0.02509	0.01799	0.01292
20	0.8343552	0.327183	0.1405	0.07428	0.046183	0.0313	0.02218	0.01595
22.5	1.3294994	0.540539	0.21729	0.10343	0.059927	0.03917	0.02723	0.01947
25	2.0146004	0.881388	0.34942	0.15059	0.079586	0.04943	0.03346	0.02365

Table G2 Annual Cycle Maximum τ (MPa), β = 500 (2.3 mm tape thickness, 1150 mm bond length), Metric Units

Amplitude (°C)	Mean temperature (°C)							
	-10	-5	0	5	10	15	20	25
0	0.0064179	0.005501	0.00458	0.00367	0.002751	0.00183	0.00092	0
2.5	0.0092437	0.007338	0.00583	0.00455	0.003409	0.00235	0.00139	0.00046
5	0.0127643	0.009595	0.00733	0.0056	0.004174	0.00294	0.00188	0.00093
7.5	0.0171484	0.012347	0.00915	0.00684	0.005063	0.00362	0.00243	0.0014
10	0.0227773	0.01572	0.01133	0.00831	0.006096	0.0044	0.00304	0.00192
12.5	0.0304288	0.019962	0.014	0.01008	0.007317	0.0053	0.00374	0.00248
15	0.0415202	0.025517	0.0173	0.01222	0.00878	0.00635	0.00453	0.00311
17.5	0.0590639	0.03321	0.0215	0.01486	0.010552	0.00759	0.00545	0.00382
20	0.0901251	0.044526	0.02708	0.01815	0.012716	0.00908	0.00652	0.00463
22.5	0.1510388	0.062652	0.03489	0.0224	0.015388	0.01088	0.00779	0.00557
25	0.2752313	0.095073	0.04649	0.02809	0.01874	0.01308	0.0093	0.00666

Table G3 Diurnal Cycle Maximum τ/β (MPa), Metric Units

Amplitude	Mean temperature (°C)							
(°C)	-10	-5	0	5	10	15	20	25
0	1.284E-05	1.1E-05	9.2E-06	7.3E-06	5.5E-06	3.7E-06	1.8E-06	0
2.5	3.981E-05	2.71E-05	2E-05	1.5E-05	1.1E-05	7.8E-06	5E-06	2.5E-06
5	7.666E-05	4.77E-05	3.3E-05	2.4E-05	1.75E-05	1.3E-05	8.6E-06	5.2E-06
7.5	0.00013	7.47E-05	4.9E-05	3.4E-05	2.49E-05	1.8E-05	1.3E-05	8.4E-06
10	0.0002136	0.000112	6.9E-05	4.7E-05	3.36E-05	2.4E-05	1.7E-05	1.2E-05
12.5	0.0003535	0.000166	9.6E-05	6.3E-05	4.39E-05	3.2E-05	2.3E-05	1.6E-05
15	0.0005959	0.000254	0.00013	8.3E-05	5.64E-05	4E-05	2.9E-05	2.1E-05
17.5	0.0010064	0.000401	0.00019	0.00011	7.21E-05	5E-05	3.6E-05	2.6E-05
20	0.0016687	0.000654	0.00028	0.00015	9.24E-05	6.3E-05	4.4E-05	3.2E-05
22.5	0.002659	0.001081	0.00043	0.00021	0.00012	7.8E-05	5.4E-05	3.9E-05
25	0.0040292	0.001763	0.0007	0.0003	0.000159	9.9E-05	6.7E-05	4.7E-05

Table G4 Annual Cycle Maximum τ/β (MPa), Metric Units

Amplitude	Mean temperature (°C)							
(°C)	-10	-5	0	5	10	15	20	25
0	1.284E-05	1.1E-05	9.2E-06	7.3E-06	5.5E-06	3.7E-06	1.8E-06	0
2.5	1.849E-05	1.47E-05	1.2E-05	9.1E-06	6.82E-06	4.7E-06	2.8E-06	9.2E-07
5	2.553E-05	1.92E-05	1.5E-05	1.1E-05	8.35E-06	5.9E-06	3.8E-06	1.9E-06
7.5	3.43E-05	2.47E-05	1.8E-05	1.4E-05	1.01E-05	7.2E-06	4.9E-06	2.8E-06
10	4.555E-05	3.14E-05	2.3E-05	1.7E-05	1.22E-05	8.8E-06	6.1E-06	3.8E-06
12.5	6.086E-05	3.99E-05	2.8E-05	2E-05	1.46E-05	1.1E-05	7.5E-06	5E-06
15	8.304E-05	5.1E-05	3.5E-05	2.4E-05	1.76E-05	1.3E-05	9.1E-06	6.2E-06
17.5	0.0001181	6.64E-05	4.3E-05	3E-05	2.11E-05	1.5E-05	1.1E-05	7.6E-06
20	0.0001803	8.91E-05	5.4E-05	3.6E-05	2.54E-05	1.8E-05	1.3E-05	9.3E-06
22.5	0.0003021	0.000125	7E-05	4.5E-05	3.08E-05	2.2E-05	1.6E-05	1.1E-05
25	0.0005505	0.00019	9.3E-05	5.6E-05	3.75E-05	2.6E-05	1.9E-05	1.3E-05

Table G5 Diurnal Cycle Maximum τ (psi), β = 500 (0.090 in. tape thickness, 45.3 in. bond length), English Units

Amplitude (°F)	Mean temperature (°F)							
	14	23	32	41	50	59	68	77
0	0.930591	0.79765	0.664708	0.531766	0.398825	0.265883	0.132942	0
4.5	2.886203	1.964524	1.43695	1.078981	0.798501	0.565585	0.359481	0.177792
9	5.557549	3.459751	2.378766	1.724972	1.265231	0.910932	0.62073	0.379199
13.5	9.422691	5.413687	3.543274	2.491372	1.806242	1.3074	0.919231	0.607638
18	15.48681	8.096785	5.021238	3.4141	2.437261	1.762256	1.259115	0.866438
22.5	25.62705	12.06176	6.969647	4.559016	3.183605	2.287601	1.647308	1.159468
27	43.20087	18.38567	9.694518	6.025596	4.089158	2.903228	2.092087	1.492308
31.5	72.96721	29.04209	13.78451	7.988947	5.224682	3.63799	2.607968	1.873408
36	120.9815	47.4415	20.37244	10.77117	6.696502	4.538818	3.216487	2.312143
40.5	192.7774	78.37814	31.50768	14.99765	8.689395	5.679099	3.948088	2.823475
45	292.1171	127.8012	50.66573	21.83608	11.53997	7.1679	4.851723	3.429745

Table G6 Annual Cycle Maximum τ (psi), β = 500 (0.090 in. tape thickness, 45.3 in. bond length), English Units

Amplitude (°F)	Mean temperature (°F)							
	14	23	32	41	50	59	68	77
0	0.930591	0.79765	0.664708	0.531766	0.398825	0.265883	0.132942	0
4.5	1.340333	1.063961	0.845153	0.660394	0.494278	0.341078	0.201016	0.066711
9	1.850817	1.391312	1.063325	0.812683	0.605282	0.426632	0.272896	0.134154
13.5	2.486512	1.790365	1.32642	0.991977	0.734068	0.524747	0.351854	0.203687
18	3.302707	2.279445	1.643547	1.205227	0.883987	0.637577	0.440716	0.277764
22.5	4.412171	2.894499	2.030126	1.461357	1.060913	0.768081	0.541682	0.359272
27	6.020425	3.699893	2.508141	1.771885	1.27314	0.92013	0.657244	0.450634
31.5	8.564259	4.815437	3.117507	2.154021	1.529996	1.100045	0.790521	0.553994
36	13.06814	6.45623	3.926184	2.632392	1.843877	1.316181	0.945619	0.671963
40.5	21.90062	9.084545	5.059163	3.248618	2.231258	1.577466	1.129046	0.807722
45	39.90855	13.78556	6.741628	4.072929	2.717352	1.896402	1.348989	0.96558

Table G7 Diurnal Cycle Maximum τ/β (psi), English Units

Amplitude	Mean temperature (°F)							
(°F)	14	23	32	41	50	59	68	77
0	0.001861	0.001595	0.001329	0.001064	0.000798	0.000532	0.000266	0
4.5	0.005772	0.003929	0.002874	0.002158	0.001597	0.001131	0.000719	0.000356
9	0.011115	0.00692	0.004758	0.00345	0.00253	0.001822	0.001241	0.000758
13.5	0.018845	0.010827	0.007087	0.004983	0.003612	0.002615	0.001838	0.001215
18	0.030974	0.016194	0.010042	0.006828	0.004875	0.003525	0.002518	0.001733
22.5	0.051254	0.024124	0.013939	0.009118	0.006367	0.004575	0.003295	0.002319
27	0.086402	0.036771	0.019389	0.012051	0.008178	0.005806	0.004184	0.002985
31.5	0.145934	0.058084	0.027569	0.015978	0.010449	0.007276	0.005216	0.003747
36	0.241963	0.094883	0.040745	0.021542	0.013393	0.009078	0.006433	0.004624
40.5	0.385555	0.156756	0.063015	0.029995	0.017379	0.011358	0.007896	0.005647
45	0.584234	0.255602	0.101331	0.043672	0.02308	0.014336	0.009703	0.006859

Table G8 Annual Cycle Maximum τ/β (psi), English Units

Amplitude	Mean temperature (°F)							
(°F)	14	23	32	41	50	59	68	77
0	0.001861	0.001595	0.001329	0.001064	0.000798	0.000532	0.000266	0
4.5	0.002681	0.002128	0.00169	0.001321	0.000989	0.000682	0.000402	0.000133
9	0.003702	0.002783	0.002127	0.001625	0.001211	0.000853	0.000546	0.000268
13.5	0.004973	0.003581	0.002653	0.001984	0.001468	0.001049	0.000704	0.000407
18	0.006605	0.004559	0.003287	0.00241	0.001768	0.001275	0.000881	0.000556
22.5	0.008824	0.005789	0.00406	0.002923	0.002122	0.001536	0.001083	0.000719
27	0.012041	0.0074	0.005016	0.003544	0.002546	0.00184	0.001314	0.000901
31.5	0.017129	0.009631	0.006235	0.004308	0.00306	0.0022	0.001581	0.001108
36	0.026136	0.012912	0.007852	0.005265	0.003688	0.002632	0.001891	0.001344
40.5	0.043801	0.018169	0.010118	0.006497	0.004463	0.003155	0.002258	0.001615
45	0.079817	0.027571	0.013483	0.008146	0.005435	0.003793	0.002698	0.001931

Appendix C References

Callister, W. D. (2003). Materials Science and Engineering - An Introduction. New York, John Wiley & Sons.

Dillard, D., L. Yan, et al. (2008). "On estimating the stresses in linear viscoelastic sealants subjected to thermally-driven deformations." In preparation for The Journal of Adhesion.

APPENDIX D

Operating Manual for 72 Station Pneumatic Creep Rupture Test Frame

Calibration Procedure

Load Cell Transducers:

- Set the gain on the gauge amplifiers to 2.0.
- Remove load cells, adjust gauge amplifier balance to zero output. Lock down the gauge amplifier dials.
- Open "Calibrate Load Cell USB.vi" in "72Station Tensile Tester" folder.
- The voltages should be nearly zero. If not, readjust gauge amplifier balance. Make sure there is no load on the load cells. Set actual load to zero, click "Save This Calibration Point."
- Place ~50 lb of weights on a weight tray and attach to the load cell. Use the weights and weight tray which have their weights written on them. Enter the exact weight applied to the load cell, and click "Save this Calibration Point."
- Write down the slope and intercept, and repeat procedure with the other load cell. These values must be entered into the LabVIEW T72 Tester Main.vi programming manually, by opening the DAQ Assistent4 block in the block diagram window.

Thermocouples:

- Freeze a cup of water.
- Drill a small hole into the ice, fill the hole with water, and insert a thermocouple tip into the hole.
- Open "Calibrate Thermocouple USB.vi." Figure out which channel you want to calibrate (0 or 1), click "Begin Calibrating this Channel," and set actual temperature to 0°C. Wait for the reading to steady, and click "Save this Calibration Point."
- Carefully set a hotplate inside the test chamber, and bring a glass of water to boil. Insert the tip of the thermocouple into the boiling water and save the 100°C calibration point.
- Click "Save Calibration Curve." This will generate a file which the T72 Tester Main.vi will automatically load when the program is started.

Controlling Temperature

The cylinders are sensitive to temperature variations, and the load applied will decrease slightly if the cylinders are heated. For ambient temperature tests, the AC/heater unit can be run to

stabilize room temperature. For elevated temperature tests, heat will conduct up the cylinder piston rods and heat the cylinders. Because this does not occur for the indicator cylinders, this can introduce error in the load record. At test temperatures above 40°C, use fans mounted overhead to cool the cylinders. Do not run the AC unit to cool the room. The AC blows cold air in a cyclic pattern which will result in a cyclic pattern of loading on the specimens in the chamber.

Controlling Humidity

At elevated temperatures, the RH in the chamber is roughly 15%. To standardize this variable for all tests, use about 8 oz. of Drierite® during ambient temperature tests. Drierite® will bring the RH down to roughly 15%. Make sure all of the holes in the bottom of the chamber are filled with bolts, or plugged by other means.

Test Run Procedure

1. If the cylinders have not been oiled recently, place ten drops of air compressor oil into the two outlet valves at the top of the test frame. Bring the pressure up to about 50 psi on both sides, and then cycle the load between tension and compression so that the cylinder pistons move up and down. Cycle the pistons about ten times. Make sure the pistons will not collide with anything inside the test chamber.
2. If the test is at elevated temperature, it is best to set the heater running about six hours before using the test frame, in order to heat up all the metal parts.
    a. Turn on the power strip that runs the heater.
    b. The heater is controlled with the two temperature control panels on the right side of the humidity/temperature control board. The other control panels are used for humidity control.
    c. Set the dial gauge on the lower right to 100°C and press "reset." This limits the test frame to 100°C before it shuts down the heater.
    d. On the upper right control panel, press "index" so that the display reads "SP1." Use the arrow keys to set the temperature and press "enter." Press "index" again, and when the display reads "SP2" set that to the same temperature and press "enter." Note that these heater control temperatures do not correspond to real temperatures in the test chamber, as indicated by the thermocouples which the LabVIEW program utilizes. This means setting the heater temperature to get the desired temperature requires some experimentation. For example, when the heater control temperature is set to 41.6°C, the test chamber is actually 40.0°C.

3. Set the two pressure regulators to the loads which the tests will be run at, wait 15 minutes, and then adjust the load again. The loads usually drop by ½ lb in the first 15 minutes.
4. After loads are set, shut off the supply of air by closing the red-handled cutoff valve at the base of the test frame.
5. Discharge the air pressure by opening the two outlet valves at the top of the frame. Close the outlet valves again.
6. Insert specimens. Taking a photograph now is a good idea for future reference. Record the position number of each specimen. The LabVIEW output file labels specimen positions as F1 to F36, and B1 to B36.
7. Wait for the chamber and specimens to heat up, if applicable.
8. Under the "Settings" tab, enter the desired data recording interval. It is usually best to start with a small interval to record specimens that fail in a short time period, and then change it to a larger interval after a few minutes or hours. The interval can be safely changed while data is being collected.
9. Enter the group number (1 to 12) of each specimen in the "Settings" tab. Failure times will be displayed by group number in the lower left plot of the "Monitor" tab.
10. Make sure the upper outlet valves are closed, click "Log Data", and name the file. After the file is saved the data collection will start. Open up the cutoff valve. The pressure regulators should already be set at the correct load.
11. When the test is finished, click "Logging Data" to stop the recording. Use the USB ports inside the grey data acquisition box to download data.

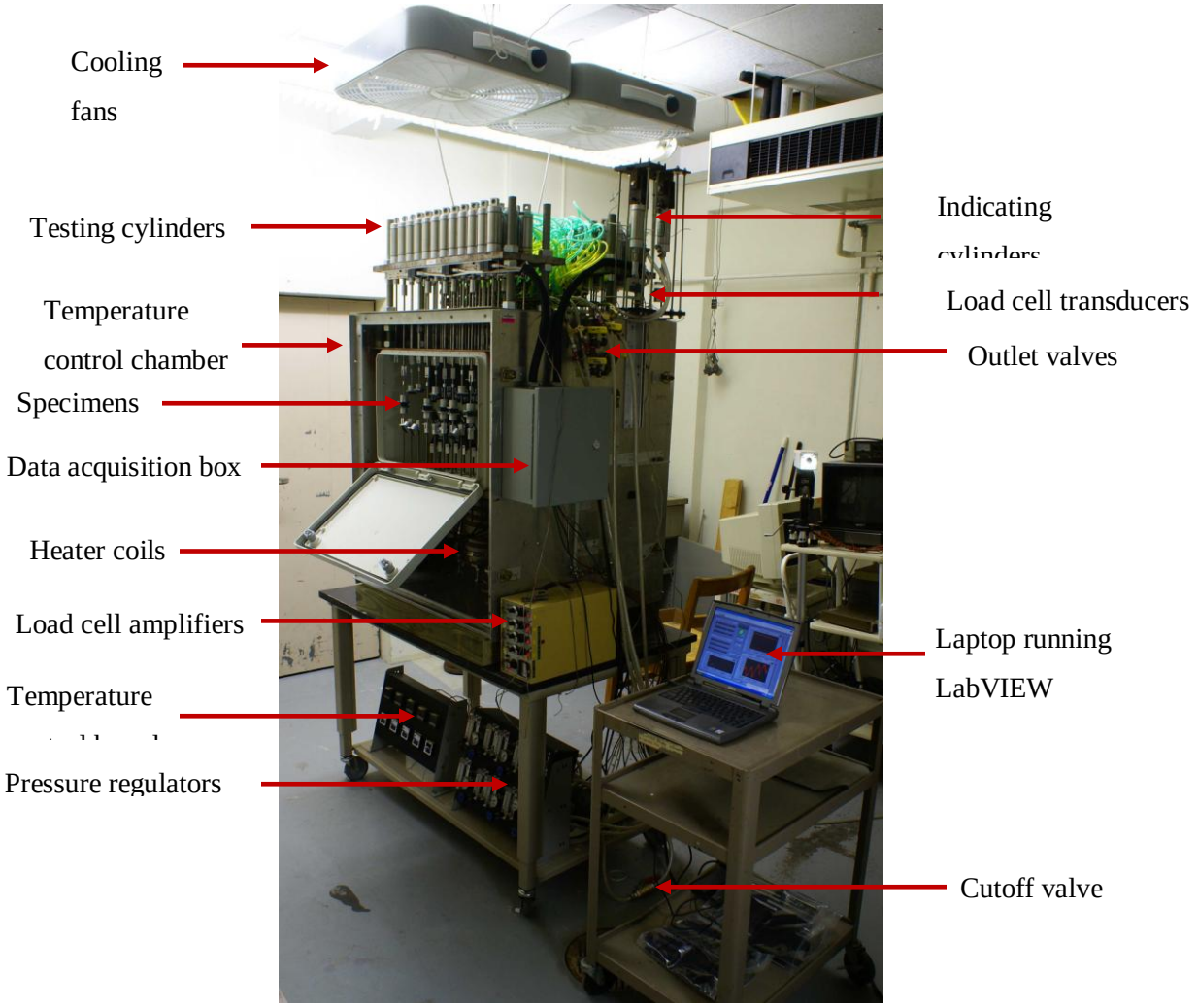

Figure D1 72-station test frame with front face of temperature control chamber removed.

APPENDIX E

Supplementary DMA Data

Table E1 presents estimations of T_g using all three DMA geometries. A value is marked "ambiguous" if the two replicates did not agree, or if data was missing at the apparent T_g and the value had to be estimated.

Table E1 Supplementary T_g Estimates

Loading frequency	Test geometry	Estimation method	T_g estimate (°C)	Ambiguous?
1 Hz	Shear	Peak loss modulus	-12	
		Peak tan δ	12	
	Compression	Peak loss modulus	-3	y
		Peak tan δ	3	y
	Long axis tension	Peak loss modulus	-4	
		Peak tan δ	20	
75 Hz	Shear	Peak loss modulus	4	
		Peak tan δ	37	
	Compression	Peak loss modulus	17	y
		Peak tan δ	25	y
	Long axis tension	Peak loss modulus	11	y
		Peak tan δ	47	

The following figures, E1 through E12, show DMA generated loss modulus, storage modulus, and tangent delta for all three geometries. Note that only the first replicate is shown for figures E7 through E12, and the Tg estimates of Table E1 were taken from the average of both replicates.

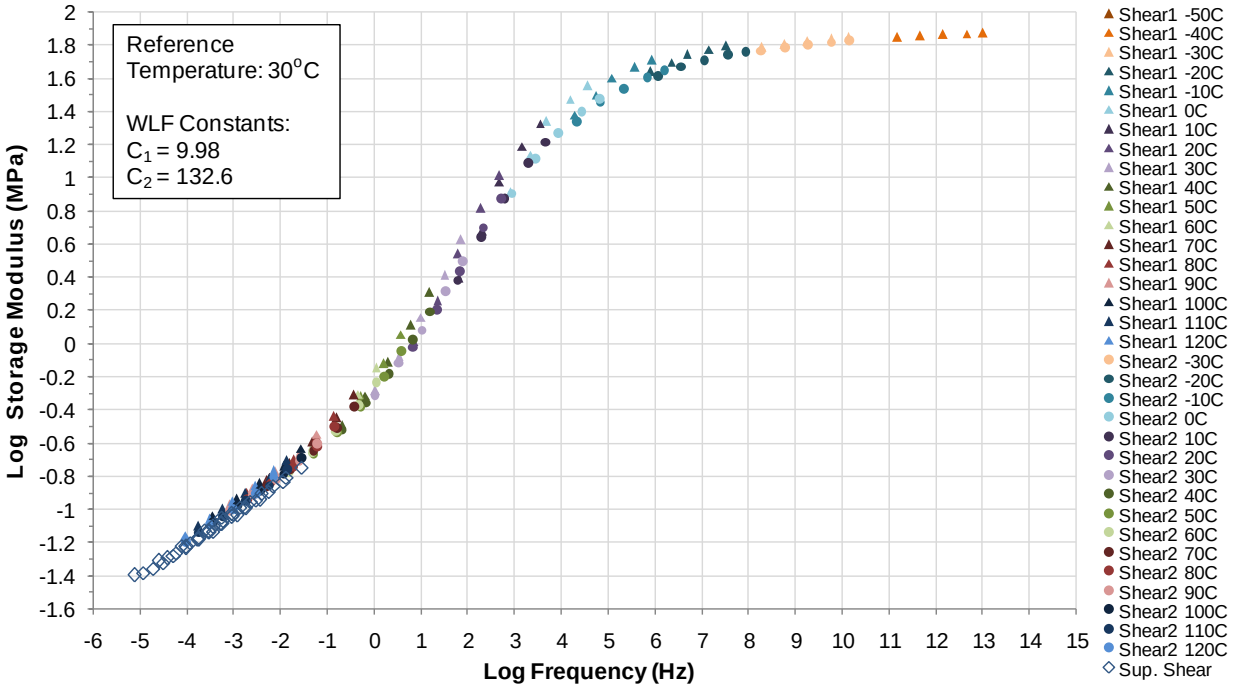

Figure E1 Shear geometry G23F storage modulus master curve.

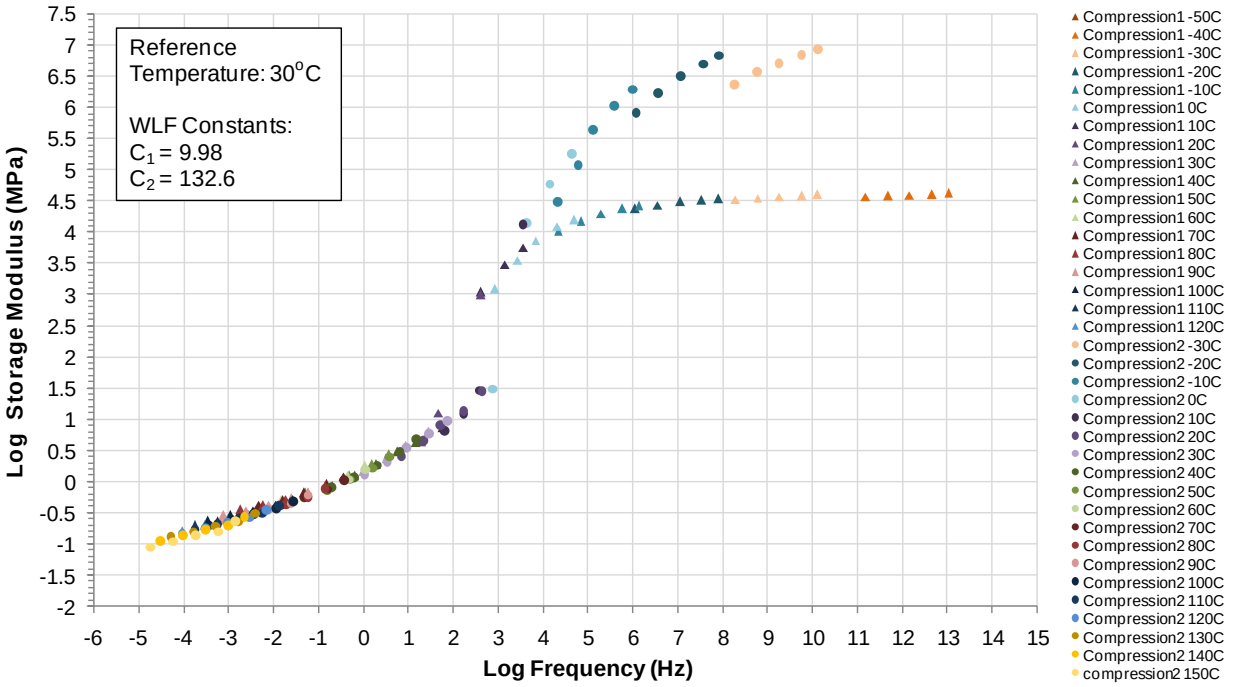

Figure E2 Compression geometry G23F storage modulus master curve – data above 10^3 Hz is erroneous.

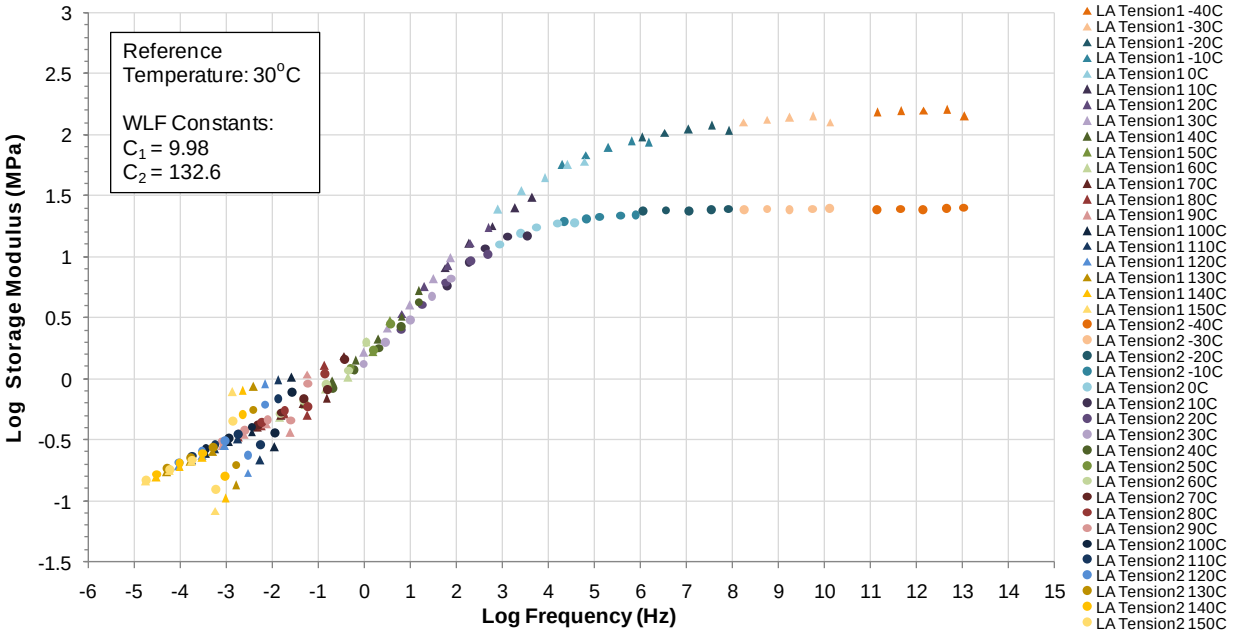

Figure E3 Long Axis tension geometry G23F storage modulus master curve – 1st replicate is likely erroneous.

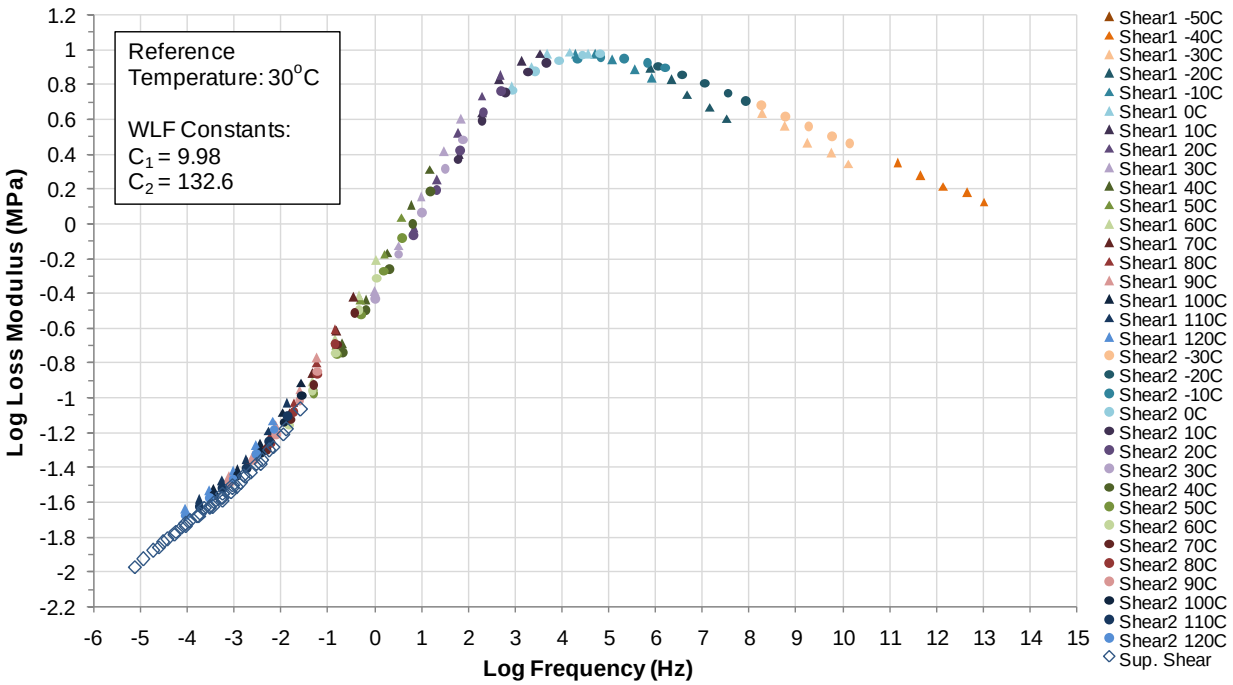

Figure E4 Shear geometry G23F loss modulus master curve.

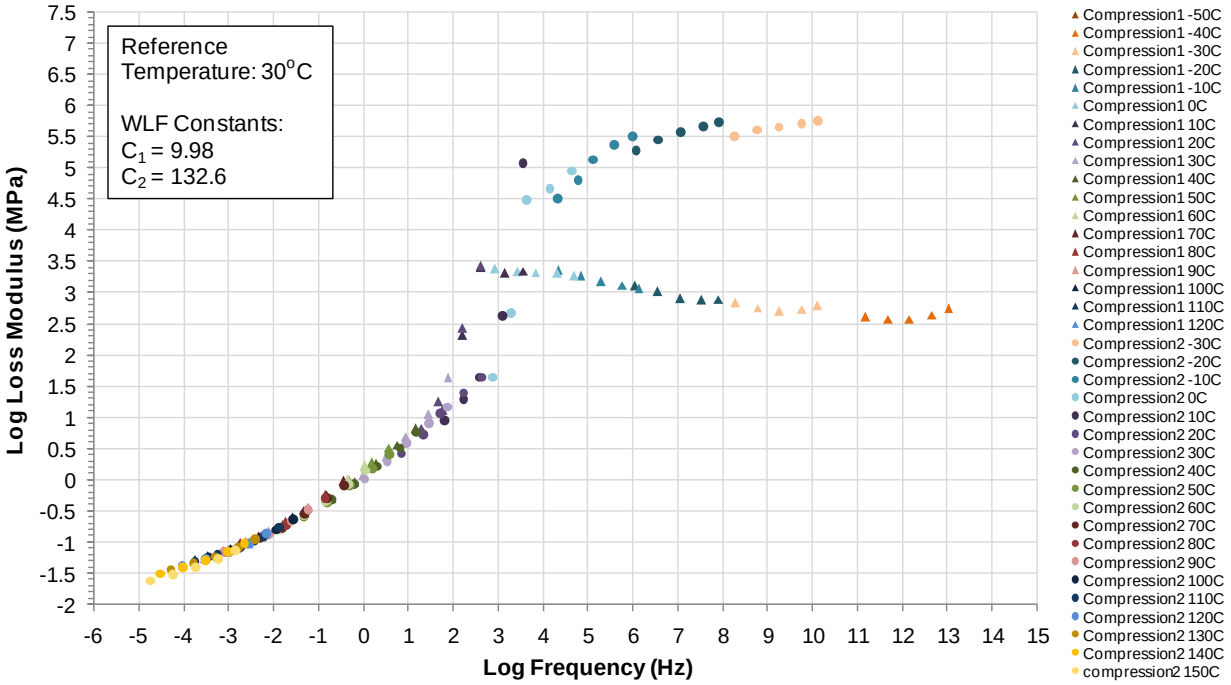

Figure E5 Compression geometry G23F loss modulus master curve – data above 10^3 Hz is erroneous.

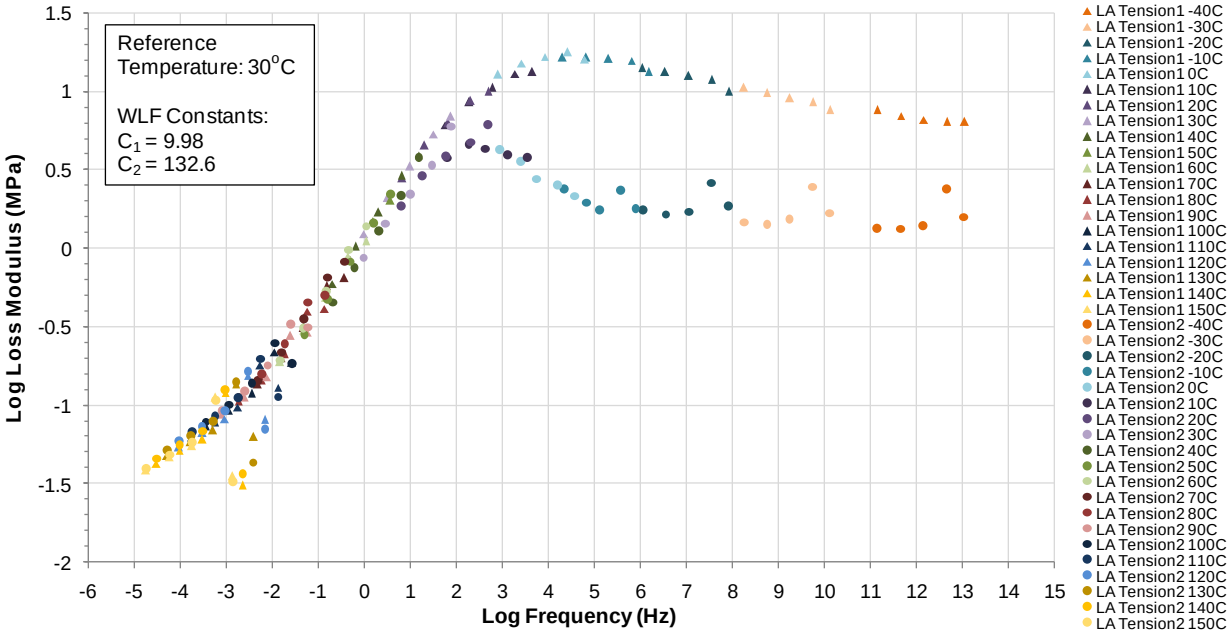

Figure E6 Long Axis tension geometry G23F loss modulus master curve – 1st replicate is likely erroneous.

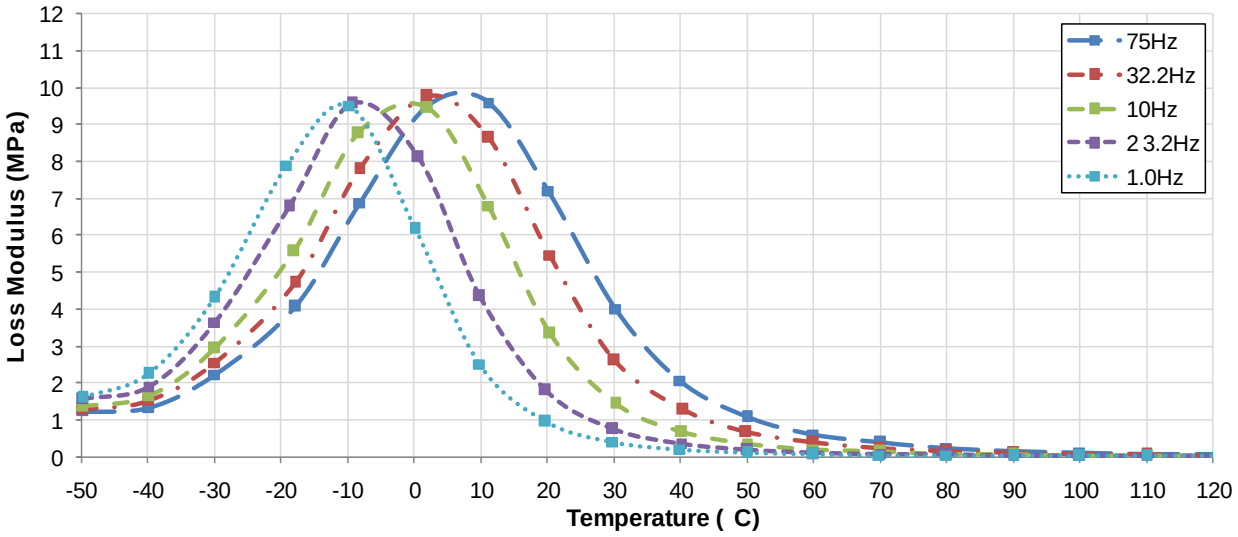

Figure E7 Loss modulus as a function of time from the first shear geometry replicate.

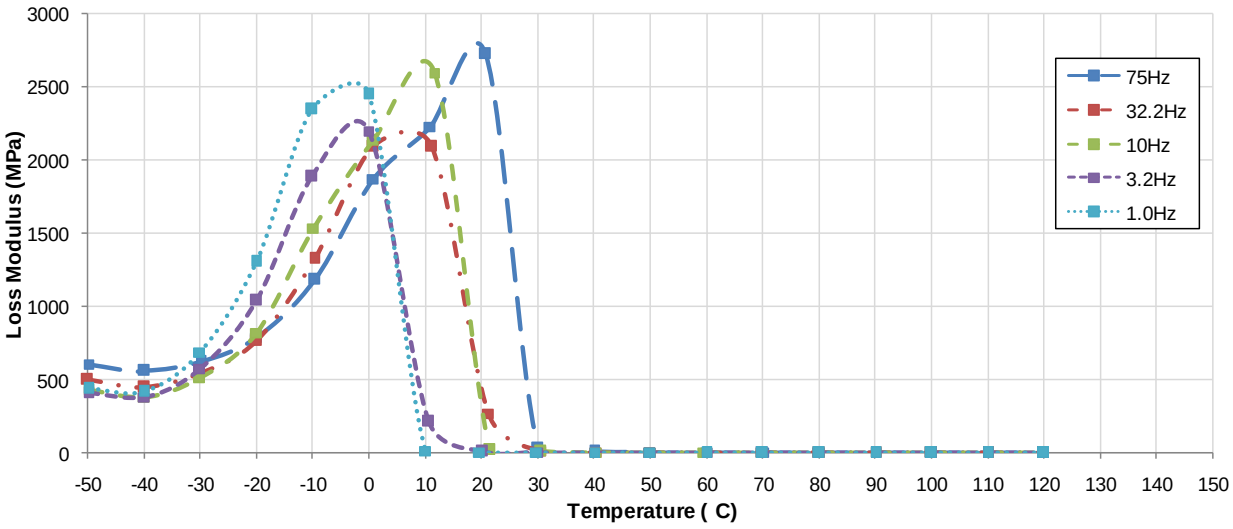

Figure E8 Loss modulus as a function of time from the first compression geometry replicate – these values are likely erroneous.

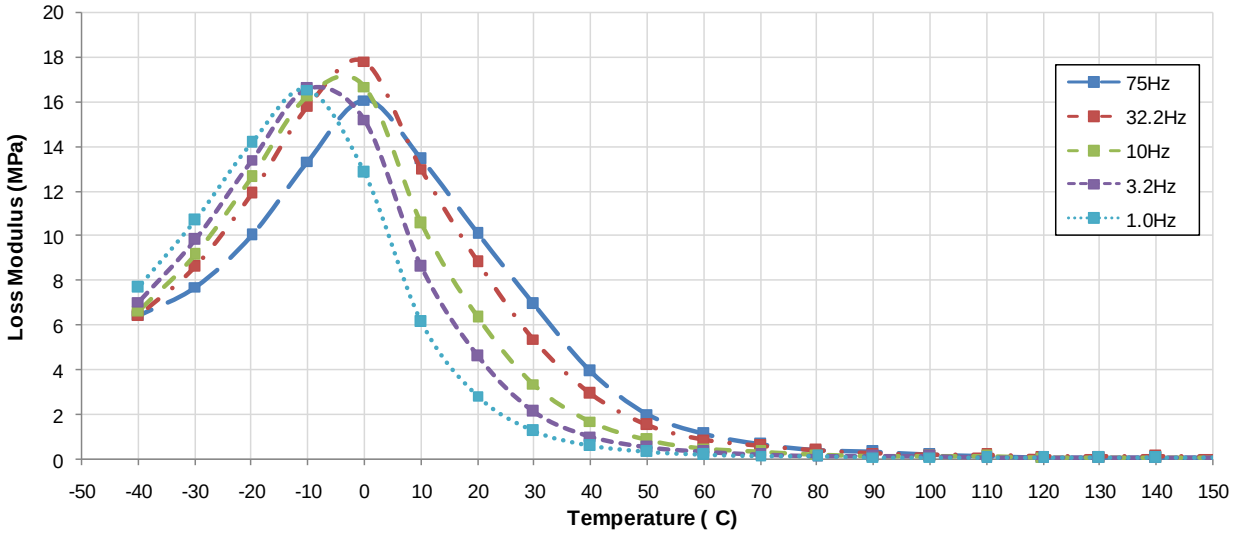

Figure E9 Loss modulus as a function of time from the first long axis tension geometry replicate – these values are likely erroneous.

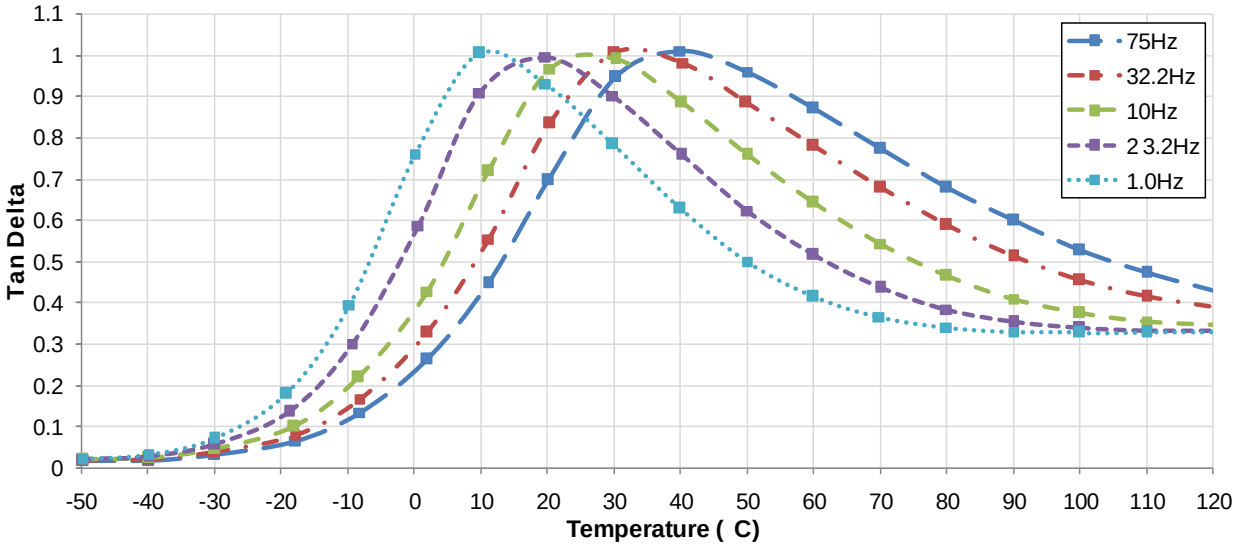

Figure E10 Tangent delta as a function of time from the first shear geometry replicate.

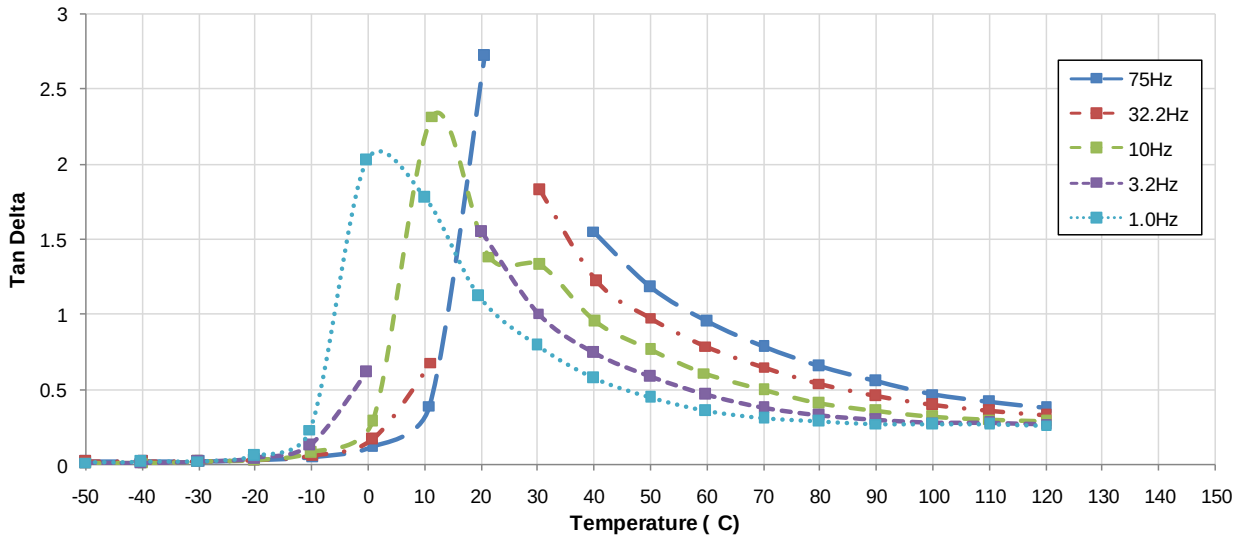

Figure E11 Tangent delta as a function of time from the first compression geometry replicate.

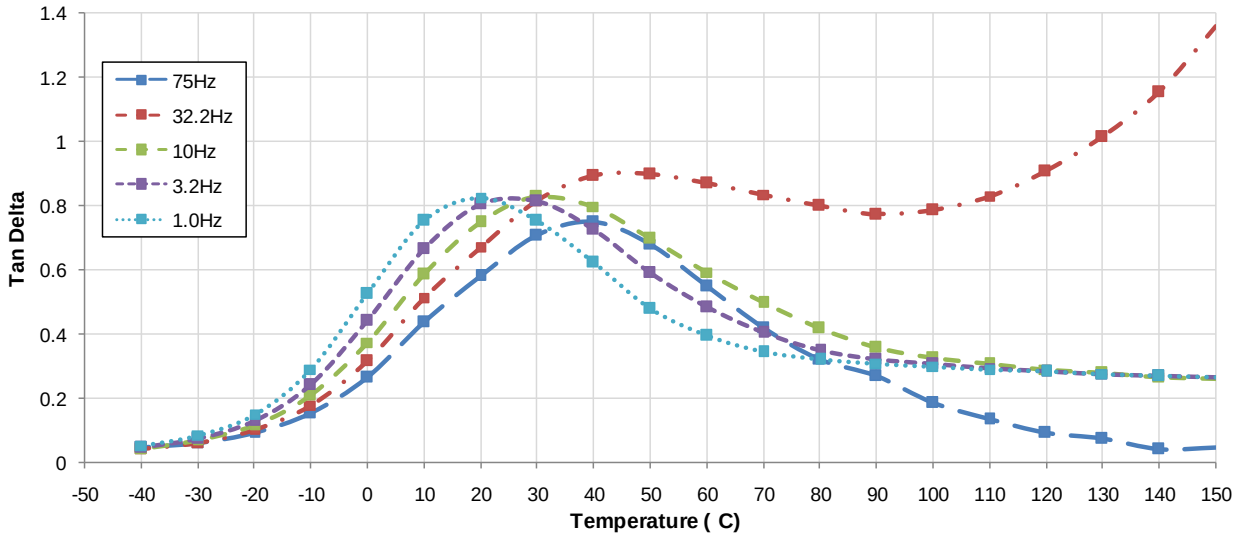

Figure E12 Tangent delta as a function of time from the first long axis tension geometry replicate.

APPENDIX F

Teflon Jig

The casting and curing of the shear and tensile silicone specimens was performed by 3M using the Teflon jig shown in Fig. F1. The jig was designed by 3M so that when the anodized aluminum adherends were slotted in place, they formed a cavity 0.25 in. by 0.25 in. by 1.33 in. (6.4mm by 6.4 mm by 33.9 mm).

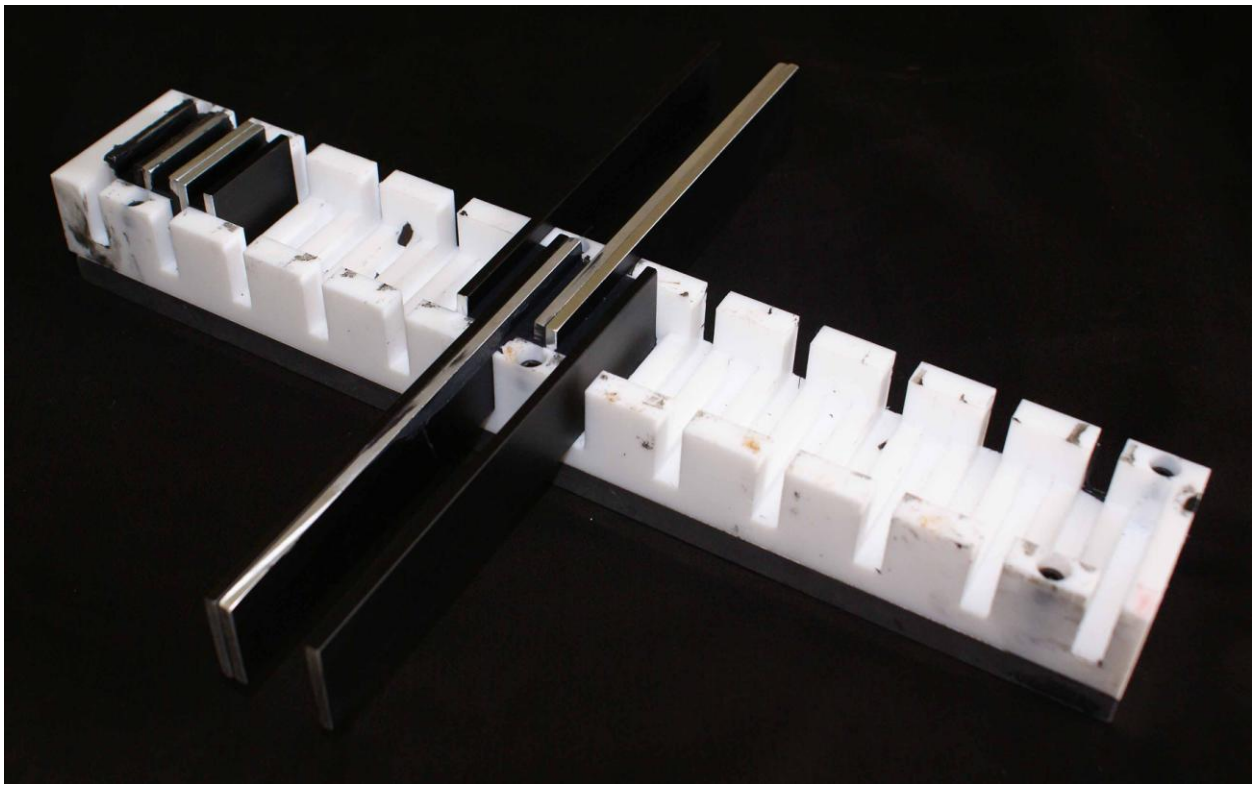

Figure F1 Teflon jig for casting silicone specimens.

APPENDIX G

Bending Jig

The s-bend applied to the silicone single lap shear adherends was formed with a bending jig and a vise, as shown in the following figures.

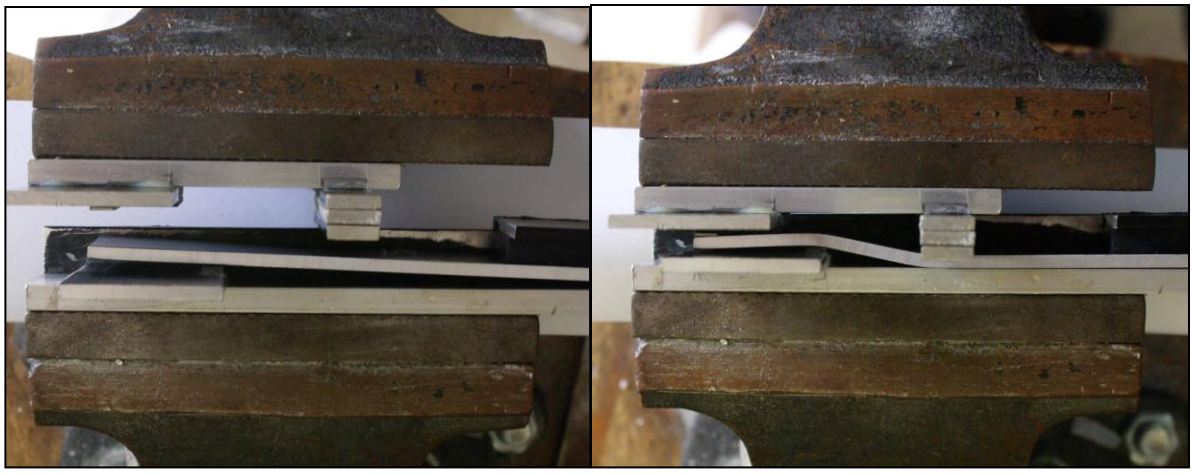

Figure G1 Single-lap shear adherend in bending jig a) before bending and b) during bending.

Figure G2 Single-lap shear adherend after bending.

APPENDIX H

Tabulated RTF Data

Table H1 Tensile VHB Tape Ramp-to-Fail Data

Loading rate (mm/min)	Temperature (°C)	Replicate	Ultimate strength (MPa)	Elongation at ultimate strength (mm)	Strain at ultimate strength	Average ultimate strength (MPa)
5	23	1	0.365	14.97	651%	0.382
		2	0.384	14.63	636%	
		3	0.398	14.66	637%	
	40	1	0.267	16.01	696%	0.265
		2	0.259	12.87	560%	
		3	0.271	13.18	573%	
	60	1	0.201	15.69	682%	0.201
		2	0.200	13.92	605%	
		3	0.203	14.35	624%	
50	23	1	0.616	12.01	522%	0.617
		2	0.618	12.19	530%	
		3	0.616	12.14	528%	
	40	1	0.390	14.51	631%	0.387
		2	0.380	12.92	562%	
		3	0.390	13.32	579%	
	60	1	0.275	13.6	591%	0.276
		2	0.278	13.84	602%	
		3	0.275	12.94	563%	
500	23	1	1.135	8.61	374%	1.092
		2	1.057	7.9	343%	
		3	1.084	8.39	365%	
	40	1	0.641	11.26	490%	0.638
		2	0.625	11.34	493%	
		3	0.647	11.54	502%	
	60	1	0.411	12.72	553%	0.407
		2	0.408	12.41	540%	
		3	0.401	13.46	585%	

Table H2 Shear VHB Tape Ramp-to-Fail Data

Loading rate (mm/min)	Silicone	Replicate	Ultimate strength (MPa)	Elongation at ultimate strength (mm)	Strain at ultimate strength	Average ultimate strength (MPa)
5	S1	1	0.755	6.12	96%	0.874
		2	0.883	18.02	284%	
		3	0.985	15.35	242%	
	S2	1	1.359	7.05	111%	1.403
		2	1.426	6.56	103%	
		3	1.423	7.59	120%	
	S3	1	0.381	6.5	102%	0.455
		2	0.515	9.35	147%	
		3	0.467	6.39	101%	
50	S1	1	1.310	14.53	229%	1.313
		2	1.325	13.65	215%	
		3	1.305	13.27	209%	
	S2	1	1.464	7.18	113%	1.479
		2	1.481	6.56	103%	
		3	1.491	7.23	114%	
	S3	1	0.586	6.91	109%	0.588
		2	0.571	7.4	117%	
		3	0.608	7.98	126%	
500	S1	1	1.338	14.05	221%	1.383
		2	1.378	14.81	233%	
		3	1.432	14.34	226%	
	S2	1	1.650	6.5	102%	1.647
		2	1.621	6.7	106%	
		3	1.669	6.43	101%	
	S3	1	0.786	9.48	149%	0.738
		2	0.686	6.49	102%	
		3	0.743	6.16	97%	

Table H3 Tensile Silicone Sealant Ramp-to-Fail Data

Loading rate (mm/min)	Silicone	Replicate	Ultimate strength (MPa)	Elongation at ultimate strength (mm)	Strain at ultimate strength	Average ultimate strength (MPa)
5	S1	1	0.755	6.12	96%	0.874
		2	0.883	18.02	284%	
		3	0.985	15.35	242%	
	S2	1	1.359	7.05	111%	1.403
		2	1.426	6.56	103%	
		3	1.423	7.59	120%	
	S3	1	0.381	6.5	102%	0.455
		2	0.515	9.35	147%	
		3	0.467	6.39	101%	
50	S1	1	1.310	14.53	229%	1.313
		2	1.325	13.65	215%	
		3	1.305	13.27	209%	
	S2	1	1.464	7.18	113%	1.479
		2	1.481	6.56	103%	
		3	1.491	7.23	114%	
	S3	1	0.586	6.91	109%	0.588
		2	0.571	7.4	117%	
		3	0.608	7.98	126%	
500	S1	1	1.338	14.05	221%	1.383
		2	1.378	14.81	233%	
		3	1.432	14.34	226%	
	S2	1	1.650	6.5	102%	1.647
		2	1.621	6.7	106%	
		3	1.669	6.43	101%	
	S3	1	0.786	9.48	149%	0.738
		2	0.686	6.49	102%	
		3	0.743	6.16	97%	

Table H4 Shear Silicone Sealant Ramp-to-Fail Data

Loading rate (mm/min)	Temperature (°C)	Replicate	Ultimate strength (MPa)	Elongation at ultimate strength (mm)	Strain at ultimate strength	Average ultimate strength (MPa)
5	S1	1	0.815	14.77	233%	0.915
		2	0.976	16.46	259%	
		3	0.955	16.04	253%	
	S2	1	0.906	10.38	163%	1.037
		2	1.085	11.54	182%	
		3	1.121	11.29	178%	
	S3	1	0.612	20.4	321%	0.568
		2	0.596	17.87	281%	
		3	0.495	14.95	235%	
50	S1	1	1.234	19.13	301%	1.159
		2	1.082	16.6	261%	
		3	1.161	17.23	271%	
	S2	1	1.200	10.9	172%	1.338
		2	1.445	14.85	234%	
		3	1.369	15.22	240%	
	S3	1	0.763	19.4	306%	0.774
		2	0.759	18.38	289%	
		3	0.801	20.16	317%	
500	S1	1	1.279	17.67	278%	1.322
		2	1.320	19.14	301%	
		3	1.368	18.27	288%	
	S2	1	1.519	12.55	198%	1.538
		2	1.605	13.29	209%	
		3	1.492	12.21	192%	
	S3	1	0.846	16.3	257%	0.866
		2	0.905	18.72	295%	
		3	0.849	16.62	262%	

APPENDIX I

Moisture Uptake Side Study

A side study was performed to investigate the rate of diffusion of moisture into VHB tape specimens. This study was necessary to determine if VHB tape specimens could be exposed briefly to ambient relative humidity without absorbing a significant degree of moisture. Ramp-to-fail, creep rupture, and DMA specimens were stored in containers that were maintained at low humidity (15 to 25% RH), but needed to be exposed to ambient RH as high as 85% while they were being prepared for testing. Additionally, the ramp-to-fail and DMA testing processes did not control humidity, although these tests required less than three hours to perform. The creep rupture testing, which could last as long as several weeks, was humidity controlled with a desiccant. The question addressed by this side study was whether three hours of exposure to high humidity would result in a significant increase in specimen moisture mass.

Two VHB tapes were used for this side study. The first was 12.7 mm (0.50 in.) wide, 2.3 mm (0.090 in.) thick 4991 VHB tape. The second was 25.4 mm (1.00 in.) wide, 1.0 mm (0.041 in.) thick 4941 VHB tape. Each specimen was 127 mm (5.00 in.) long. Some specimens had one flat face sealed with steel foil, some specimens had both flat faces sealed, and some specimens had no faces sealed. The 4991 tape had two replicates per condition set, and the 4941 tape had one replicate, for a total of nine specimens tested. Note that the specimens that most resembled those used for ramp-to-fail, creep rupture, and DMA testing were the 4991 VHB tape specimens with steel foil sealing both flat faces. G23F VHB tape was not immediately available at the time of this side study.

The specimens were dried to constant mass for seven days at 90°C (194°F), and then placed in a sealed chamber with standing water, providing nearly 100% RH conditions. Fig. I1 provides the resulting increase in percent moisture (moisture mass / dry specimen mass) over several weeks. Fig. I2 shows only the specimens that had foil applied to both flat faces, for the first two days of testing. Tabulated data is provided in Table I1. On most days when readings were taken, condensed moisture was observed on the steel foil. Note that at days 9 and 12, no condensed moisture was observed when the specimens were removed from the humidity chamber. Ambient

RH was very low during that time period, and it is likely that the chamber was not providing the full 100% RH conditions.

The data indicated that for 4991 or 4941 VHB tape with steel foil applied to seal both flat faces, three hours of exposure to 100% RH will increase the % moisture of an initially dry specimen by approximately 0.04%. Considering that the G23F VHB tape used for the main research testing contained some moisture to begin with, and the ambient RH was less than 100%, the side study suggested that exposing specimens to elevated RH for three hours will not have a significant effect on ramp-to-fail, creep rupture, or DMA results.

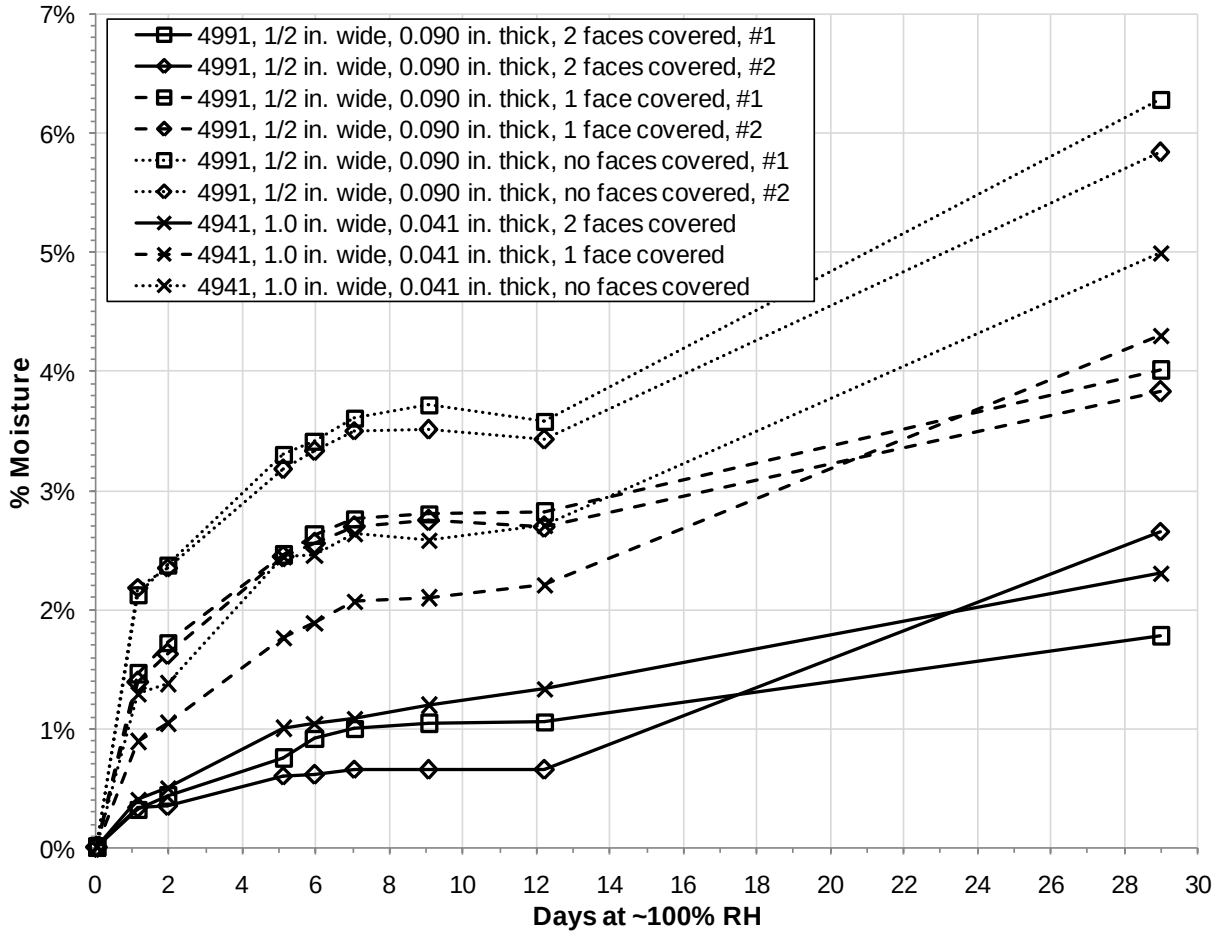

Figure I1 Moisture uptake for 4991 and 4941 VHB tape.

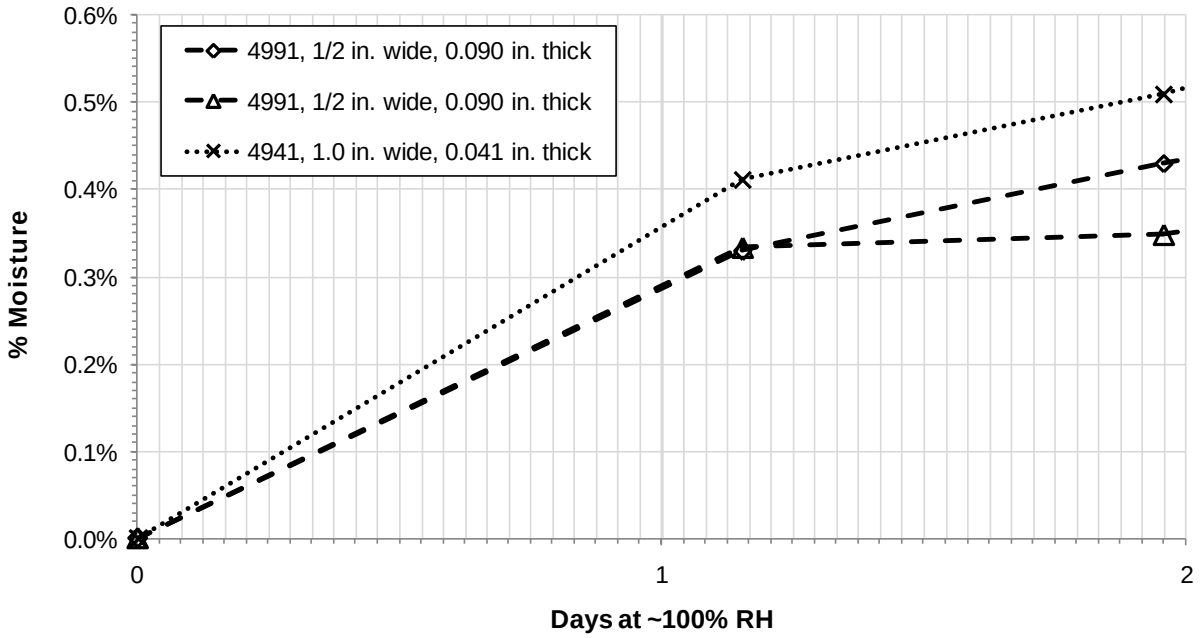

Figure I2 Short-term moisture uptake for VHB tape specimens with both flat faces sealed.

Table I1 % Moisture (Mass Water / Dry Mass of Specimen)

Days:	0.00	1.15	1.96	5.09	5.97	7.02	9.04	12.21	28.96
4991, 1/2 in. wide, 0.090 in. thick, 2 faces covered, #1	0.00%	0.33%	0.43%	0.75%	0.93%	1.01%	1.04%	1.07%	1.78%
4991, 1/2 in. wide, 0.090 in. thick, 1 face covered, #1	0.00%	1.46%	1.72%	2.46%	2.62%	2.77%	2.81%	2.82%	4.01%
4991, 1/2 in. wide, 0.090 in. thick, no faces covered, #1	0.00%	2.13%	2.38%	3.31%	3.42%	3.61%	3.73%	3.59%	6.29%
4991, 1/2 in. wide, 0.090 in. thick, 2 faces covered, #2	0.00%	0.33%	0.35%	0.61%	0.62%	0.66%	0.66%	0.66%	2.66%
4991, 1/2 in. wide, 0.090 in. thick, 1 face covered, #2	0.00%	1.39%	1.63%	2.45%	2.56%	2.69%	2.76%	2.70%	3.84%
4991, 1/2 in. wide, 0.090 in. thick, no faces covered, #2	0.00%	2.19%	2.35%	3.18%	3.33%	3.51%	3.52%	3.43%	5.85%
4941, 1.0 in. wide, 0.041 in. thick, 2 faces covered	0.00%	0.41%	0.51%	1.00%	1.05%	1.09%	1.20%	1.34%	2.31%
4941, 1.0 in. wide, 0.041 in. thick, 1 face covered	0.00%	0.89%	1.04%	1.77%	1.89%	2.07%	2.09%	2.22%	4.31%
4941, 1.0 in. wide, 0.041 in. thick, no faces covered	0.00%	1.30%	1.37%	2.45%	2.46%	2.65%	2.59%	2.71%	5.01%